Modelling evaporation and phase behaviour of particle suspensions

Christopher Chalmers

Submitted in partial fulfilment of the requirements for the award of
Doctor of Philosophy of Loughborough University

October 2017

Certificate of Originality

This is to certify that I am responsible for the work submitted in this thesis, that the original work is my own except as specified in acknowledgments or in footnotes, and that neither the thesis nor the original work contained therein has been submitted to this or any other institution for a degree.

Abstract

We present two statistical mechanics based methods for simulating the evaporation of droplets of nanoparticle suspensions from upon a heterogeneous surface. These are based on a generalised lattice-gas model. Properties such as wettability and the dynamic contact angle, are determined by the attraction strength parameters between particles and from the dynamic mobility coefficients. Both models incorporate the effects of surface roughness and slip at the surface. The two approaches used are Monte Carlo (MC) computer simulations and Dynamical Density Functional Theory (DDFT). We calculate the bulk fluid phase behaviour including the influence of the suspended nanoparticles, comparing results from the two approaches. We also calculate thermodynamic quantities such as the surface tensions. Our results show that the presence of steps in the surface can be crucial in controlling dewetting from heterogeneous surfaces. We also observe that coffee ring stains can be formed via the coupling of evaporation to phase separation and that the advective hydrodynamics within the droplets in not required for ring stains to form.

This thesis is partly based on the following publications:

Chapter 6

C. Chalmers, R. Smith, and A. J. Archer.

Modelling the evaporation of nanoparticle suspensions from heterogeneous surfaces

Journal of Physics: Condensed Matter, **29**, 295102 (2017).

Chapter 7

C. Chalmers, R. Smith, and A. J. Archer.

Dynamical density functional theory for the evaporation of droplets of nanoparticle suspension

Submitted (2017).

Chapter 8

B. Chacko, C. Chalmers, and A. J. Archer.

Two-dimensional colloidal fluids exhibiting pattern formation

J. Chem. Phys. **143**, 244904 (2015).

Contents

List of Figures

Chapter 1

Introduction

Modeling offers a way to obtain results for something potentially expensive and time consuming if done using experiments. Computer simulations and theory also offer the possibility to calculate quantities such as the free energy, which is not straightforward to do in experiments. It is almost trivial to run a simulation with a range of different values of parameters such as those determining the strength of attraction between molecules, whereas changing parameters experimentally can be difficult or impossible. The challenge is to create simulations that give good results and run in a practical amount of time.

In this thesis we look at two different modelling approaches to simulate the evaporation of droplets and films of colloidal suspensions, like ink or paint, from various different types of surfaces. Colloid suspensions are common in industry and the drying stage is a key part of the process. The size of droplets we consider are on the mesoscopic scale, typically only a few hundred times the size of the colloids. Colloid particles are typically 10nm-10µm in diameter. However the methods we develop can easily be scaled up to describe larger systems. There are a number of properties of droplet evaporation that make it difficult to simulate on the microscopic scale. The molecules that make up the liquid are many orders of magnitude smaller than the drop itself. The time scale for the interaction between the molecules is of the order of picoseconds, but it can take minutes for even small droplets to

fully evaporate. Such differences in scales make it infeasible to directly solve the Newton's equations of motion for all the particles. Instead of trying to handle each particle individually we use statistical mechanics, a theory that looks at the average behaviour of a system to determine the probability of observing a particular state.

The simulation models developed in the thesis consist of lattice-gas type models, i.e., generalised Ising models [1]. Putting the system on a discrete lattice makes the computer code for the simulations easier and run faster. Lattice models do have some limitations, for example they do not properly distinguish between the liquid and the solid state of a substance, nevertheless we show that lattice models can still give useful results.

The first few chapters in this thesis serve as an introduction to the material for the two main chapters, 6 and 7, which contain original results. The main chapters are structured as standalone research publications and can be read independently by readers familiar with the background material. The penultimate chapter is a publication where the author of this thesis contributed as second author to work that was led by another PhD student in the group. The system being modelled is different, but the methods are related.

Chapter 2 gives a brief introduction to simple liquids. It also introduces more complex liquids and gives some ideas on how they might be modelled. This is built on by us to chapter 3, which describes the key ideas of statistical mechanics used in this thesis. Statistical mechanics is the study of the average mechanics of systems of interacting particles. Statistical mechanics is an important topic and ideas in this chapter are the basis for both the density functional theory (DFT) [2, 3] and Monte Carlo (MC) [4, 5] models used in this thesis. Chapter 4 describes DFT which is a statistical mechanical theory able to predict the equilibrium density profiles for a system. Initially, continuum DFT is described, and then this is subsequently extended to describe the lattice based model which is used in chapter 7.

Chapter 5 introduces the basics of MC and Markov chains. This is to provide some of the background fundamentals for chapter 6. This uses an extended Metropolis MC algorithm to simulate the evaporation of droplets of nanoparticle suspensions. This work stems from

seeking to model some of the phenomena observed and overcome in using ink-jet printing in advanced manufacturing.

Chapter 7 develops a different method for simulating evaporating droplets, namely a dynamical DFT (DDFT) based model [6, 3, 7, 8, 9, 10, 11]. DDFT is based on DFT and is a theory that can calculate the progression of a density profile in time. The results from the DDFT are related to the MC results in the previous chapter since the underlying system is the same.

Chapter 8 describes work that is not connected to the previous two chapters. It looks at pattern forming in two dimensional colloid suspensions with a complex attraction potential. Lattice based DFT and MC simulations are used and the results are compared.

Chapter 9 contains some final concluding remarks and ideas for future work.

Chapter 2

Simple and complex liquids

Physical simple matter under normal conditions in everyday life exists in three different states, solid, liquid and gas. By simple matter, we mean systems of one type of roughly spherical particles with isotropic interactions between them. Each of these states has very different physical properties. The state of a substance can be changed by varying its temperature or pressure. We consider a substance to be made up of a collection of N molecules (where N is large, on the order of Avogadro's constant). The structure in which the particles are assembled depends on the thermodynamic state. When a substance is solid there is no 'flow' and each particle is rigidly part of a fixed structure. Liquid or gas (i.e. vapour) phases on the other hand can flow. Substances in the gas phase condense on cooling or when the pressure is increased. Similarly, liquids can evaporate when the temperature is increased or the pressure is reduced [3].

Under normal conditions a gas has a very low density. Collisions between the molecules in a gas are rare and can be modelled by the Boltzmann kinetic equation [12]. In contrast, liquids have a much higher density. The molecules are close together so that they constantly interact with each other. This significant change in behaviour is dependant on the balance between the intermolecular forces and the kinetic energy of the particles. If the temperature is high enough the modules are able to move fast enough to overcome the attractive inter-

molecular forces and spread out as much as possible, forming a gas. At lower temperatures, the intermolecular forces are strong enough to keep the particles together; this is known as cohesion. On further cooling the substance becomes solid. The particles can no longer move past one another and the substance forms a rigid solid. In this thesis we are mostly interested in substances in their fluid state.

Consider a closed system containing both the liquid and gas. For the two phases to coexist they must have the same temperature, pressure and chemical potential. Also when two different phases of a substance are in contact there is an interface between them. At the molecular level the density distribution profile at an interface takes the form of a continuous density change between one phase to the other but at the macroscopic scale the interface appears to be a sharp shift in density between the two phases and has a well defined surface area, A. At coexistence there is a constant exchange of molecules between the two phases but overall there is no net flux from one to the other. There is a free energy cost associated with the presence of the interface. There are entropic contributions to this, but the largest contribution is generally due to the broken bonds of the liquid molecules at the interface, since they have less neighbouring molecules than those in the bulk. The extra free energy is known as the surface tension, γ, which is the excess free energy per unit area due to the interface [13, 14, 15]. Thermodynamic systems try to minimise the free energy and so seek to minimise the surface area of the interface, which is why we see spherical drops of water when no gravity is present and why soap bubbles form sometimes complex shapes. There is an interfacial tension not only between the fluid phases but also there is a fluid-solid surface tension, which plays a key role in determining the shape of a liquid droplet on a surface.

2.0.1 Surface tension and contact angles

The equilibrium shape of a droplet in contact with a flat surface is determined by the various interfacial energies [14]. There are three interfaces, the gas-liquid interface, the liquid-solid and the gas-solid interface. There is an interfacial energy associated with all of these and
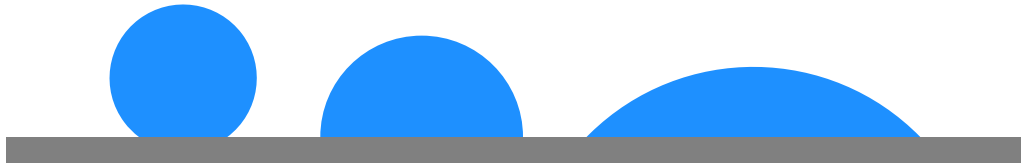
Figure 2.1: Three droplets in contact with a surface. From left to right: partially dry, 90°
contact angle and partially wet.

the droplet shape is determined by minimising the total free energy. In fact, the droplet
will make a spherical cap with the surface, at least at the macroscopic scale but whilst the
drop is still small enough that the effect of gravity can be neglected. The contact angle this
spherical cap makes with the surface depends on the three surface tensions, liquid-gas: γ_{lg},
wall-liquid: γ_{wl} and wall-gas: γ_{wg} and can be calculated by using Young's equation [14]:

$$\cos\theta = \frac{\gamma_{wg} - \gamma_{wl}}{\gamma_{lg}}. \tag{2.0.1}$$

Generally speaking a strong attraction between the liquid molecules and the surface gives
a smaller contact angle with the limit $\theta \to 0°$ producing a film of liquid that spreads out
on the surface, known as total wetting of the surface. Similarly, the weaker the attraction,
the larger the contact angle with the surface in the limit $\theta \to 180°$ (almost never achieved
in nature) producing a sphere that only touches the surface at single point, known as total
dewetting. Typical hydrophobic materials such as Teflon and wax do not usually reach a
contact angle over 130°, however there are some nano and micro structured surfaces with
contact angles near 170° [16]. A surface with a contact angle between 0° and 90° is known as
partially wet and an angle between 90° and 180° is known as partially dry. Figure 2.1 shows
a illustration of droplets in contact with a surface at different contact angles.

Normally, when a drop is initially placed on a surface it is not at equilibrium. The drop
subsequently flows towards a shape with the equilibrium contact angle and tries to reach
the minimum free energy equilibrium state. This is a problem that has been extensively

studied, both experimentally and theoretically. Assuming the surface is completely smooth, in the case of complete wetting ($\theta = 0$), the drop keeps spreading until it reaches a limiting thickness (usually determined by the van de Waals forces) [14]. However in day-to-day life, most surfaces are rough and very few surfaces are molecularly flat. Defects on a surface can pin the contact line of a drop. This is why droplets on an small inclusion can stay at rest even when the equilibrium contact angle is not achieved. A lot of the time a drop does not reach its equilibrium state because it gets caught in some metastable state, for example getting caught on a defect on the surface. If such a drop is left to evaporate the contact line can stay pinned initially and so the contact angle gets smaller as the evaporation proceeds. After enough evaporation, the contact line can suddenly start moving. This contact angle is smaller than the equilibrium contact angle and is called the receding contact angle [17]. Similarly, when the volume of a drop is increased, for example by injecting further liquid, the contact line remains pinned initially and then the contact angle increases until the contact line start moving. The angle at this point is called the advancing contact angle. The value of these angles depend on the roughness of the surfaces.

Contact angles offer a quantitative way to compare simulations, experiments and theoretical results. In chapter 6 contact angles are calculated from simulation results and briefly discussed. In chapter 7 the contact angles are compared with the KMC model and the receding contact angles as a drop evaporates are also calculated.

2.1   Pair potentials

The microscopic description of a liquid often starts from specifying an interaction potential between particles which in the simplest form is a pair potential. The pair potential is the potential energy from two molecules/particles in the liquid interacting. It is a function of the distance between the centres of two particles and can sometimes also depend on the orientation [3]. Assuming the interactions are solely via pair potentials often provides a good

description for how most particles interact. Sometimes three-body potentials and maybe even higher-body potentials are required, however, these are not considered here. Depending on the nature of the interactions between the molecules, the pair potentials can take different forms, including hard spheres, potentials with attraction, repulsion and combinations like potentials exhibiting short range attraction, but also with a long range repulsion.

The mechanisms for how particles truly interact are often quantum in nature [18] and so pair potentials are really only a classical approximation to the total effective interaction between the particles. One of the simplest pair potentials one can conceive is one with no interactions other than the prevention of particles overlapping:

$$V_{\mathrm{HS}}(r) = \begin{cases} \infty & r \leq \sigma, \\ 0 & \text{otherwise.} \end{cases} \tag{2.1.1}$$

This is known as the hard-sphere potential and describes certain colloid particles suspended in a solvent [3]. The parameter σ is the diameter of the particles. Another commonly used pair potential for describing simple molecules is the Lennard-Jones potential:

$$V_{\mathrm{LJ}}(r) = r\varepsilon \left[\left(\frac{\sigma}{r} \right)^{12} - \left(\frac{\sigma}{r} \right)^{6} \right], \tag{2.1.2}$$

where ε is the attraction parameter. This is a reasonable approximation for the interaction between the atoms of a Nobel gas such as Argon atoms which are spherical, do not overlap and have a small van-der Waals-London pair attraction [12]. Pair potentials are not limited to describing the interactions between the molecules of the same species as they can also describe the interactions between different molecules. In this case one must define a set of pair potential $V_{ij}(r)$, specifying the interaction between particles of species i and j.

More complex pair potentials can arise for more complicated fluids. The next sections considers examples of complex fluids and how this is reflected in the pair potentials.

2.1.1   Complex fluids

Simple fluids are those made up of a single species of small approximately spherical particles with simple short range van de Waals interaction, like nitrogen or argon. The behaviour of simple liquids has been studied extensively and is well understood [3]. While simple liquids are important, many useful liquids used in industry and everyday life are so called "complex liquids" and understanding their properties is crucial to improving their performance and reliability.

Even liquids that might seem simple can still exhibit complex behaviour. Take water for example: the arrangement of the hydrogen atoms around each oxygen at a 109° angle results in a dipole. Also, the arrangement of the electronic orbitals in water means that there are strong highly directional bonds between water molecules, which means that on the molecular scale, the molecules are aligned in a network-like structure. These complex interactions lead to interesting behaviour like the fact that an increase in the pressure can actually reduce the viscosity of water [12]. The arrangement of the bonds is also responsible for ice being less dense than water.

There are many ways a fluid can be complex: mixtures of different species can demix or have opposite charges; fluids can consist of molecules that are non-spherical or bonded in chains to form polymers. However, the class of complex liquids we are interested in here is colloidal suspensions. These are fluids where colloids, which are relatively large particles with diameter on the nm-μm scale, are suspended in a fluid. Colloidal suspensions are very common in everyday life: milk, ink, paint and lubricants are a few examples. The colloids can have varying shapes and sizes which can lead to interesting properties.

In Fig. 2.2 there is an illustration of a colloid surrounded by liquid molecules. The significant difference in the size of the colloids compared to the molecules that make up the surrounding fluid poses a problem for developing theories or computer simulation models. Attempting to model each liquid molecule individually using Newton's equations of motion is simply computationally infeasible. Even to model a few colloids would require of order of
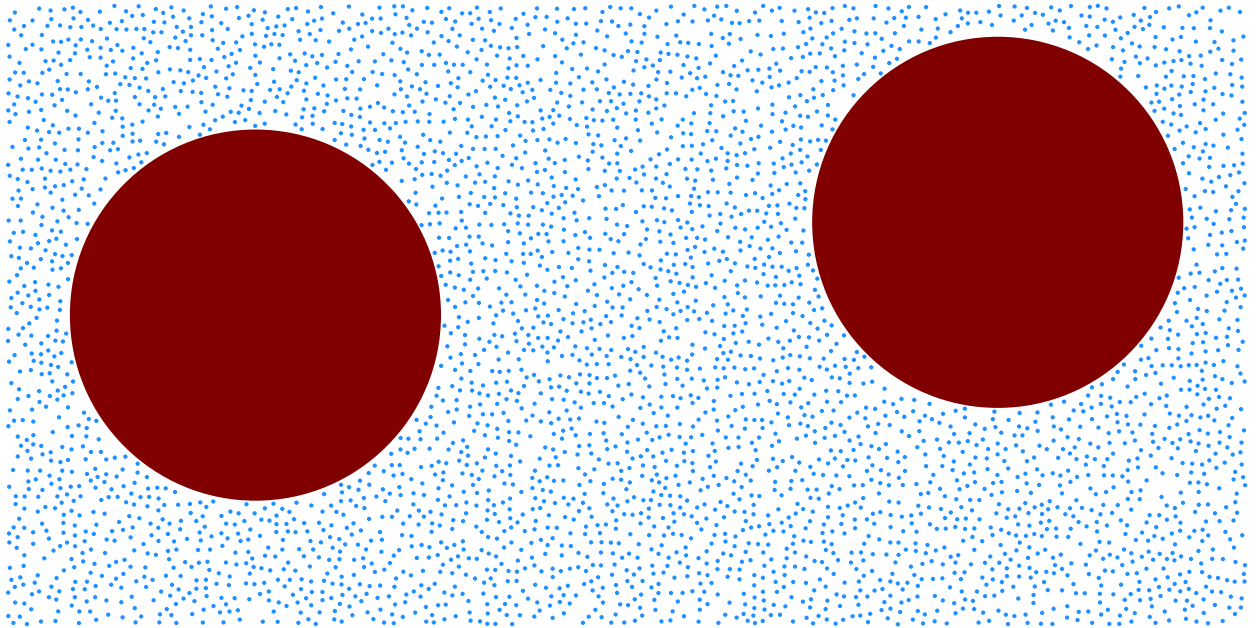
Figure 2.2: A 2D illustration of colloids (red) in suspension in a liquid (blue). Note that this is not to scale, the colloid would typically be much larger than this relative to the liquid molecules.

millions of particles. Instead, we take a step back and look at the motion at the scale of the colloid. At this scale the movement of the colloid appears to be random, known as Brownian motion [19]. Particles that undergo Brownian motion are called Brownian particles. The velocity of this motion is of the order of $\sqrt{k_B T/m}$ for particles of mass m and temperature T where k_B is Boltzmann's constant. We can also define a Brownian timescale, τ_B, which is the time it takes the colloid to travel a distance of order is own diameter. On the time scales for the overall macroscopic fluid motion this is a short time. However in this time many rearrangements of the surrounding liquid molecules have occurred.

To give a feeling for how this can be modelled we derive an equation of motion by considering the forces acting on a colloid. The resistance force that the liquid molecules apply to a colloid moving though the liquid is approximately proportional to the velocity of the colloid, $F_{\text{fric}} = -\gamma \dot{\mathbf{r}}$. We also assume that the liquid molecules have zero overall flow, meaning we neglect any hydrodynamic effects. Due to the thermal fluctuations there is also a random fluctuating force on the colloid.

Finally we consider the colloid to be under the influence of an external potential, ϕ. Therefore, the force exerted on it is given by $-\nabla\phi(\mathbf{r})$. Combining these three forces in Newton's equation yields the Langevin equation:

$$m\ddot{\mathbf{r}} = -\gamma\dot{\mathbf{r}} + \sqrt{2D}\mathbf{R}(t) - \nabla\phi(\mathbf{r}), \qquad (2.1.3)$$

where $\sqrt{2D}\mathbf{R}(t)$ is the random force due to the thermal fluctuations in the liquid and where D is the diffusion coefficient [19] and $\mathbf{R}(t) \in \mathbb{R}^3$ is a vector whose components are Gaussian random variables.

By considering the probability of a particle at position $x + \Delta x$ at time $t + \Delta t$ and using Eq. (2.1.3) in the over-damped limit, it is possible to derive the Smoluchowskii equation [19]

$$\frac{\partial\rho}{\partial t} = D\nabla \cdot \left[\nabla\rho + \beta\rho\nabla\phi(\mathbf{r})\right], \qquad (2.1.4)$$

where $\rho = \rho(\mathbf{r}, t)$ is the probability of finding the particle at position $\mathbf{r}$ at time t and $\beta = 1/k_B T$.

This is a partial differential equation that describes the time evolution of the probability of finding the particle at position $\mathbf{r}$. Note that when $\phi = 0$, Eq. (2.1.4) reduces to the diffusion equation. Using probability to describe a system is the essence of statistical mechanics. In the next section we introduce statistical mechanics and the basics of DFT.

Chapter 3

Statistical mechanics

The term 'Statistical Mechanics' was coined by American Physicist Josiah Willard Gibbs. He, together with Ludwig Boltzmann and James Clerk Maxwell in 1902 created the branch of mathematics that uses probability theory to study the average behaviour of many-body mechanical systems.

We consider an isolated system of N identical spherical particles of mass m. The state of the system is described by coordinates $\mathbf{r}^N = \mathbf{r}_1, \ldots, \mathbf{r}_N$ and momenta $\mathbf{p}^N = \mathbf{p}_1, \ldots, \mathbf{p}_N$. The Hamiltonian is the total energy of the system:

$$\mathcal{H}(\mathbf{r}^N, \mathbf{p}^N) = K_N(\mathbf{p}^N) + V_N(\mathbf{r}^N) + \Phi_N(\mathbf{r}^N), \tag{3.0.1}$$

where K_N is the kinetic energy of the N particles of mass m:

$$K_N(\mathbf{p}^N) = \sum_{i=1}^{N} \frac{\mathbf{p}_i^2}{2m}. \tag{3.0.2}$$

V_N is the potential energy due to the interactions between particles; we only consider two

body interactions so V_N can be written as a sum over pair contributions

$$V_N(\mathbf{r}^N) = \sum_{i<j}^{N} V(|\mathbf{r}_i - \mathbf{r}_j|) \tag{3.0.3}$$

where $V(r)$ is the pair potential. The external potential, Φ, is given by

$$\Phi_N(\mathbf{r}^N) = \sum_{i=1}^{N} \phi(\mathbf{r}_i), \tag{3.0.4}$$

where ϕ is the one body external potential [3].

3.1 Ensembles

An ensemble, also called a statistical ensemble, is a potentially infinite set of possible states that a certain real system might be in. In statistical mechanics we calculate average properties of a system by averaging over the ensemble of states. There are various different kinds of ensemble that are considered [1, 3], but here we only consider two: the canonical ensemble and the grand canonical ensemble.

3.1.1 Canonical ensemble

The states in a canonical ensemble all have the temperature T, volume V and the number of identical particles N is fixed. This is an appropriate ensemble to describe a closed system coupled to a heat bath. The probability of a given state in the canonical ensemble is given by [1, 3]

$$f(\mathbf{r}^N, \mathbf{p}^N) = \frac{1}{h^{dN} N!} \frac{e^{-\beta \mathcal{H}(\mathbf{r}^N, \mathbf{p}^N)}}{Z} \tag{3.1.1}$$

where h is Plank's constant, $\beta = 1/k_B T$ and d the dimensionality of the system. The term $1/N!$ is to correct for counting duplicate states, since the particles are indistinguishable. The

canonical partition function is

$$Z = \frac{1}{h^{dN} N!} \iint e^{-\beta \mathcal{H}(\mathbf{r}^N, \mathbf{p}^N)} \, \mathrm{d}\mathbf{r}^N \mathrm{d}\mathbf{p}^N, \tag{3.1.2}$$

where $\int \mathrm{d}\mathbf{r}^N = \int \mathrm{d}\mathbf{r}_1 \int \mathrm{d}\mathbf{r}_2 \ldots \int \mathrm{d}\mathbf{r}_N$ and $\int \mathrm{d}\mathbf{p}^N = \int \mathrm{d}\mathbf{p}_1 \int \mathrm{d}\mathbf{p}_2 \ldots \int \mathrm{d}\mathbf{p}_N$. The partition function is the sum (i.e. integral) over all the possible configurations of the system.

The total internal energy of the system at equilibrium, U, is given by the ensemble average of the Hamiltonian:

$$U = \langle \mathcal{H} \rangle. \tag{3.1.3}$$

We use the notation $\langle B \rangle$ as the statistical average of the thermodynamic quantity B, defined by

$$\langle B \rangle = \iint B(\mathbf{r}^N, \mathbf{p}^N) f(\mathbf{r}^N, \mathbf{p}^N) \, \mathrm{d}\mathbf{r}^N \, \mathrm{d}\mathbf{p}^N \tag{3.1.4}$$

The Helmholtz free energy, F, which is the obtainable work from a closed system, is given by

$$F = -k_B T \ln Z. \tag{3.1.5}$$

This is entirely consistent with the thermodynamic definition of the Helmholtz free energy [3].

$$F = U - TS \tag{3.1.6}$$

where U is the internal energy of the system defined in (3.1.8) and S is the entropy. The equilibrium state of a canonical system corresponds to the minimum of F.

An infinitesimal change to the internal energy can be written in differential form as

$$\mathrm{d}U = T\mathrm{d}S + \mu \mathrm{d}N - p\mathrm{d}V, \tag{3.1.7}$$

where μ is the chemical potential and p is the pressure. This is just the first law of thermodynamics, which is statement of the conservation of energy. Since S, N, and V are all

extensive quantities (quantities that scale with the size of the system) we have

$$U = TS + \mu N - pV. \tag{3.1.8}$$

Differentiating to write Eq. (3.1.6) in differential form and substituting in Eq. (3.1.7) gives

$$\mathrm{d}F = \mathrm{d}U - T\mathrm{d}S - S\mathrm{d}T$$

$$= \mu\mathrm{d}N - p\mathrm{d}V - S\mathrm{d}T. \tag{3.1.9}$$

Considering derivatives with each of N, V and T whilst the two other variables are constant we get three equations:

$$S = -\left(\frac{\partial F}{\partial T}\right)_{V,N}, \quad \mu = -\left(\frac{\partial F}{\partial N}\right)_{T,V}, \quad p = -\left(\frac{\partial F}{\partial V}\right)_{T,N}. \tag{3.1.10}$$

The above relations are used later extensively to calculate phase diagrams.

3.1.2 The configuration integral

The configuration integral is a factor of the partition function which is shown here and used to simplify calculations later. Using Eq. (3.0.1) the partition function can be written as

$$Z = \frac{1}{h^{dN}N!} \int e^{-\beta K_N(\mathbf{p}^N)} \, \mathrm{d}\mathbf{p}^N \int e^{-\beta[V_N(\mathbf{r}^N)+\Phi_N(\mathbf{r}^N)]} \, \mathrm{d}\mathbf{r}^N. \tag{3.1.11}$$

The integrals over the momenta and positions are independent, so they can be factorised using Eq. (3.0.2)

$$\int e^{-\beta K(\mathbf{p}^N)} \, \mathrm{d}\mathbf{p} = \prod_{i=1}^{N} \int e^{-\frac{\beta\mathbf{p}_i^2}{2m}} \, \mathrm{d}\mathbf{p}_i. \tag{3.1.12}$$

The components $\mathbf{p}_i = (p_{(i,1)}, p_{(i,2)}, \ldots, p_{(i,d)})$ are also independent where d is the dimensionality of the space. Now since $\int_{-\infty}^{\infty} e^{-\alpha^2 u^2} \mathrm{d}u = \sqrt{\pi}/\alpha$ we can write this as

$$\int e^{-\frac{\beta \mathbf{p}_i^2}{2m}} \, \mathrm{d}\mathbf{p}_i = \left(\frac{2\pi m}{\beta}\right)^{d/2}. \tag{3.1.13}$$

Thus we can write the partition function as

$$Z = Q\Lambda^{-dN}, \tag{3.1.14}$$

where $\Lambda = \sqrt{\frac{\beta h^2}{2\pi m}}$ is the thermal de Broglie wavelength and

$$Q = \frac{1}{N!} \int e^{-\beta(V_N + \Phi_N)} \, \mathrm{d}\mathbf{r}^N \tag{3.1.15}$$

is the configuration integral.

3.1.3 Grand canonical ensemble

Unlike the canonical ensemble where N, V and T are fixed, we can consider systems where the number of particles is no longer fixed. Instead the particles are free to move back and forth between the system and a reservoir that allows the exchange of particles. The average number of particles in the system is determined by the chemical potential of the reservoir, μ, which is the energy required to insert a particle into the system.

The probability of observing a particular state in the grand canonical ensemble is given by [3]

$$f(\mathbf{r}^N, \mathbf{p}^N) = \frac{1}{h^{dN} N!} \frac{e^{-\beta(\mathcal{H} - \mu N)}}{\Xi}, \tag{3.1.16}$$

where Ξ is the grand partition function,

$$\Xi = \mathrm{Tr}\left(e^{-\beta(\mathcal{H} - \mu N)}\right), \tag{3.1.17}$$

and where Tr denotes the classical trace [3, 20]:

$$\text{Tr}(\cdot) \equiv \sum_{N=0}^{\infty} \frac{1}{h^{dN} N!} \iint (\cdot) \, d\mathbf{r}^N d\mathbf{p}^N. \tag{3.1.18}$$

The ensemble average is

$$\langle B \rangle = \text{Tr}(fB), \tag{3.1.19}$$

where f is the probably density (3.1.16) and B is an arbitrary physical quantity.

The thermodynamic potential for the grand canonical system is called the grand free energy, Ω, defined as

$$\Omega = F - \overline{N}\mu, \tag{3.1.20}$$

where $\overline{N} = \langle N \rangle$ is average number of particles in the system.

Similar to the canonical free energy we can write the grand potential in differential form:

$$d\Omega = -SdT - \overline{N}d\mu - pdV. \tag{3.1.21}$$

In a manner analogous to that in the canonical ensemble we can consider the variables separately in order to obtain thermodynamic quantities expressed as derivatives of the free energy:

$$S = -\left(\frac{\partial \Omega}{\partial T}\right)_{\mu,V}, \quad \overline{N} = -\left(\frac{\partial \Omega}{\partial \mu}\right)_{T,V}, \quad p = -\left(\frac{\partial \Omega}{\partial V}\right)_{T,\mu}. \tag{3.1.22}$$

Using Eq. (3.1.20) and Eq. (3.1.8) we find that the grand potential reduces to

$$\Omega = -pV. \tag{3.1.23}$$

The grand potential can also be written in terms of the grand partition function as

$$\Omega = -k_B T \ln \Xi, \tag{3.1.24}$$

which expresses Ω in terms of Ξ, which is a sum over all states of the system. The equilibrium state of a system is given by the minimum of Ω [1, 3, 20].

Chapter 4

Density Functional Theory

Density Functional Theory (DFT) started as a quantum mechanical theory developed in the 1960s to describe the density distribution of electrons. It was known this theory could also be extended to describe classical systems around this time but it wasn't until the 1970s review by Evans [20] that DFT was introduced for systems of classical interacting particles to a broad audience.

Calculating the partition function Z is not always practical as it involves summing all possible configurations of the system. Thus, an approximation of the partition function is needed. DFT [2, 3, 20] instead focuses on developing a good approximation for the Helmholtz free energy and is therefore [c.f. Eq (3.1.24)] able to provide a good approximation of the partition function. The grand free energy Ω is expressed as a functional of the average density at point $\mathbf{r}$, $\rho(\mathbf{r})$. This functional is then minimised with respect to variations in $\rho(\mathbf{r})$ and the profile which minimises Ω is the equilibrium profile. The value of Ω at this minimum is the thermodynamic grand potential.

4.1   Intrinsic Helmholtz free energy

The intrinsic Helmholtz free energy, $\mathcal{F}$ is defined as the Helmholtz free energy minus the contribution due to the external field. Recall that the external potential is given by

$$\Phi_N = \sum_{i=1}^{N} \phi(\mathbf{r}_i) \tag{4.1.1}$$

$$= \int \hat{\rho}(\mathbf{r})\phi(\mathbf{r})\,\mathrm{d}\mathbf{r}, \tag{4.1.2}$$

where $\hat{\rho}(\mathbf{r}) = \sum_{i=1}^{N} \delta(\mathbf{r} - \mathbf{r}_i)$ is the density operator. The ensemble average density profile is defined by $\rho(\mathbf{r}) = \langle\hat{\rho}(\mathbf{r})\rangle$ and so also the statistical average contribution to the (free) energy due to the external potential can be written as

$$\langle\Phi_N\rangle = \int \rho(\mathbf{r})\phi(\mathbf{r})\,\mathrm{d}\mathbf{r}. \tag{4.1.3}$$

Thus, the intrinsic Helmholtz free energy is

$$\mathcal{F} = F - \langle\Phi_N\rangle. \tag{4.1.4}$$

It turns out that the intrinsic free energy functional $\mathcal{F}$ in no way depends on the external potential [2, 3, 20].

To obtain an expression for $\mathcal{F}$, we first consider the case with no external potential and no interactions between the particles, $V_N = \Phi = 0$, i.e. an ideal gas. In this case the configuration integral (3.1.15) is

$$Q = \frac{1}{N!} \int \mathrm{d}\mathbf{r}^N \tag{4.1.5}$$

$$= \frac{V^N}{N!}. \tag{4.1.6}$$

Using Eqs. (3.1.5), (3.1.14) and (4.1.4) the ideal intrinsic free energy is

$$\mathcal{F}_{\text{id}} = k_B T \ln \left(\frac{N! \Lambda^{dN}}{V^N} \right) \tag{4.1.7}$$

$$= k_B T \left(\ln N! + N \ln \frac{\Lambda^d}{V} \right). \tag{4.1.8}$$

For large N we can use Stirling's formula, $\ln N! \approx N \ln N - N$, to obtain

$$\mathcal{F}_{\text{id}} \approx k_B T N \left(\ln N + \ln \frac{\Lambda^d}{V} - 1 \right) \tag{4.1.9}$$

$$= k_B T N \left(\ln \frac{N \Lambda^d}{V} - 1 \right). \tag{4.1.10}$$

For this uniform system the density $\rho(\mathbf{r})$ is constant with $\rho = N/V$. This gives

$$\mathcal{F}_{\text{id}} = k_B T V \rho (\ln[\Lambda^d \rho] - 1). \tag{4.1.11}$$

This result is in fact more general and for an inhomogeneous ideal gas we obtain the generalisation of this:

$$\mathcal{F}_{\text{id}} = k_B T \int \rho(\mathbf{r}) (\ln[\Lambda^d \rho(\mathbf{r})] - 1) \, d\mathbf{r}. \tag{4.1.12}$$

More generally, when there are interactions between the particles, the total intrinsic free energy can be written as a sum of the ideal gas part plus an excess free energy term which incorporates the contribution to the free energy due to the particle interactions [2, 3, 20]:

$$\mathcal{F} = \mathcal{F}_{\text{id}} + \mathcal{F}_{\text{ex}}. \tag{4.1.13}$$

4.2   The grand potential functional

Using equation Eq. (4.1.4) we write the grand potential, $\Omega = F - \overline{N}\mu$, as

$$\Omega = \mathcal{F} + \int \rho(\mathbf{r})\phi(\mathbf{r})\,\mathrm{d}\mathbf{r} - \overline{N}\mu \qquad (4.2.1)$$

$$= \mathcal{F} - \int \rho(\mathbf{r})u(\mathbf{r})\,\mathrm{d}\mathbf{r}, \qquad (4.2.2)$$

where $u(\mathbf{r}) = \mu - \phi(\mathbf{r})$. The grand potential and intrinsic Helmholtz free energy are functionals of the density profile, which we denote using the notation $\Omega[\rho]$ and $\mathcal{F}[\rho]$ to show functional dependencies. From (4.1.12) and (4.2.2) we obtain

$$\Omega[\rho(\mathbf{r})] = k_B T \int \rho(\mathbf{r})\big(\ln[\Lambda^d \rho(\mathbf{r})] - 1\big)\,\mathrm{d}\mathbf{r} + \mathcal{F}_{\mathrm{ex}} - \int \rho(\mathbf{r})u(\mathbf{r})\,\mathrm{d}\mathbf{r}. \qquad (4.2.3)$$

Note that this shows that Ω is a Legendre transform of $\mathcal{F}$. Since the system is in the grand canonical ensemble, the minimum of the grand potential corresponds to the equilibrium state. We denote the density profile which minimises Ω to be $\rho_0(\mathbf{r})$. This minimising density profile can be found by solving the Euler-Lagrange equation

$$\left.\frac{\delta\Omega[\rho(\mathbf{r})]}{\delta\rho(\mathbf{r})}\right|_{\rho(\mathbf{r})=\rho_0(\mathbf{r})} = 0. \qquad (4.2.4)$$

Taking the functional derivative of Eq. (4.2.3) gives

$$\frac{\delta\Omega[\rho(\mathbf{r})]}{\delta\rho(\mathbf{r})} = \beta^{-1}\ln[\Lambda^d \rho(\mathbf{r})] - \beta^{-1}c^{(1)}(\mathbf{r}) - u(\mathbf{r}) = 0, \qquad (4.2.5)$$

where $\beta = 1/k_B T$ and

$$c^{(1)}(\mathbf{r}) \equiv -\beta\frac{\delta\mathcal{F}_{\mathrm{ex}}[\rho(\mathbf{r})]}{\delta\rho(\mathbf{r})} \qquad (4.2.6)$$

is the one-body direct correlation function [2, 3]. Taking a further functional derivative yields the two-body direct correlation function

$$c^{(2)}(\mathbf{r}_1, \mathbf{r}_2) \equiv -\beta \frac{\delta^2 \mathcal{F}_{\mathrm{ex}}[\rho(\mathbf{r}_1)]}{\delta\rho(\mathbf{r}_1)\delta\rho(\mathbf{r}_2)}. \tag{4.2.7}$$

This is a key quantity used in the study of pair correlations in liquids.

The general approach in DFT is to develop a suitable approximation for $\mathcal{F}_{\mathrm{ex}}[\rho]$ and then by solving Eq. (4.2.5) the equilibrium density profile $\rho(\mathbf{r})$ is obtained. This profile can then be substituted into Eq. (4.2.3) to obtain the grand free energy Ω and from this many other thermodynamic quantities can also be obtained. For more background on DFT and also some of the approximations used for $\mathcal{F}_{\mathrm{ex}}[\rho]$, see Refs. [2, 3].

4.3 The Ornstein-Zernike Equation

The Ornstein-Zernike (OZ) equation is an integral equation used to define the direct correlation function [3]. The total pair correlation function for an inhomogeneous fluid $h^{(2)}(\mathbf{r}_1, \mathbf{r}_2)$ is defined as

$$h^{(2)}(\mathbf{r}_1, \mathbf{r}_2) = g^{(2)}(\mathbf{r}_1, \mathbf{r}_2) - 1 \tag{4.3.1}$$

where $g^{(2)}$ is the pair distribution function, a quantity from which one can obtain the joint probability of finding one particle at $\mathbf{r}_1$, at the same time as finding another at $\mathbf{r}_2$. As $|\mathbf{r}_1 - \mathbf{r}_2| \to \infty$, $h^{(2)} \to 0$. It turns out that the correlation function $c^{(2)}(\mathbf{r}_1, \mathbf{r}_2)$ is related to the total pair correlation function and to the single particle density by the (inhomogeneous fluid) Ornstein-Zernike equation [3, 20]

$$h^{(2)}(\mathbf{r}_1, \mathbf{r}_2) = c^{(2)}(\mathbf{r}_1, \mathbf{r}_2) + \int c^{(2)}(\mathbf{r}_1, \mathbf{r}_3)\rho^{(1)}(\mathbf{r}_3)h^{(2)}(\mathbf{r}_3, \mathbf{r}_2)\, \mathrm{d}\mathbf{r}_3. \tag{4.3.2}$$

This allows for a good intuitive understanding of $c^{(1)}(\mathbf{r}_1, \mathbf{r}_2)$: it gives the direct correlation between particles 1 and 2 whilst the second term in (4.3.2) gives the indirect correlation

between the other particles. That can be seen even more clearly by recursively substituting Eq. (4.3.2) for $h^{(2)}$ to give

$$h^{(2)}(\mathbf{r}_1, \mathbf{r}_2) = c^{(2)}(\mathbf{r}_1, \mathbf{r}_2) + \int c^{(2)}(\mathbf{r}_1, \mathbf{r}_3)\rho^{(1)}(\mathbf{r}_3)c^{(2)}(\mathbf{r}_3, \mathbf{r}_2)\, \mathrm{d}\mathbf{r}_3$$
$$+ \iint c^{(2)}(\mathbf{r}_1, \mathbf{r}_3)\rho^{(1)}(\mathbf{r}_3)c^{(2)}(\mathbf{r}_3, \mathbf{r}_4)\rho^{(1)}(\mathbf{r}_4)c^{(2)}(\mathbf{r}_4, \mathbf{r}_2)\, \mathrm{d}\mathbf{r}_3\mathrm{d}\mathbf{r}_4 + \cdots . \quad (4.3.3)$$

In general the pair direct correlation function $c^{(2)}$ is unknown so we cannot directly find the value of $h^{(2)}$. However if we assume the particles interact via a pair potential $V(r)$, one can obtain the following closure relation [3]

$$c^{(2)}(r) = h^{(2)}(r) - \ln[g^{(2)}(r)] - \beta V(r) + B(r), \quad (4.3.4)$$

although this still involves $B(r)$, which is the bridge function and which is also not known exactly. However, simple approximations for $B(r)$ can often yield fairly accurate results. For example, the so called Hypernetted-Chain (HNC) approximation sets $B = 0$ to yield [3]

$$c^{(2)}_{\mathrm{HNC}}(r) = h^{(2)}(r) - \ln[g^{(2)}(r)] - \beta V(r), \quad (4.3.5)$$

which can be fairly accurate, especially for soft core particle fluids.

4.4 DFT for lattice models

The following section closely follows the presentation in Ref. [21]. We can map a continuous system to be described on a regular grid with lattice spacing σ, which we set to $\sigma = 1$ throughout. Each site is labeled with an index $\mathbf{i}$. For a one component fluid we describe the state of the system by a set of occupation numbers

$$\{n_{\mathbf{1}}, n_{\mathbf{2}} \ldots, n_{\mathbf{N}}\} \quad (4.4.1)$$

where $n_\mathbf{i}$ is the occupation number for site $\mathbf{i} = (i, j, k)$, i.e., $n_\mathbf{i} = 0$ for an empty site and $n_\mathbf{i} = 1$ for an occupied site. Note that there are $M = N_x N_y N_z$ lattice sites in the system where the Mth site is $\mathbf{N} = (N_x, N_y, N_z)$. Now the configuration integral (3.1.15) becomes a sum over all the different configurations of the lattice sites. The configurational part of the Hamiltonian is approximated by

$$E\left(\{n_\mathbf{i}\}\right) = \sum_{\mathbf{i}=1}^{\mathbf{M}} n_\mathbf{i} \Phi_\mathbf{i} + \frac{1}{2} \sum_{\mathbf{i},\mathbf{j}} V_{\mathbf{i},\mathbf{j}} n_\mathbf{i} n_\mathbf{j} \tag{4.4.2}$$

where $\Phi_\mathbf{i}$ is the external potential at lattice site $\mathbf{i}$ and the second term is the energy contribution from interactions between particles, i.e., $V_{\mathbf{i},\mathbf{j}}$ is a discretised pair potential. We assume there are only two-body interactions.

The probability of a certain state $\{n_\mathbf{i}\}$ is given by

$$f\left(\{n_\mathbf{i}\}\right) = \frac{e^{-\beta E(\{n_\mathbf{i}\})}}{Z} \tag{4.4.3}$$

where

$$Z = \sum_{\text{all states}} e^{(-\beta E_{\text{state}})}, \tag{4.4.4}$$

is the partition function and "state" means a possible lattice configuration $\{n_\mathbf{i}\}$. This can also be written as $Z = \text{Tr}^L(e^{-\beta E_{\text{state}}})$ where Tr^L is the lattice trace:

$$\text{Tr}^L(x) = \sum_{\text{all states}} x = \sum_{n_\mathbf{1}=0}^{1} \sum_{n_\mathbf{2}=0}^{1} \cdots \sum_{n_\mathbf{N}=0}^{1} \tag{4.4.5}$$

Calculating Z directly is not always possible. However if we consider the case with no inter-particle interactions, $V_{\mathbf{i},\mathbf{j}} = 0$, and no external potential, $\Phi_\mathbf{i} = 0$, we have $f(\{n_\mathbf{i}\}) = 1/Z$. This means each state has equal probability. Therefore, from Eq. (4.4.4), the partition for a

system of N identical particles distributed around M lattice sites is

$$Z = \frac{M!}{N!(M-N)!}. \tag{4.4.6}$$

For large N and M we can use Stirling's approximation: $\ln N! \approx N \ln N - N$. Substituting into the equation for the Helmholtz free energy we get

$$\beta F = -M \ln M + N \ln N + (M-N) \ln(M-N). \tag{4.4.7}$$

Since this is a uniform system, the density $\rho = N/M$, so the free energy per unit volume can be written as

$$\frac{\beta F}{M} = \rho \ln \rho + (1-\rho) \ln(1-\rho). \tag{4.4.8}$$

For inhomogeneous fluids the density is not uniform. The Helmholtz free energy of an inhomogeneous fluid can be expressed in terms of the average density at site $\mathbf{i}$, defined as

$$\rho_{\mathbf{i}} = \langle n_{\mathbf{i}} \rangle$$
$$= \mathrm{Tr}^L (n_{\mathbf{i}} P_{\text{state}}) \tag{4.4.9}$$

where there grand canonical probability

$$P_{\text{state}} = \frac{e^{-\beta(E_{\text{state}} - \mu N)}}{\Xi} \tag{4.4.10}$$

and where the normalising factor is the grand partition function

$$\Xi = \mathrm{Tr}^L \left(e^{-\beta(E_{\text{state}} - \mu N)} \right). \tag{4.4.11}$$

From Eq. (3.1.24) we have $\Xi = e^{-\beta\Omega}$. Substituting this into (4.4.11) yields

$$e^{-\beta\Omega} = \text{Tr}^L \left(e^{-\beta(E_{\text{state}} - \mu N)} \right). \tag{4.4.12}$$

In order to develop an approximation for Ω we choose an inhomogeneous reference system with Hamiltonian E_0 that has no particle interactions ($V_{\mathbf{i},\mathbf{j}} = 0$) (with probability P_0 and grand partition function Ξ_0):

$$E_0 = \sum_{\mathbf{i}=1}^{M} (\Phi_{\mathbf{i}} + \varphi_{\mathbf{i}}) n_{\mathbf{i}}, \tag{4.4.13}$$

where $\Phi_{\mathbf{i}}$ is the external potential and $\varphi_{\mathbf{i}}$ are variational parameters to be determined. Then we can rewrite the energy as $E = E_0 + \Delta E$ where $\Delta E = E - E_0$. We have

$$e^{-\beta\Omega} = \text{Tr}^L \left(e^{-\beta(E_0 - \mu N)} e^{-\beta\Delta E} \right). \tag{4.4.14}$$

From Eq. (4.4.10), we can write $P_0 = e^{-\beta(E_0 - \mu N)}/\Xi_0$. Now the statistical average value of any quantity x in the reference system is given by

$$\langle x \rangle_0 = \text{Tr}^L \left(\frac{e^{-\beta(E_0 - \mu N)}}{\Xi_0} x \right), \tag{4.4.15}$$

so, returning to Eq. (4.4.14), recalling that $\Xi_0 = e^{-\beta\Omega_0}$ and that Tr^L is a linear operator, we have

$$\begin{aligned}
e^{-\beta\Omega} &= e^{-\beta\Omega_0} \text{Tr}^L \left(\frac{e^{-\beta(E_0 - \mu N)}}{\Xi_0} e^{-\beta\Delta E} \right) \\
&= e^{-\beta\Omega_0} \langle e^{-\beta\Delta E} \rangle_0.
\end{aligned} \tag{4.4.16}$$

Now since e^{-x} is a convex function this implies $\langle e^{-x} \rangle \geq e^{\langle -x \rangle}$. Making use of this we get

$$e^{-\beta\Omega} \geq e^{-\beta\Omega_0} e^{-\beta\langle \Delta E \rangle_0}. \tag{4.4.17}$$

Taking the logarithm of each side yields the Gibbs-Bogoliubov inequality:

$$\Omega \leq \Omega_0 + \langle \Delta E \rangle_0. \tag{4.4.18}$$

This gives an upper bound that we can minimise to give an approximation for the grand potential. Note that this depends only on the energy of our reference system, E_0.

Furthermore, since E_0 contains the undermined parameters $\varphi_{\mathbf{i}}$, these can be varied to obtain a minimal value in the right hand side of (4.4.18) and so obtain an optimal approximation for Ω.

From Eq. (4.4.11) we have

$$
\begin{aligned}
\Xi_0 &= \mathrm{Tr}^{\mathrm{L}} \, e^{-\beta(E_0 - \mu N)} \\
&= \sum_{n_{\mathbf{1}}=0}^{1} \sum_{n_{\mathbf{2}}=0}^{1} \cdots \sum_{n_{\mathbf{M}}=0}^{1} e^{-\beta \sum_{\mathbf{i}=1}^{M} \gamma_{\mathbf{i}} n_{\mathbf{i}}} \\
&= \left[\sum_{n_{\mathbf{1}}=0}^{1} e^{-\beta \gamma_1 n_{\mathbf{1}}} \right] \left[\sum_{n_{\mathbf{2}}=0}^{1} e^{-\beta \gamma_2 n_{\mathbf{2}}} \right] \cdots \left[\sum_{n_{\mathbf{M}}=0}^{1} e^{-\beta \gamma_M n_{\mathbf{M}}} \right] \\
&= \left[1 + e^{-\beta \gamma_{\mathbf{1}}} \right] \left[1 + e^{-\beta \gamma_{\mathbf{2}}} \right] \cdots \left[1 + e^{-\beta \gamma_{\mathbf{M}}} \right] \\
&= \prod_{\mathbf{i}=1}^{M} \left(1 + e^{-\beta \gamma_{\mathbf{i}}} \right)
\end{aligned}
\tag{4.4.19}
$$

where $\gamma_{\mathbf{i}} = \Phi_{\mathbf{i}} + \varphi_{\mathbf{i}} - \mu$. Rearranging and substituting Eq. (4.4.10) into Eq. (4.4.9) we get,

$$
\begin{aligned}
\rho_{\mathbf{i}} &= \frac{1}{\Xi_0} \sum_{n_{\mathbf{1}}=0}^{1} \sum_{n_{\mathbf{2}}=0}^{1} \cdots \sum_{n_{\mathbf{M}}=0}^{1} n_{\mathbf{i}} e^{\left(-\beta \sum_{\mathbf{j}=1}^{M} \gamma_{\mathbf{j}} n_{\mathbf{j}} \right)} \\
&= \frac{\displaystyle\sum_{n_{\mathbf{i}}=0}^{1} n_{\mathbf{i}} e^{\left(-\beta \sum_{\mathbf{j}=1}^{M} \gamma_{\mathbf{j}} m_{\mathbf{j}} \right)}}{\displaystyle\sum_{n_{\mathbf{i}}=0}^{1} e^{\left(-\beta \sum_{\mathbf{j}=1}^{M} \gamma_{\mathbf{j}} n_{\mathbf{j}} \right)}} \\
&= \frac{e^{-\beta \gamma_{\mathbf{i}}}}{1 + e^{-\beta \gamma_{\mathbf{i}}}}.
\end{aligned}
\tag{4.4.20}
$$

This implies that

$$1 - \rho_i = \frac{1}{1 + e^{-\beta\gamma_i}} \tag{4.4.21}$$

and

$$\rho_i = e^{-\beta\gamma_i}(1 - \rho_i). \tag{4.4.22}$$

From Eq. (4.4.19) this means $\Xi_0 = \prod_{i=1}^{M} \frac{1}{1 - \rho_i}$ so the grand free energy becomes:

$$\Omega_0 = -k_B T \ln \Xi_0$$

$$= -k_B T \ln \left(\prod_{i=1}^{M} \frac{1}{1 - \rho_i} \right)$$

$$= -k_B T \sum_{i=1}^{M} \ln \left(\frac{1}{1 - \rho_i} \right)$$

$$= k_B T \sum_{i=1}^{M} \ln (1 - \rho_i).$$

$$= k_B T \sum_{i=1}^{M} (\rho_i + 1 - \rho_i) \ln(1 - \rho_i)$$

$$= k_B T \sum_{i=1}^{M} [\rho_i \ln(1 - \rho_i) + (1 - \rho_i) \ln(1 - \rho_i)]. \tag{4.4.23}$$

From Eq. (4.4.22) we have $\ln(1 - \rho_i) = \beta\gamma_i + \ln \rho_i$. So above equation can be expressed as

$$\Omega_0 = k_B T \sum_{i=1}^{M} [\rho_i \ln(\rho_i) + (1 - \rho_i) \ln(1 - \rho_i)] + \sum_{i=1}^{M} \gamma_i \rho_i. \tag{4.4.24}$$

Substituting $\gamma_i = \Phi_i + \varphi_i - \mu$ from above:

$$\Omega_0 = k_B T \sum_{i=1}^{M} [\rho_i \ln(\rho_i) + (1 - \rho_i) \ln(1 - \rho_i)] + \sum_{i=1}^{M} (\Phi_i + \varphi_i - \mu)\rho_i. \tag{4.4.25}$$

We can write

$$\Omega = F - \mu \sum_{i=1}^{M} \rho_i, \tag{4.4.26}$$

where,

$$F = k_B T \sum_{i=1}^{M} [\rho_i \ln(\rho_i) + (1 - \rho_i) \ln(1 - \rho_i)] + \sum_{i=1}^{M} (\Phi_i + \varphi_i) \rho_i. \qquad (4.4.27)$$

From Eq. (4.4.2) we can write

$$\Delta E = \frac{1}{2} \sum_{i,j} V_{i,j} n_i n_j - \sum_{i=1}^{M} \varphi_i n_i. \qquad (4.4.28)$$

Since $\rho_i = \langle n_i \rangle$, we have

$$\langle \Delta E \rangle_0 = \frac{1}{2} \sum_{i,j} V_{i,j} \rho_i \rho_j - \sum_{i=1}^{M} \varphi_i \rho_i. \qquad (4.4.29)$$

From Eqs. (4.4.25) and (4.4.29) we can write the upper bound for the grand potential, $\hat{\Omega}$,

$$\hat{\Omega} = \Omega_0 + \langle \Delta E \rangle_0$$

$$= k_B T \sum_{i=1}^{M} [\rho_i \ln(\rho_i) + (1 - \rho_i) \ln(1 - \rho_i)] + \frac{1}{2} \sum_{i,j} V_{i,j} \rho_i \rho_j + \sum_{i=1}^{M} (\Phi_i - \mu) \rho_i. \qquad (4.4.30)$$

We see that $\varphi_i = \frac{1}{2} \sum_j V_{i,j} \rho_j$, by comparing Eqs. (4.4.25) and (4.4.30), where φ_i is the mean field, i.e. the effective field at site i due to other particles around it. In Eq. (4.4.30) we see we have derived a discretised DFT with a particular approximation for the excess free energy $\mathcal{F}_{\text{ex}}$.

The foundations of DFT derived in this chapter are used later in chapter 7 to run simulations using Dynamic DFT (DDFT) which is based on equilibrium DFT. In the next chapter we look at another approach to statistical mechanics: Monte-Carlo simulations. This approach no longer uses densities to describe a system, but instead uses a discrete description, namely the lattice occupation numbers in Eq. (4.4.1), and evolves these in time by repeated random sampling from a probability distribution that takes as input the lattice Hamiltonian in Eq. (4.4.2).

4.5   DDFT

Now we have established a way to calculate equilibrium density profiles, we wish to build upon this theory to incorporate dynamics. The following derivation follows the description presented in [8].

For a system of N interacting Brownian particles with overdamped equation of motion [c.f. Eq. (2.1.3), in the limit $m \to 0$]:

$$\gamma \dot{\mathbf{r}}_i = -\nabla U_N(\mathbf{r}_i) + \sqrt{2D}\mathbf{R}(t), \tag{4.5.1}$$

where the total potential energy is [c.f. Eqs. (3.0.1) – (3.0.4)]:

$$U_N(\mathbf{r}^N, t) = \sum_{i=1}^{N} \phi(\mathbf{r}_i, t) + \frac{1}{2} \sum_{j \neq i}^{N} \sum_{i} v(\mathbf{r}_i, \mathbf{r}_j), \tag{4.5.2}$$

where $\phi(\mathbf{r})$ is the external potential and $v(r)$ is the pair interaction potential between the particles. Thus, the configuration of the system is defined by $\mathbf{r}^N = \{\mathbf{r}_1, \mathbf{r}_2, \ldots, \mathbf{r}_N\}$, the set of positions of all the particles. The time evolution of the N-particle probability distribution $\rho^{(N)}(\mathbf{r}^N, t)$ is given by the Smolochowskii equation [20]

$$\frac{\partial \rho^{(N)}(\mathbf{r}^N, t)}{\partial t} = \Gamma \sum_{i=1}^{N} \nabla_i \left[k_B T \nabla_i + \nabla_i U(\mathbf{r}^N, t) \right] \rho^{(N)}(\mathbf{r}^N, t), \tag{4.5.3}$$

where $\Gamma = \gamma^{-1}$. Integrating over all except one of the position coordinates in the Smolochowskii equation yields

$$\frac{\partial \rho(\mathbf{r}_1, t)}{\partial t} = \Gamma k_B T \nabla_1^2 \rho(\mathbf{r}_1, t) + \Gamma \nabla_1 [\rho(\mathbf{r}, t) \nabla_1 \phi(\mathbf{r}_1, t)] + \Gamma \nabla_1 \int \rho^{(2)}(\mathbf{r}_1, \mathbf{r}_2, t) \nabla_1 v(\mathbf{r}_1, \mathbf{r}_2) \, d\mathbf{r}_2 \tag{4.5.4}$$

where the one-body density profile

$$\rho(\mathbf{r}_1, t) = N \int d\mathbf{r}_2 \cdots \int d\mathbf{r}_N \rho^{(N)}(\mathbf{r}^N, t) \tag{4.5.5}$$

and the two-body density

$$\rho^{(2)}(\mathbf{r}_1, \mathbf{r}_2, t) = N(N-1) \int d\mathbf{r}_3 \cdots \int d\mathbf{r}_N \rho^{(N)}(\mathbf{r}^N, t). \tag{4.5.6}$$

Note that in Eq. (4.5.4) if we set the pair potential $v = 0$, then we obtain Eq. (2.1.4). In order to close Eq. (4.5.4), we can apply the equilibrium sum rule [20]

$$- k_B T \rho(\mathbf{r}_1) \nabla c^{(1)}(\mathbf{r}_1) = \int \rho^{(2)}(\mathbf{r}_1, \mathbf{r}_2) \nabla v(\mathbf{r}_1, \mathbf{r}_2) \, d\mathbf{r}_2 \tag{4.5.7}$$

to approximate $\rho^{(2)}(\mathbf{r}_1, \mathbf{r}_2, t)$ in terms of $\rho(\mathbf{r}, t)$. Inserting this into Eq. (4.5.4) and recalling (4.1.12) and (4.2.3) we obtain:

$$\frac{\partial \rho(\mathbf{r}, t)}{\partial t} = \Gamma \nabla \left[\rho(\mathbf{r}, t) \nabla \frac{\delta F[\rho(\mathbf{r}, t)]}{\delta \rho(\mathbf{r}, t)} \right], \tag{4.5.8}$$

where $F[\rho(\mathbf{r}, t)]$ is the equilibrium fluid Helmholtz free energy functional. This result and its generalisation to a two component mixture is used in chapter 7 to describe the dynamics of droplets of evaporating colloidal suspension.

Chapter 5

Monte Carlo

In 1953 the paper "Equation of State Calculations by Fast Computing Machines" [5] was published by Nicholas Metropolis, Arianna W. Rosenbluth, Marshall N. Rosenbluth, Augusta H. Teller and Edward Teller. The algorithm described in this paper is now known as the Metropolis Monte Carlo algorithm, even though "Metropolis played no role in its development other than providing computer time" [22]. The theoretical work was done by Marshall Rosenbluth. The method was later generalised by Wilfred K. Hastings in 1970 [23].

A Monte Carlo (MC) simulation does not evolve forward in time using equations of motion, such as Newton's equations of motion. Instead it is event driven and uses random numbers in order to generate a sequence of configurations drawn from a relevant probability distribution. A different sequence of numbers may lead to different system trajectories but if sufficient simulations are carried out the distribution will be properly sampled and the quantities resulting form the simulation will be statistically similar. Monte Carlo simulations can be used for a wide variety of problems ranging from data analysis to simulating quantum systems. In statistical mechanics we can use MC as a statistical evolution algorithm to sample a phase space, which evolves the system along a trajectory in phase space over time. This enables us to obtain a thermal average of a many particle system.

5.0.1 Markov chains

A Markov chain is a sequence of states where the probability of the next states depends only on the current state. The transition state probability from state α to state β of a Markov process is

$$w_{\alpha \to \beta} = P(S_\beta, t | S_\alpha, t - 1) \qquad (5.0.1)$$

where S_β is the state of the system at time t and S_α is state at time $t - 1$. The transition probability also requires

$$w_{\alpha \to \beta} \geq 0, \quad \sum_\beta w_{\alpha \to \beta} = 1. \qquad (5.0.2)$$

5.0.2 Metropolis Hastings

The Metropolis-Hastings Monte Carlo algorithm is a Markov chain MC method for obtaining a sequence of random samples from a probability distribution. It can be used to draw samples from any probability distribution $P(x)$ given a function, $g(x)$, that is proportional to the density of P. Metropolis-Hastings is particularly useful for approximating distributions that are difficult to sample directly.

For our purposes we use the Metropolis-Hastings algorithm for sampling the Boltzmann distribution of the system. In this case, recall from Eq. (3.1.1) the probability of being in a given state is

$$f_{\text{state}} = \frac{e^{-E_i/k_B T}}{Z}. \qquad (5.0.3)$$

In the practical implementation of the algorithm for our problem we only need a function that is proportional to the probability distribution, which means we do not need to evaluate the partition function, Z, and we can use the probability distribution $g(x) = e^{-\beta H}$. The specific steps for the Metropolis algorithm are described in the next chapter in section 6.2 but the basic idea is to initialise states of the lattice fluid on the three dimensional grid. Allowed random changes of state are then considered at points on the grid and the change in the energy is evaluated. If the move results in a lower energy, the change is accepted. If the

change results in an increase in energy this is accepted with the probability $e^{-\beta \Delta E_i}$, where ΔE_i is the change in the energy. The event clock is advanced and the procedure is repeated.

The Metropolis algorithm, with a suitable time scaling, produces results in good and fair agreement with Brownian dynamics [24] for both 1D analytical results and 3D colloid suspension simulations for metastable fluids crystallising. Thus, one can use MC to study equilibrium dynamics and in fact also non-equilibrium dynamics, as we show later.

Chapter 6

Modelling the evaporation of nanoparticle suspensions from heterogeneous surfaces

We present a Monte Carlo (MC) grid-based model for the drying of drops of a nanoparticle suspension upon a heterogeneous surface. The model consists of a generalised lattice-gas in which the interaction parameters in the Hamiltonian can be varied to model different properties of the materials involved. We show how to choose correctly the interactions, to minimise the effects of the underlying grid so that hemispherical droplets form. We also include the effects of surface roughness to examine the effects of contact-line pinning on the dynamics. When there is a 'lid' above the system, which prevents evaporation, equilibrium drops form on the surface, which we use to determine the contact angle and how it varies as the parameters of the model are changed. This enables us to relate the interaction parameters to the materials used in applications. The model has also been applied to drying on heterogeneous surfaces, in particular to the case where the suspension is deposited on a surface consisting of a pair of hydrophilic conducting metal surfaces that are either side of a band of hydrophobic insulating polymer. This situation occurs when using inkjet printing to manufacture electri-

cal connections between the metallic parts of the surface. The process is not always without problems, since the liquid can dewet from the hydrophobic part of the surface, breaking the bridge before the drying process is complete. The MC model reproduces the observed dewetting, allowing the parameters to be varied so that the conditions for the best connection can be established. We show that if the hydrophobic portion of the surface is located at a step below the height of the neighbouring metal, the chance of dewetting of the liquid during the drying process is significantly reduced.

6.1   Introduction

How ink or paint dries, i.e. how liquid droplets containing nanoparticles deposited on a surface evolve in time as the liquid evaporates has significant relevance in modern manufacturing. Inkjet deposition is increasingly used during the manufacture of functional nano-structured materials. An innovative recent example is the application described in [25] which uses inkjet printing as part of a new method for constructing solar panels. This includes making the electrical interconnections after the various different layers that form a solar cell have been laid down on the glass substrate and then scribed using laser ablation [25]. The benefits of using inkjet printing include reduced costs, wastage and potentially improved performance. Several parts of the structure are inkjet printed. An insulating polymer layer can be formed by depositing an ink that consists of a polymer solution. Another ink consists of a suspension of conducting metal nanoparticles. As the solvent evaporates, the goal is for the remaining nanoparticles to form an electrically conducting connection over the surface.

The surface onto which the nanoparticle ink is printed consists of two materials: (i) a metal conducting surface that is either side of (ii) a strip of a polymer insulating material. The metallic part of the surface is hydrophilic and the polymeric part is hydrophobic. When the liquid is deposited onto these two materials side-by-side, there is a tendency for the liquid to dewet from the surface of the insulator and move onto the metal, since this reduces the
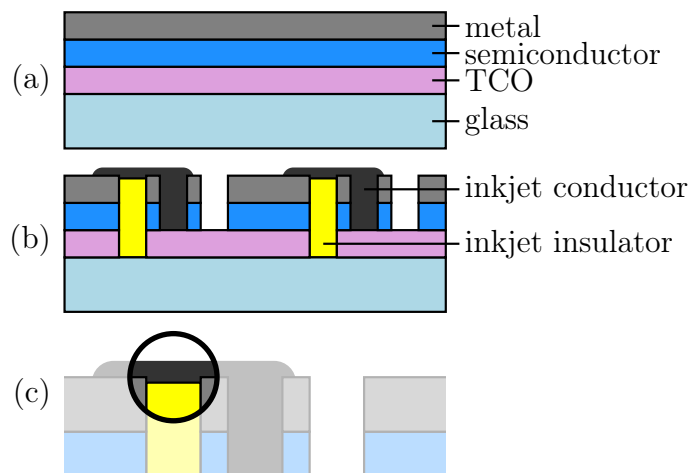
Figure 6.1: Illustration of the solar cell manufacturing process developed in Ref. [25], which uses inkjet printing. In the initial stage (a), three layers are deposited in sequence onto a glass substrate. The first is a transparent conducting oxide (TCO) layer, then the semiconductor and finally a metallic layer. Then, trenches are made by depth selective laser scribes. Following this, the insulating polymer and conductive inks are deposited, as shown in (b). When the process is complete, the conductive ink should form a conducting connection between the TCO at the bottom of one cell and the metal on the top of the neighbouring cell, bridging the insulating polymer. In (c) we display a zoom of the conducting connection that we model here.

energy of the system. In the solar cell manufacturing process [25], this insulating polymer strip is created by inkjet printing into a trench created on the surface by laser ablation, at a previous stage — see Fig. 6.1.

If the nanoparticle suspension deposited perpendicular to the polymer strip is to dry to form an electrical connection, it is crucial that the ink does not dewet from the hydrophobic surface. The aim of the present work is to understand when this dewetting occurs and also to determine if there are processes that can be done during manufacturing to prevent dewetting.

The specific example considered is a particular case of a more general class of problem: that of modelling the evaporation of a nanoparticle suspension from a heterogeneous surface. The deposition and drying of the ink involves processes that occur over a huge range of time and length scales. The procedure can be roughly split into two parts: (i) the process of the ink being sprayed from the print head and arriving at the surface and (ii) the behaviour of the ink as it dries, once it is on the surface. In our work, we focus solely on stage (ii), in

which there are still processes that occur over a great range of length and time scales.

The nanoparticles move throughout the liquid with a diffusive dynamics, where changes occur on a time scale much larger than the time scale for rearrangements of the solvent molecules. Drop shape changes occur on a time scale that is very much larger than the molecular time scale and also the nanoparticle diffusive time scale. There are also several disparate length scales, ranging from the solvent molecular diameter scale, to the size of the nanoparticles, the scale of any surface structures and then largest of all, the liquid drop size. Because of this, modelling such a multi-scale system has many challenges. Mesoscopic thin-film partial differential equation based models can be used [26, 27, 28, 29, 30, 31] but relating properties of the microscopic interactions between the particles and the structures they form in the liquid is not straightforward, because this type of model describes the distribution of the nanoparticles over the surface via a height-averaged concentration profile. This does not allow for a description of the variations in the nanoparticles density distribution in the direction perpendicular to the surface. A fully microscopic approach, such as molecular dynamics (MD) does include every aspect of the motion of the particles and can be used to describe small liquid drops on a surface [32, 33, 34, 35]. Generally MD is computationally infeasible even for moderate system sizes due to the long time scales over which the evaporative drying occurs. Similarly, classical density functional theory (DFT) [20, 2, 3] and dynamical DFT [7, 8, 36, 6] can describe in great detail the density profile of the liquid at the interface and the structure down to the scale of individual particles [2, 3, 37, 38, 39] but the level of detail makes this also computationally very expensive.

We require a coarse-grained model to describe the fluid dynamical processes of interest here but not to the degree of coarse-graining as is present in the thin-film equation based models. Thus, we develop a lattice model for the system using Monte Carlo (MC) to capture the non-equilibrium dynamics and model the system time evolution as a series of discrete events. We model the nanoparticles individually, incorporating in the model their diffusion through the liquid over time thus enabling a description of the structures they may form

on the surface. However, instead of modelling every solvent molecule individually, we group them together and statistically model them by a single, larger effective 'particle' of the same size as the nanoparticles, also residing on a lattice. MC models of this type have been used before, initially by treating the system effectively in two dimensions [40, 41, 42, 43]. However, more recently models that are fully three-dimensional have been used [44, 45, 46, 47, 48]. Our model here is of this kind but differs from previous studies in the manner in which we describe the particle interactions, allowing for correct modelling of the (hemispherical) liquid drop shape. Additionally, the effect of surface roughness is incorporated.

How a liquid wets a surface is characterised by the *spreading parameter s* [14]. It is defined as the difference in the surface tensions between the liquid, gas and the substrate:

$$s = \gamma_{\text{sg}} - (\gamma_{\text{sl}} + \gamma_{\text{lg}}). \tag{6.1.1}$$

The first term, γ_{sg}, is the excess free energy per unit area of the substrate when dry (i.e. in contact with the gas phase), referred to as the solid-gas interfacial tension. The second term is the excess free energy per unit area of the substrate when it is wet by a thick film of the liquid and is the sum of the solid-liquid interfacial tension γ_{sl} and the liquid-gas interfacial tension γ_{lg}. When $s > 0$ the liquid seeks to spread over the surface. In contrast, when $s < 0$ the liquid only partially wets the substrate, forming a drop with contact angle θ. Young's equation [14] relates the contact angle θ to the interfacial tensions

$$\gamma_{\text{lg}} \cos \theta = \gamma_{\text{sg}} - \gamma_{\text{sl}}. \tag{6.1.2}$$

Therefore, the contact angle and spreading parameter are related by $s = \gamma_{\text{lg}}(\cos \theta - 1)$. From our simulation results we can calculate the contact angle and also determine how this depends on the parameters in our model. Thus, to model a particular experiment, we have to find the contact angle of the solvent on the particular material(s) in the substrate (many are available in the literature) and then we select our model parameters to match the experiments.
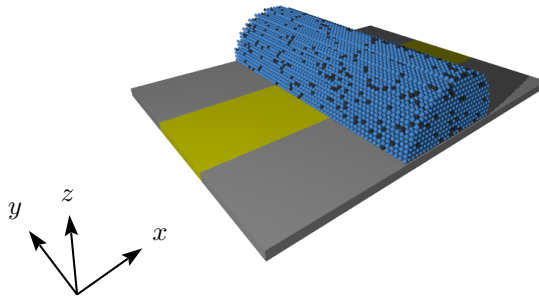
Figure 6.2: An example of a simulation starting condition. The liquid (blue) is initiated in a semi-circular strip connecting the conductive metal surfaces. Nanoparticles (black) are randomly dispersed throughout the liquid. The metal surface (in grey) can be elevated above the insulating portion in the middle (yellow), but in the case displayed here is not.

The remainder of this chapter is laid out as follows: In Sec. 7.2 we describe our model and the MC algorithm for the dynamics. This section also presents results for the model when no nanoparticles are present, to illustrate the wetting behaviour of the pure solvent liquid on a uniform planar surface. We determine the dependance of the contact angle on the model parameters, to enable selecting values to match experiments. In Sec. 6.3 we briefly present the bulk solvent fluid phase diagram. In Sec. 6.4 we present results for droplets containing nanoparticles evaporating from a smooth planar surface and also show how to include the effect of surface roughness by changing the fluid dynamics in the vicinity of the surface. Sec. 6.5 presents results for the drying of the nanoparticle suspension from a heterogeneous surface, with emphasis on the drying of liquid bridges spanning a hydrophobic patch. Finally, in Sec. 7.7 we make a few concluding remarks.

6.2 Lattice model for the system

The system is discretised onto a regular three dimensional grid with lattice spacing σ and with periodic boundary conditions in the x and y coordinates. The surface of the substrate onto which the nanoparticle suspension (ink) is deposited is perpendicular to the z direction.

Ink cannot penetrate the surface. At the top of the simulation box, at $z = L$, we apply various different boundary conditions, discussed below. A typical starting configuration is displayed in Fig. 6.2. Each lattice site above the surface can be in one of three states: (i) empty, (ii) containing a nanoparticle or (iii) containing liquid. We refer to a lattice site containing liquid as containing a liquid 'particle', but it should be borne in mind that this does not mean an individual solvent molecule but rather many of them grouped together in a volume σ^3. The lattice constant σ is most easily envisaged as being the diameter of the nanoparticles but this does not have to be so: one can also consider σ to be a larger coarse-graining length scale, in which case when a lattice site is said to be 'containing' a nanoparticle, we mean 'contains mostly nanoparticles'.

We define $n_{\mathbf{i}}$ and $l_{\mathbf{i}}$ to be the occupation numbers of lattice site $\mathbf{i}$ for nanoparticles and liquid respectively, where

$$\mathbf{i} = (i, j, k) \tag{6.2.1}$$

is the discrete position vector (c.f. Fig. 6.2). If site $\mathbf{i}$ is occupied by liquid, then $l_{\mathbf{i}} = 1$, otherwise $l_{\mathbf{i}} = 0$. Similarly, if site $\mathbf{i}$ is occupied by a nanoparticle then $n_{\mathbf{i}} = 1$ and $n_{\mathbf{i}} = 0$ if there is no nanoparticle. Liquid and a nanoparticle cannot occupy the same site.

We model the total energy of the system E by the following sum:

$$
\begin{aligned}
E = -\sum_{\mathbf{i},\mathbf{j}} & \left(\frac{\varepsilon_{nn}}{2} c_{\mathbf{ij}} n_{\mathbf{i}} n_{\mathbf{j}} + \varepsilon_{nl} c_{\mathbf{ij}} l_{\mathbf{i}} n_{\mathbf{j}} + \frac{\varepsilon_{ll}}{2} c_{\mathbf{ij}} l_{\mathbf{i}} l_{\mathbf{j}} \right) \\
& - \mu \sum_{\mathbf{i}} l_{\mathbf{i}} + \sum_{\mathbf{i}} V_{\mathbf{i}}^{l} l_{\mathbf{i}} + \sum_{\mathbf{i}} V_{\mathbf{i}}^{n} n_{\mathbf{i}}.
\end{aligned}
\tag{6.2.2}
$$

The first term, a sum over pairs of lattice sites, is the contribution from particle interactions. The overall strength of the interactions between pairs of nanoparticles is determined by the parameter ε_{nn}, between liquid and nanoparticles by ε_{nl} and between pairs of liquid particles by ε_{ll}. The precise value of the interaction energy between pairs of particles at sites $\mathbf{i}$ and $\mathbf{j}$ is determined by the dimensionless coefficient $c_{\mathbf{ij}}$, which decreases in value as the distance

between the pair of particles increases. We use the following values

$$
c_{\mathbf{ij}} = \begin{cases} 1 & \mathbf{j} \in \{\text{NN } \mathbf{i}\} \\ \dfrac{3}{10} & \mathbf{j} \in \{\text{NNN } \mathbf{i}\} \\ \dfrac{1}{20} & \mathbf{j} \in \{\text{NNNN } \mathbf{i}\} \\ 0 & \text{otherwise} \end{cases} \tag{6.2.3}
$$

where NN $\mathbf{i}$, NNN $\mathbf{i}$ and NNNN $\mathbf{i}$ stand for nearest neighbours, next nearest neighbours and next-next nearest neighbours of site $\mathbf{i}$, respectively. Thus, we truncate all interactions for $|\mathbf{i} - \mathbf{j}| > \sqrt{3}\sigma$. The influence on the wetting behaviour of truncating the range of the interactions is discussed in Refs. [38, 39].

The choice of particular values in Eq. (6.2.3) is important, as this leads to liquid droplets on the surface having a hemispherical shape. For example, if instead we set $c_{\mathbf{ij}} = 0$ for $\mathbf{j} \in$ NNN $\mathbf{i}$ and $\mathbf{j} \in$ NNNN $\mathbf{i}$, (i.e. just nearest neighbour interactions) then the system forms unrealistic rectangular shaped droplets, particularly at low temperatures. Thus, with the values in Eq. (6.2.3) the dependence of the gas-liquid surface tension on the orientation of the interface with respect to the grid is minimised. That one should select the particular values in Eq. (6.2.3) comes from noting that the sum over neighbours in Eq. (6.2.2) has the same form as a finite difference approximation for the Laplacian [49]. It can be shown that the values for $c_{\mathbf{ij}}$ given in Eq. (6.2.3) minimise the errors from discretising the Laplacian on the grid [50], dictating the choice in Eq. (6.2.3)[1]

The second term in Eq. (6.2.2) is the contribution from treating the liquid as being coupled to a reservoir, which is the vapour above the surface. μ is the chemical potential of the vapour. The value of μ determines the rate at which the liquid evaporates from the surface. The last two terms of Eq. (6.2.2) are the contribution from the interaction with

---

[1]In addition to leading to hemispherical droplets, we expect the particular values for $c_{\mathbf{ij}}$ in Eq. (6.2.3) to result in the roughening transition [51, 52] temperature to be suppressed. Indeed, at all the temperatures for which we have performed simulations, we have seen no evidence of a roughening transition. The roughening transition temperature is the value where the free energy barrier that much be surmounted to add a new layer to the substance becomes negligible. Thus, above this temperature the interfacial fluctuations are greater.

the surface, where $V_{\mathbf{i}}^l$ and $V_{\mathbf{i}}^n$ are the external potentials due to the surface exerted on the liquid and the nanoparticles, respectively. Assuming that the surface is composed of particles interacting with the fluid with interaction strength ε_{wl} and a pair potential of the same form as the pair potentials in Eq. (6.2.2), then for a flat structureless surface the potential takes the form

$$V_{\mathbf{i}}^l = \begin{cases} \infty & k < 1 \\ -12\varepsilon_{wl}/5 & k = 1 \\ 0 & \text{otherwise,} \end{cases} \qquad (6.2.4)$$

where k is the perpendicular distance from the surface. Similarly, if the interaction strength with the nanoparticles is ε_{wn}, then the external potential for the nanoparticles takes the same form as (6.2.4) but the suffix l is replaced by n.

The external potential in Eq. (6.2.4) is modified when the surface varies in height or if the material changes. For example, to model the situation illustrated in Fig. 6.1, since the polymer hydrophobic section of the surface is inkjet printed at an earlier stage, its surface height can be controlled. We denote the step in height from the polymer to the metal part of the surface, to be h.

In all that follows below, we non-dimensionalise and set ε_{ll} to be the unit of energy and the lattice spacing σ to be our unit of length. All other parameters are given in terms of these.

The Monte Carlo Algorithm

We denote a particular state of the system as $S_\alpha \equiv \{n_{\mathbf{1}}, n_{\mathbf{2}}, \ldots, l_{\mathbf{1}}, l_{\mathbf{2}}, \ldots\}$, i.e. a particular set of values of the occupation numbers, which we index with the label α. We also denote the probability of the system being in this state at time t as $P(S_\alpha, t)$. The time evolution of

this probability is given by the master equation

$$P(S_\alpha, t+1) = P(S_\alpha, t) - \sum_{\beta \neq \alpha} w_{\alpha \to \beta} P(S_\alpha, t)$$
$$+ \sum_{\beta \neq \alpha} w_{\beta \to \alpha} P(S_\beta, t) \tag{6.2.5}$$

where $w_{\alpha \to \beta}$ is the transition rate from state S_α to state S_β.

In equilibrium, where $P(S_\alpha, t+1) = P(S_\alpha, t)$, we have [53]:

$$\frac{w_{\alpha \to \beta}}{w_{\beta \to \alpha}} = e^{-\Delta E / k_B T} \tag{6.2.6}$$

where T is the temperature, k_B is Boltzmann's constant and $\Delta E = E(S_\beta) - E(S_\alpha)$, with the energy E given in Eq. (6.2.2). The following Metropolis Monte Carlo algorithm satisfies this [53]:

1. Pick a random particle.

2. Pick a random neighbouring site.

3. Calculate the change in energy, ΔE, from swapping these particles using Eq. (6.2.2).

4. If $\Delta E < 0$, perform the swap. Otherwise, swap the particles with probability $e^{-\Delta E / k_B T}$.

The assumption here is that even when the system is out of equilibrium, the transition rates given by Eq. (6.2.6) still hold, allowing us to use the algorithm to determine the non-equilibrium dynamics of the liquid.

This algorithm is refined for a system with both nanoparticles and liquid. To evolve the liquid, a random site on the lattice is picked. The MC algorithm described above is used, however any move involving a nanoparticle is forbidden during a liquid step.

The nanoparticles are modelled differently. Instead of selecting any random particle from the system, we keep an explicit list of nanoparticle positions and select a nanoparticle from this list to attempt the following dynamics: Firstly, to prevent nanoparticles from being

left floating when the surrounding liquid moves away, after selecting a nanoparticle, we first check if there is a vacancy in the lattice site below the chosen nanoparticle. If there is, the nanoparticle is moved down to that empty site, finishing the move. If the site below is non-empty or is part of the surface, we then perform a weighted sum over the neighbouring lattice sites to determine how much liquid there is in the vicinity of the nanoparticle. We calculate the quantity $\bar{l}_\mathbf{i} = \sum_\mathbf{j} c_\mathbf{ij} l_\mathbf{j}$, where the coefficients $c_\mathbf{ij}$ are the same as those used to calculate the energy, given in Eq. (6.2.3). If $\bar{l}_\mathbf{i} < 5/3$ then the nanoparticle move is rejected. Only if $\bar{l}_\mathbf{i} \geq 5/3$ we do allow the nanoparticle to move, swapping with one of the neighbouring liquid particles, as per steps 2–4 above. This is done to prevent excessive nanoparticle movement once most of the liquid has evaporated, since the physical origin of the nanoparticle dynamics is the Brownian motion due to being suspended in the liquid. If there are not enough liquid particles neighbouring the nanoparticle, then it remains stationary. The threshold value $5/3$ was determined empirically; a lower value makes the nanoparticles too mobile on the dry surface, but higher values leads to the formation of immobile nanoparticle clusters. Note that the algorithm described above for evolving the nanoparticles violates detailed balance. This is in keeping with previous MC models for systems of this kind [40, 41, 42] and is a consequence of the facilitated dynamics of the nanoparticles. Of course, for the liquid there is detailed balance.

Liquid and nanoparticles evolve at different rates. We perform M liquid steps for every nanoparticle step. This ratio determines the diffusion coefficient of the nanoparticles in the liquid [40, 41, 42]. We set the value of M to depend on the ratio of nanoparticles to non-nanoparticles in the system as:

$$M = \xi \frac{V - N\sigma^3}{N\sigma^3} \tag{6.2.7}$$

where V is the volume of the system and N is the total number of nanoparticles. For all simulations in this paper, we use a value of $\xi = 0.2$. For typical systems this corresponds to

a value of $M \approx 30$. Eq. (6.2.7) is required to prevent the nanoparticles "speeding up" as the liquid evaporates from the system, which decreases the ratio of liquid to nanoparticles.

Diffusion coefficient

In what follows the system is referred to as having evolved for a time of x Monte Carlo steps (MC steps), which means that there has been an attempted move on average x times per lattice site. To relate MC steps to the physical time scales, the diffusion coefficient of a single nanoparticle moving though the bulk liquid is determined.

This is calculated by running multiple simulations with a single nanoparticle in a system full of liquid. The distance r that the nanoparticle travels is recorded at certain time intervals. A plot of $\langle r^2 \rangle$ against the number of MC steps is then made. Note that $\langle \mathcal{P} \rangle$ denotes the statistical average of any quantity $\mathcal{P}$. Using the relation [54]

$$\langle r^2 \rangle = 6Dt \tag{6.2.8}$$

where D is the diffusion coefficient and t is time, the value of D can be determined from the gradient of the plot.

For a system with $\mu/\epsilon_{ll} = 6$ (a system filled with liquid), $k_B T/\epsilon_{ll} = 0.6$ and averaging over $10,000$ simulations, a value of $D = 2.6 \times 10^{-4} \, \sigma^2 \, \mathrm{MC} \, \mathrm{step}^{-1}$ was found. Thus, the Brownian timescale $\tau_B \equiv \sigma^2/6D = 650$ MC steps. τ_B is the time it takes on average for a nanoparticle to diffuse a distance of order its own diameter. We obtain a similar value at the higher temperature $k_B T/\epsilon_{ll} = 1.0$, since the value of D only starts to change when the temperature is high enough or the chemical potential is low enough that the density of the vacancies in the liquid becomes sizeable. Although we specify times below in units of MC steps, knowing the value of D allows to easily relate to the true timescales in a given system.
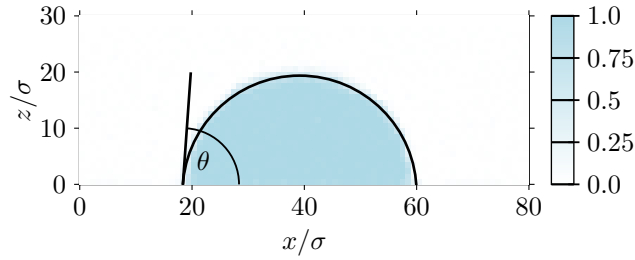
Figure 6.3: A density profile for a drop at equilibrium with $k_B T/\varepsilon_{ll} = 1$ and $\varepsilon_{wl}/\varepsilon_{ll} = 0.7$ obtained by averaging along the length of the liquid drop. The approximating circle used to estimate the contact angle is shown as the black line. This circle is calculated using the Taubin circle fitting method [55] on the boundary points of the profile.

Determination of contact angles

Once the system, such as that illustrated in Fig. 6.2, has reached equilibrium we can measure the contact angle. This is done by taking an average along the length of the liquid ridge in the y-direction (c.f. Fig. 6.2). We average over the configurations of a liquid ridge instead of a hemispherical drop because this is easier to measure and gives us more samples to average over. This average calculates a density profile $\rho_{\mathbf{i}} = \langle l_i \rangle$. From this density profile, we define the liquid drop to be where $\rho_{\mathbf{i}}\sigma^3 > 0.5$. We then fit a circle to the top portion of the boundary of the drop using the Taubin circle fitting method [55], illustrated in Fig. 6.3. From this circle, it is then straightforward to determine the contact angle, which is the angle made with the surface. The density profile in Fig. 6.3 is for a system with temperature $k_B T/\varepsilon_{ll} = 1.0$ and wall attraction strength $\varepsilon_{wl}/\varepsilon_{ll} = 0.7$. The 0.7 value corresponds to a weakly hydrophilic interface and so the liquid does not spread and forms a drop with a contact angle $\approx 75°$. Increasing ε_{wl} decreases the contact angle, corresponding to the surface becoming more hydrophilic. On the other hand, decreasing ε_{wl} makes the surface hydrophobic.

In Fig. 6.4 we display a plot of the contact angle as the surface-liquid attraction strength ε_{wl} is varied, for the temperature $k_B T/\varepsilon_{ll} = 1.0$. In addition to results for this 'smooth' surface, we also include in Fig. 6.4 results for a 'rough' surface, discussed further below. We
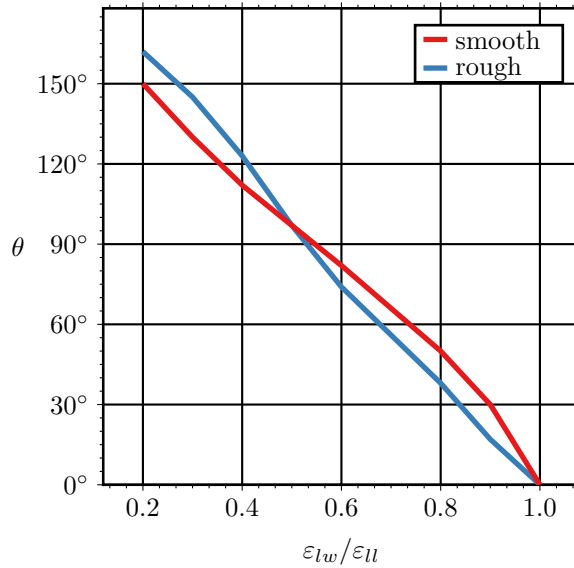
Figure 6.4: The contact angle θ plotted as a function of the surface attraction ε_{wl} with $k_B T/\varepsilon_{ll} = 1.0$, for both a smooth and a rough surface. We see that increasing the attraction due to the surface decreases the contact angle. When $\varepsilon_{wl} > \varepsilon_{ll}$, the drops wet the surface.

see that as the attraction strength increases, the contact angle decreases, until eventually at $\varepsilon_{wl} \approx \varepsilon_{ll}$ there is a wetting transition to a state where the liquid wets the surface, with contact angle 0°. For small values of ε_{wl} the surface only weakly attracts the liquid, corresponding to a strongly hydrophobic surface on which the drop takes a shape that is close to a full circle, with a large contact angle. Owing to the way we define the wall potential, the contact angle plot in Fig. 6.4 varies only weakly with the temperature in the range $0.6 < k_B T/\varepsilon_{ll} < 1.2$, the range in which most of our results are calculated. At higher temperatures, one should expect the wall attraction strength for wetting to be lower. However, at higher temperatures the interfacial fluctuations become significant and the system is no longer in the regime relevant to modelling the drying of inkjet printed drops. At lower temperatures (results not displayed), the simulations become slow and the system becomes hard to equilibrate.

We also display in Fig. 6.4 the contact angle obtained for the liquid on a rough surface. This surface is physically rough on the scale of the lattice, modelled by randomly raising and

lowering respectively one third of the blocks on the surface by one lattice spacing σ. When the wall is sufficiently attractive, for $\varepsilon_{wl}/\varepsilon_{ll} > 0.5$, this generates a surface that contains many pits, into which liquid condenses (from the vapour) and becomes trapped. This makes the surface effectively more attractive and so the contact angle in this regime is decreased, compared to the smooth surface. However, for $\varepsilon_{wl}/\varepsilon_{ll} < 0.5$ the surface roughness makes the surface more hydrophobic and with a larger contact angle than the smooth surface with the corresponding value of ε_{wl}. This is the well-known lotus effect used to create superhydrophobic surfaces via surface roughness [56, 57, 58, 14].

6.3 Bulk solvent phase behaviour

Understanding the behaviour of the liquid in equilibrium gives us insight into how the liquid behaves out of equilibrium. Calculating the binodal allows us to pick parameters that correspond to a suitably high density liquid phase coexisting with low density vapour phase.

The binodal gives the coexisting density values for a system in equilibrium. Two coexisting phases have the same chemical potential, temperature and pressure in each phase.

Since we do not need to know the binodal densities with great accuracy we calculate the binodal by performing simulations in a long, narrow box of size $10\sigma \times 10\sigma \times 80\sigma$, with periodic boundary conditions, treated in the canonical ensemble. Initially one end of the box is filled with liquid particles, with the other half being empty. The simulation then equilibrates in a state with half the system in the liquid phase, coexisting with the other half containing the vapour.

To estimate the density of the two coexisting phases we first calculate the mean density ρ_i of each $10\sigma \times 10\sigma$ layer of the box. The layer densities are then split into two groups: those with $\rho_i > 0.5$ and those with $\rho_i < 0.5$. In each of these groups the statistical outliers are eliminated, since these are layers that correspond to the interface between the gas and the liquid. Then the mean of the remainder in each group is used as the density on the binodal.
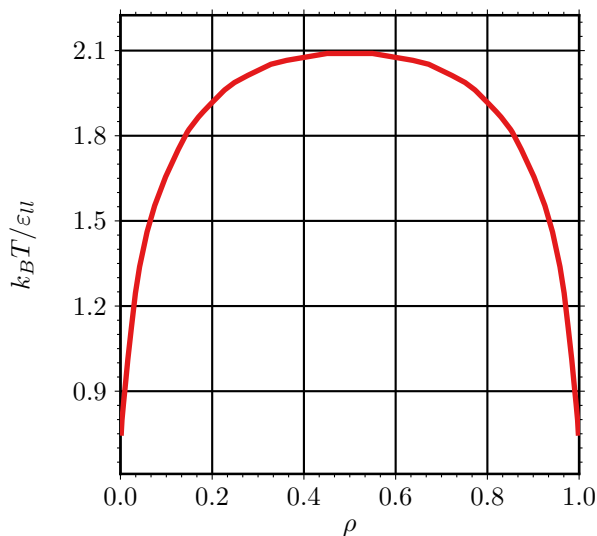
Figure 6.5: The bulk fluid binodal, which gives the densities of the coexisting gas and liquid phases as the temperature is varied.

The result of this approach, over a range of temperatures, yields the binodal displayed in Fig 6.5. For example, when $k_BT/\varepsilon_{ll} = 0.9$ the density of the coexisting liquid and vapour is $\rho_l = 0.99$ and $\rho_g = 0.01$.

In the vicinity of the critical temperature T_c, the binodal can not be calculated with any great accuracy using the approach described above, due to the fact that the average densities of the two coexisting phases become rather similar and also because the system is strongly fluctuating with a diverging correlation length at T_c [3, 53]. The top of the binodal curve displayed in Fig. 6.5 was estimated by inspecting the histogram of densities $\rho_{\mathbf{i}}$ in each layer. Below the critical temperature, this histogram has two distinct maxima, corresponding to the two phases. We use the density value at each of these maxima as our estimate for the densities of the two coexisting phases. For $T > T_c$, the density histogram has only one maximum, at $\rho_{\mathbf{i}} = 0.5$. Based on this method we find that the critical temperature is $k_BT_c/\varepsilon_{ll} = 2.08 \pm 0.02$.

6.4   Evaporating droplets

For evaporation to occur, the statistical mechanics of the system must be done in the semi-grand canonical ensemble: the liquid is treated grand canonically, whilst the nanoparticles are dealt with canonically. The liquid is treated grand canonically because the vapour above the drop acts as a reservoir with chemical potential μ, with which the system can exchange particles, allowing the number of liquid particles in the system to vary over time. This is achieved by periodically setting the density of the top layer of the system to the low density result $\rho_{\mathbf{i}} \approx e^{\beta\mu}/(1 + e^{\beta\mu})$ [59, 38]. This enables the removal of particles from the system as the liquid drop evaporates. In contrast, the nanoparticles are treated canonically, since the number of nanoparticles in the system is fixed over time. In contrast, as discussed above, in order to determine the contact angle of a drop of liquid on the surface, we must treat it canonically, with a fixed number of liquid particles in the system.

We initiate the system with a fraction ϕ of the liquid particles replaced by nanoparticles. Fig. 6.6 shows the evaporation of a droplet containing nanoparticles with initial concentration $\phi = 0.15$. The substrate area is $120\sigma \times 120\sigma$ and the height of the top of the simulation box above the substrate is 80σ. The initial droplet consists of a hemisphere with a radius of 40σ with the vertical part linearly scaled to have a height of 24σ. The chemical potential is $\mu/\varepsilon_{ll} = -9$ and temperature $k_B T/\varepsilon_{ll} = 0.8$ which corresponds to an equilibrium vapour with a density $\rho_g = 0.001$. The interaction parameters are $\varepsilon_{lw}/\varepsilon_{ll} = \varepsilon_{nw}/\varepsilon_{ll} = 0.8$, $\varepsilon_{ln}/\varepsilon_{ll} = 1.25$ and $\varepsilon_{nn}/\varepsilon_{ll} = 1.5$.

The drop in Fig. 6.6 initially spreads to cover a greater area of the surface, since the starting configuration does not have the equilibrium contact angle. However, over time, liquid evaporates and the drop reduces in volume and so subsequently the area of the surface covered by the drop decreases – i.e. the contact line initially advances and then later recedes. Owing to the smooth surface, the drop retains a dynamic contact angle that is close in value to the equilibrium contact angle throughout most of the time evolution. Since the nanoparticles are attracted to the liquid they generally follow the liquid.
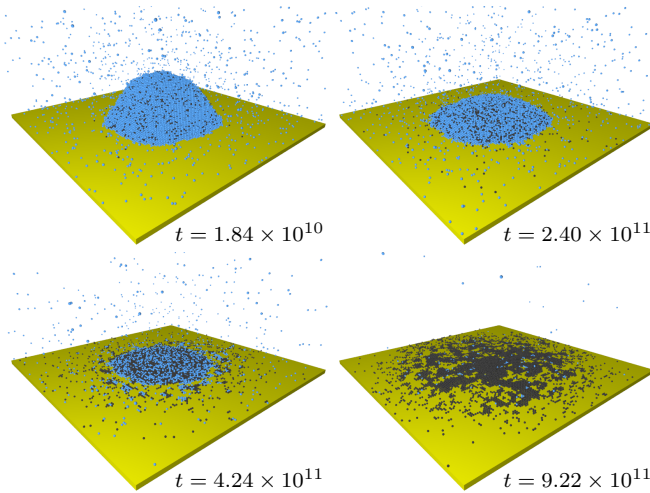
Figure 6.6: Droplet evaporation simulation, for $k_B T/\varepsilon_{ll} = 0.8$, $\mu/\varepsilon_{ll} = -9$, $\phi = 0.15$, $\varepsilon_{nn}/\varepsilon_{ll} = 1.5$, $\varepsilon_{nl}/\varepsilon_{ll} = 1.25$, $\varepsilon_{lw}/\varepsilon_{ll} = \varepsilon_{nw}/\varepsilon_{ll} = 0.8$ in a system with surface area $120\sigma \times 120\sigma$ and box height 80σ. Times, in units of MC steps, are given at the bottom right of each snapshot. After most of the liquid has evaporated, the nanoparticles diffuse out over the smooth surface, with dynamics facilitated by the small, but non-zero, vapour density.

After most of the liquid has evaporated there is then a further spreading of nanoparticles over the surface. Because of the smoothness of the surface and the non-zero vapour density, the residual liquid facilitates a diffusive dynamics that allows the nanoparticles to spread out over the surface to a state where the average distance of the nanoparticles from the centre of the system is larger than when the liquid is present.

Surface roughness

The roughness of surfaces is known to play an important role in how liquids spread. Surface roughness can hinder contact line motion over the surface and can lead to significant differences between the advancing, receding and equilibrium contact angles [14]. We consider two different methods of modelling the effect of surface roughness. The first is to introduce a dynamic rule that forbids moves parallel to the surface for all particles in contact with the surface. This is equivalent to a no-slip boundary condition. Thus, for a contact line to advance, particles in the second layer of lattice sites or higher above the surface must
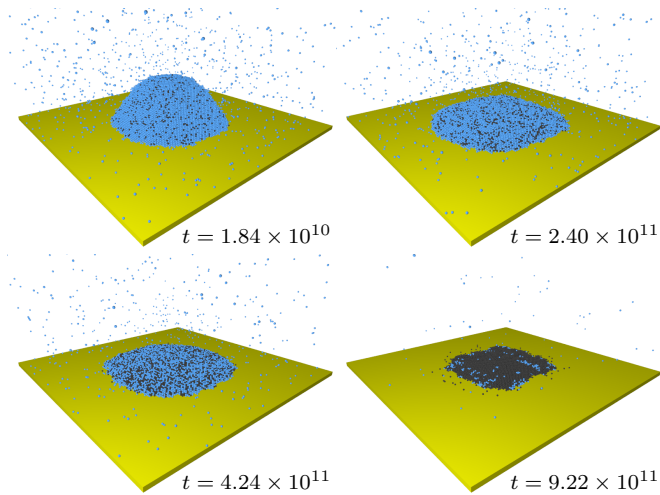
Figure 6.7: Snapshots of a liquid drop evaporating from a rough surface, with surface roughness modelled by incorporating a no-slip dynamic rule preventing motion at the surface being parallel to the surface. These are for the same times and parameter values as the smooth surface results in Fig. 6.6.

advance and then drop down to wet the dry surface ahead of the spreading droplet.

Fig. 6.7 shows snapshots from a simulations with the same parameter values as the evaporation simulation in Fig. 6.6 but with the no-slip dynamical rule forbidding moves across the surface. The droplet still spreads to a cover an area similar to that in the case with the smooth surface – i.e. to a value similar to that dictated by the equilibrium contact angle for this particular value of ε_{wl}. We then find that once most of the liquid has evaporated, the nanoparticles are left in an almost uniform circle which has a slightly larger radius than the original drop. There is also no further spreading out over the surface, even though the vapour density is still non-zero.

We have also investigated droplet evaporation from the rough surface considered at the end of Sec. 7.2 that is physically rough on the scale of the lattice, made by randomly setting the height of the surface to be 0 or $\pm\sigma$, each with equal probability. Results for this surface are displayed in Fig. 6.8. Recall that for $\varepsilon_{wl}/\varepsilon_{ll} > 0.5$ the contact angle is less than on the corresponding flat surface (see Fig. 6.4). This second approach to modelling surface roughness generates a wall that contains many pits, within which liquid becomes trapped.
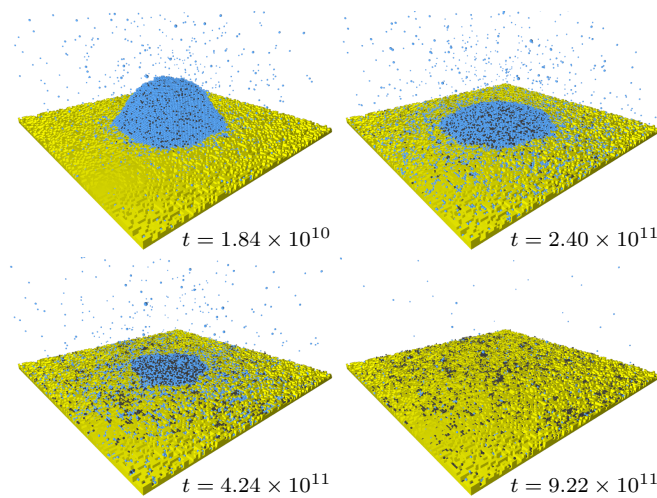
Figure 6.8: Snapshots of a liquid drop evaporating from a rough surface, the effect of which is modelled by setting the height of the surface to randomly be 0 or $\pm\sigma$, each with equal probability. These are for the same times and parameter values as the cases in 6.6 and Figs. 6.7.

This leads to a much higher amount of liquid remaining adsorbed on the surface than in the cases in Figs. 6.6 and 6.7. The adsorbed liquid facilitates the spreading of the nanoparticles over the surface out to distances well beyond where the liquid droplet was located. Whilst this facilitated dynamics is interesting, it is not what is observed on the experimental surfaces of interest here.

In Fig. 6.9 we display a plot of the mean distance $\langle r \rangle$ of the nanoparticles from the centre of the system (the centre of where the droplet was initiated) as a function of time for the three different surface roughness cases. Initially the average radius increases due to the droplet spreading in order to try and reach the equilibrium contact angle. However, except in the case where we model the surface roughness via the no-slip dynamic rule, once the liquid has evaporated, $\langle r \rangle$ further increases because the nanoparticles continue to spread out over the surface, facilitated by the vapour of liquid particles. The plateau value of $\langle r \rangle$ for the physically rough surface (Fig. 6.8) is even greater than the smooth surface case (Fig. 6.6) due to the higher amount of liquid adsorbed on the surface, in the surface pits. Eventually, $\langle r \rangle$ tends to a constant value as the spreading nanoparticles become trapped in the pits in
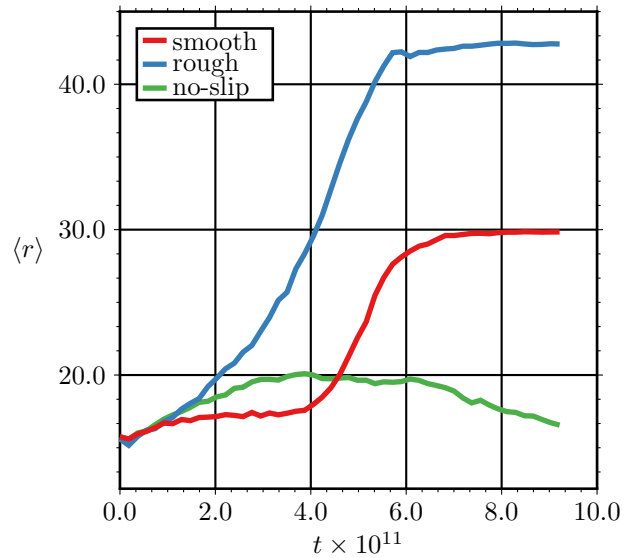
Figure 6.9: Plot of the average distance of the nanoparticles from the centre over time, for the three cases of (i) a smooth surface [Fig. 6.6], (ii) a rough surface where the effect of the surface roughness is modelled by a no-slip dynamic rule [Fig. 6.7] and (iii) surface roughness modelled by making the surface height randomly higher/lower than the average [Fig. 6.8].

the surface. For the case with the no-slip dynamic rule modelling surface roughness, as the droplet spreads and evaporates, $\langle r \rangle$ reaches a maximal value at around $t = 4 \times 10^{11}$. It then decreases slightly as the droplet contact line starts to recede, due to the droplet volume being decreased by the evaporation.

The results in Figs. 6.7 and 6.9 show that incorporating the effects of surface roughness via the no-slip dynamical rule seems to model the required physics. It also has the additional advantage of not introducing an additional length scale to be considered, namely the length scale of the surface roughness. Thus, this is the model we adopt henceforth to model the effects of surface roughness.

6.5 Modelling the ink drying process

Evaporating liquid bridge over a hydrophobic strip

In Fig. 6.10 we display snapshots as the liquid evaporates from a surface containing a hydrophobic strip. The interaction parameters are given in the figure caption. The surface is smooth – i.e. we do not implement the no-slip dynamical rule. The chemical potential in the vapour is set to be $\mu/\varepsilon_{ll} = -6$, which corresponds to the vapour phase being the thermodynamic equilibrium state, so the liquid seeks to evaporate from the surface. The substrate is made of a central hydrophobic strip of width 20σ (coloured yellow) which we denote region A, with $\varepsilon_{wl}^{\mathrm{A}}/\varepsilon_{ll} = \varepsilon_{wn}^{\mathrm{A}}/\varepsilon_{ll} = 0.4$, i.e. only weakly attracting the liquid and the nanoparticles. From Fig. 6.4 we see that on this part of the surface the liquid has contact angle $\theta \approx 110°$. Either side of this (coloured grey) is region B, where the surface is hydrophilic, having attraction strength parameters $\varepsilon_{wl}^{\mathrm{B}}/\varepsilon_{ll} = \varepsilon_{wn}^{\mathrm{B}}/\varepsilon_{ll} = 0.8$, corresponding to $\theta \approx 60°$. When there is no step in height from region B to region A ($h = 0$), then Fig. 6.10 shows that during the drying, the liquid dewets from the hydrophobic part of the surface, breaking the nanoparticle bridge at time $t \approx 1.2 \times 10^{12}$ MC steps. When there is a small step of height $h = \sigma$ (results not displayed), then the behaviour is similar, although the breaking of the bridge is slightly delayed. In contrast, a step of height $h \geq 2\sigma$ enables the liquid bridge to remain intact as it dries, so that a nanoparticle bridge is formed, spanning the hydrophobic part of the surface. The nanoparticle density is even slightly increased on the hydrophobic part of the surface when $h \geq 2\sigma$ (see Fig. 6.10).

The reason a step enables the liquid bridge to remain is that a corner is created into which the liquid is strongly attracted. The ability of corners and wedges to promote wetting by a liquid is well known [60, 61, 62, 63, 64, 65]. Since surface roughness can also modify the wetability of surfaces, a combination of steps and roughness can be used to control dewetting.

Fig. 6.11 shows results from a case when the nanoparticles are less strongly attracted to one another, which enhances the spreading over the hydrophilic part of this (smooth)
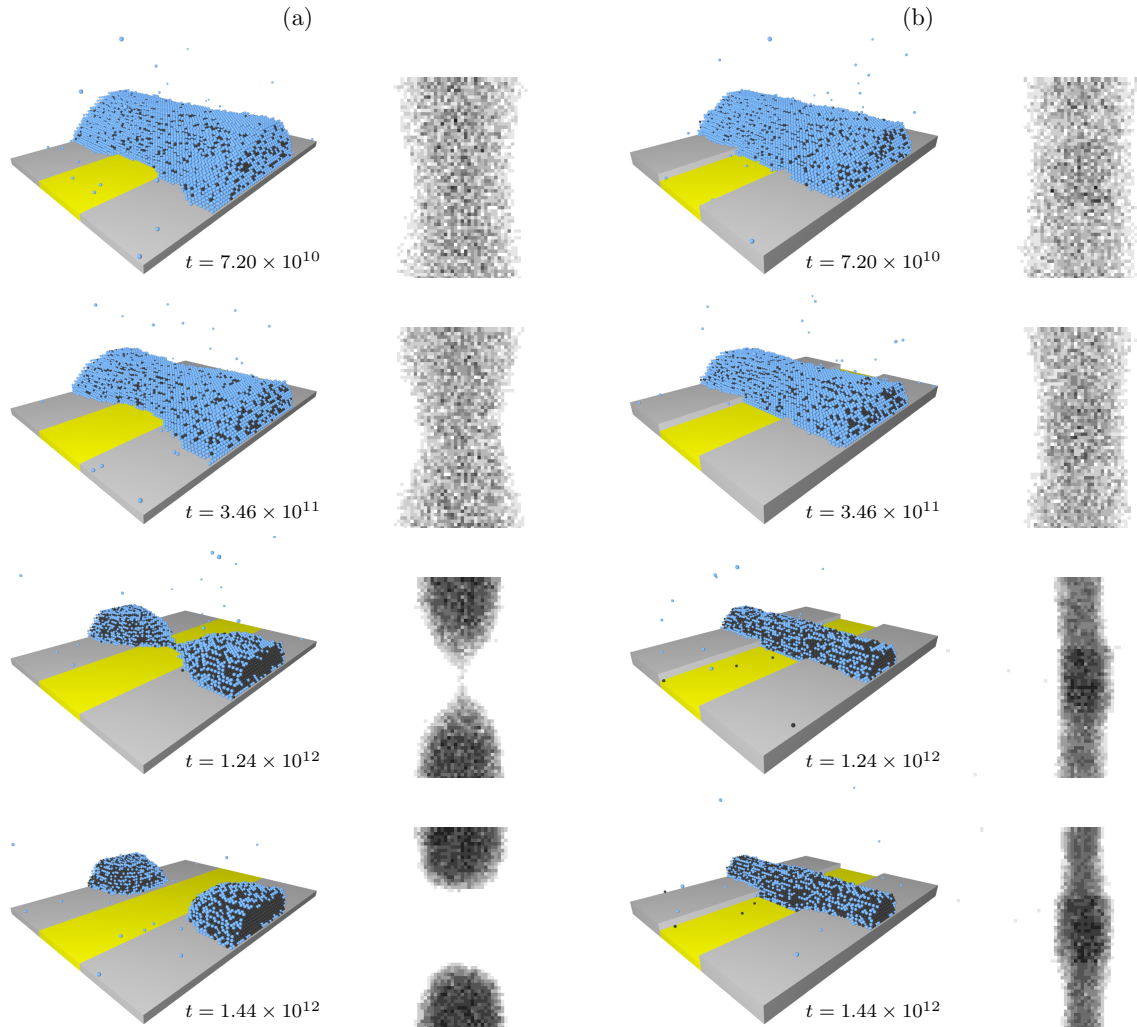
Figure 6.10: Time series from the drying of the liquid from the surface, when $\varepsilon_{nl}/\varepsilon_{ll} = 1.5$, $\varepsilon_{nn}/\varepsilon_{ll} = 2$, $\phi = 0.2$, $k_B T/\varepsilon_{ll} = 0.6$ and $\mu/\varepsilon_{ll} = -6$. The attraction strength with the hydrophobic yellow part A surface is $\varepsilon_{wl}^{A}/\varepsilon_{ll} = \varepsilon_{wn}^{A}/\varepsilon_{ll} = 0.4$, while the interaction with the grey part B strips either side has strength $\varepsilon_{wl}^{B}/\varepsilon_{ll} = \varepsilon_{wn}^{B}/\varepsilon_{ll} = 0.8$. On the right of each snapshot is the nanoparticles density distribution for that snapshot as viewed from above. The results on the left are for the case when there is no step ($h = 0$) going from the part B to part A. In this case, as the liquid evaporates, it also dewets from the surface, breaking the bridge. The results on the right correspond to when there is a step of height $h = 2\sigma$. This step prevents the dewetting, so that as the liquid evaporates, the nanoparticles gather to form a bridge. The times t are given in terms of average number of MC steps per lattice site.
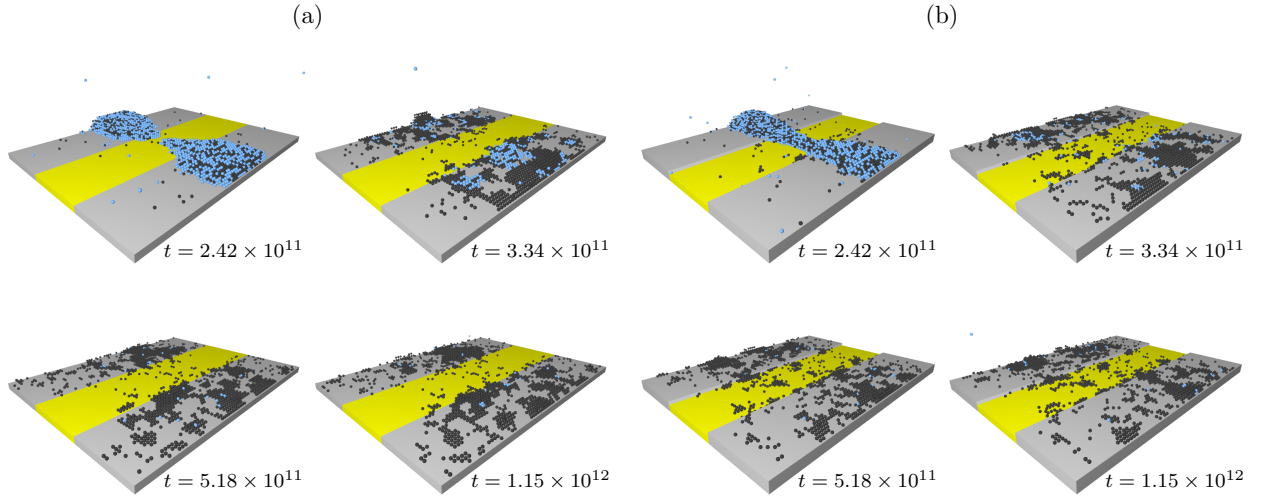
Figure 6.11: Snapshots from a simulation of a liquid bridge drying from the smooth surface
with $\varepsilon_{nl}/\varepsilon_{ll} = 1.25$, $\varepsilon_{nn}/\varepsilon_{ll} = 1.5$, $k_B T/\varepsilon_{ll} = 0.6$, $\phi = 0.1$, $\mu/\varepsilon_{ll} = -6$. The attraction
strength with the hydrophobic yellow part A surface is $\varepsilon_{wl}^A/\varepsilon_{ll} = \varepsilon_{wn}^A/\varepsilon_{ll} = 0.4$, while the
interaction with the grey part B strips either side has strength $\varepsilon_{wl}^B/\varepsilon_{ll} = \varepsilon_{wn}^B/\varepsilon_{ll} = 0.8$. In
the four snapshots on the left in (a) there is no difference in height between the two surfaces
($h = 0$). In the four on the right (b) the hydrophilic part B (in grey) is raised a distance
$h = \sigma$ above part A.

surface, compared to the case in Fig. 6.10. With no step present ($h = 0$), the bridge of liquid
breaks at the time $t \approx 2.4 \times 10^{11}$ MC steps and the nanoparticles temporally group together
with the remaining liquid, but eventually spread out over the hydrophilic region. With a
step of height $h = \sigma$, the bridge still breaks at $t \approx 2.4 \times 10^{11}$ MC steps. More nanoparticles
remain at the corner formed from the step but the end result is similar to the case with
no step. Although not shown here, when $h = 2\sigma$, the connection breaks at $t \approx 2.1 \times 10^{11}$
MC steps but the break occurs in the hydrophilic region and the nanoparticles collect in
the hydrophobic region, scattering randomly as the rest of the liquid evaporates, due to the
smoothness of the surface.

Fig. 6.12 shows results from a simulation where the parameters are the same as in
Fig. 6.11, except here we assume the surface is rough, i.e. we implement the no-slip dy-
namical rule. When there is no step ($h = 0$), the bridge breaks at $t \approx 4.4 \times 10^{11}$ MC steps.
When the step height $h = \sigma$, the bridge connection almost holds, but eventually breaks

(a) (b)
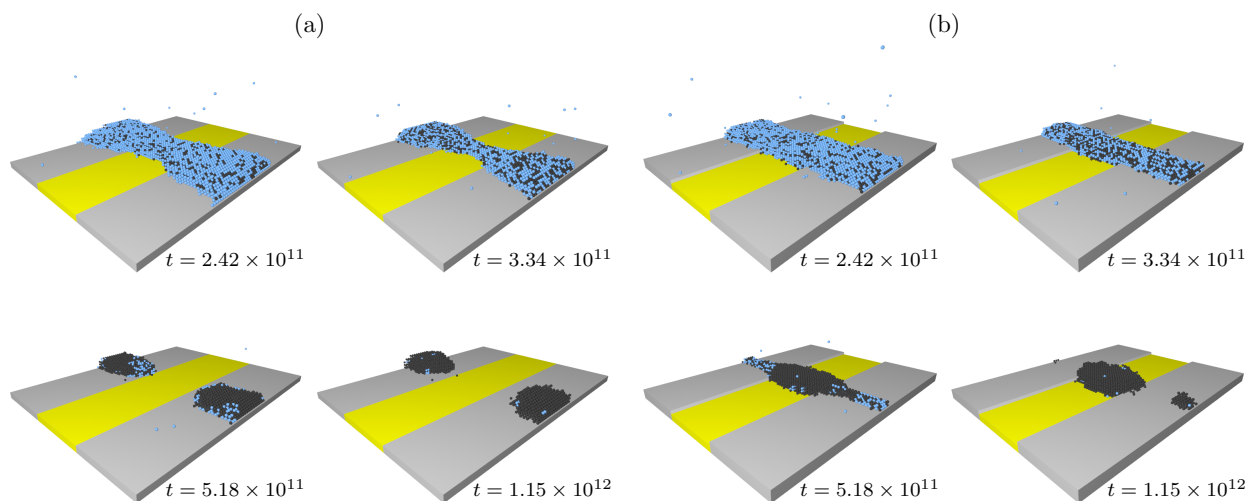
Figure 6.12: Time series from a bridge of liquid drying from a rough surface (modelled using the no-slip dynamical rule), with the same parameter values as given in caption of Fig. 6.11. The four on the left (a), are snapshots for the case when there is no step ($h = 0$) in the height of the surface. In this case, as the liquid evaporates, it also dewets from the surface, breaking the bridge. The four on the right (b) correspond to a step of height $h = \sigma$ between the hydrophobic and hydrophilic parts of the surface. The times t are given in terms of average number of MC steps per lattice site, taken at the same times as in the previous figure.

at $t \approx 5.2 \times 10^{11}$ MC steps. Interestingly, however, due to the attractive step from the hydrophobic to the hydrophilic region, most of the nanoparticles are stabilised in a cluster on the hydrophobic region.

Evaporating film over an hydrophobic strip

Figs. 6.13 and 6.14 illustrate the situation when a film of nanoparticle suspension that initially has uniform thickness evaporatively dewets from the same surface considered already, i.e. with both hydrophobic and hydrophilic parts. All the parameters for the simulations in Figs. 6.13 and 6.14 are the same as in Fig. 6.11 except for the temperature which is increased from $k_B T / \varepsilon_{ll} = 0.6$ to $k_B T / \varepsilon_{ll} = 0.76$, which slightly speeds up the simulations.

Fig. 6.13 for the smooth surface shows there are differences between $h = 0$ and $h = \sigma$. As the liquid evaporates, in both cases holes appear in the film during the drying, at around $t \approx 2.0 \times 10^{11}$ MC steps. We are not able to determine conclusively whether these holes are

nucleated or are formed via spinodal dewetting, which is expected to occur when the film thickness decrease below a critical value [27, 28, 49]. In the $h = 0$ case, the holes appear first in the hydrophobic region. This leads to a dewetting of the liquid from off the hydrophobic region, moving many of the nanoparticles onto the hydrophilic region. In contrast, for the $h = \sigma$ case, since the film is thicker over the hydrophobic region, the holes instead appear first over the hydrophilic region. Thus, in the $h = \sigma$ case, initially the dewetting from the hydrophilic part of the surface leads to a clear increase in the density of the nanoparticles on the hydrophobic region. However, they then subsequently move back onto the hydrophilic part of the surface as the evaporation continues. In both cases, after most of the liquid has evaporated, the nanoparticles are distributed inhomogeneously over the surface, having a greater density on the hydrophilic part of the surface. However, for the $h = \sigma$ case, because the nanoparticles congregate at the corner of the steps, there is therefore slightly more bare patches on the hydrophilic part of the surface, compared to the $h = 0$ case.

Fig. 6.14 shows snapshots from two simulations with the no-slip dynamical rule, which prevents horizontal movement of particles that are in contact with the surface. Holes in the film appear in a manner similar to that observed in the early stages of the dynamics when the surface is smooth (Fig. 6.13). However, once the holes are formed, the dynamics is changed significantly. The surface roughness results in the nanoparticles becoming congregated in clumps and they spread far less than in the case with the smooth surface. For the $h = 0$ case in Fig. 6.14(a), the final state consists of the nanoparticles being clustered into two mounds with fewer lone nanoparticles than observed on the smooth surface. Surprisingly, one of the nanoparticle clusters spans the hydrophobic region of the surface. We believe this stems from the interplay of the no-slip dynamics and the fact that the attraction of the nanoparticles to each other is stronger than their attraction to the surface.

In the case with a step of height $h = \sigma$ displayed in Fig. 6.14(b), the dewetting initiates in the thinner film on the hydrophilic part of the surface, similar to the smooth surface case in Fig. 6.13(b). This leads to the nanoparticles becoming deposited on the hydrophobic

region, similar to in the smooth surface case, except that fewer nanoparticles remain on the hydrophilic region. However, in contrast to the smooth surface case, ultimately the relative lack of mobility leads to the nanoparticles remaining on the hydrophobic region, forming a large cluster that is stabilised at the edges by the step.

6.6 Conclusion

In this paper we have presented a MC model of the drying of a nanoparticle suspension on heterogeneous surfaces. This mixture of liquid and nanoparticles is a simple model for the ink that is used in the ink jet printing manufacturing process described in [25]. The model contains parameters which can be determined from experiments. Measuring the equilibrium contact angle of drops of the liquid on the relevant surfaces, in conjunction with the present work, allows the determination of the required values of the liquid-liquid and liquid-wall attraction parameters. Similarly, knowledge of the diffusion coefficient allows to relate the MC time step to the experimental time scales. The model can include the effects of surface roughness via a simple no-slip dynamical rule that forbids the motion of all particles that are in contact with the surface.

A key finding of the present work is the observation that when printing a bridge over a hydrophobic region to connect hydrophilic strips either side, adhesion is improved when the hydrophobic strip is at a lower level than the surrounding hydrophilic regions. We find that when the bridge does not properly form, generally the break occurs over the hydrophobic strip. However, for some parameter values occasionally the counter-intuitive result occurs, whereby the film breaks, but with nanoparticles congregating in the hydrophobic strip. This effect generally occurs when considering the evaporation of a film of liquid, rather than a bridge. That said, evaporating films can still result in clumps of nanoparticles distributed over the two regions.

The results have shown the necessity to choose ink and surface parameters carefully

to obtain the best connections when ink jet printing. For example, it may be possible to enhance particle bridge formation by adjusting the surface chemistry of the nanoparticles to make them favour the hydrophobic portion of the surface. This aspect has not been explored here. However, such enhancement might also instead lead to results such as that in Fig. 6.12, where the bulk of the nanoparticles are deposited on the hydrophobic part of the surface and the bridge is broken. Further work will directly relate the parameters in the model Hamiltonian to the properties of the specialist materials used in the printing process. Our work here shows that to fully understand the observed phenomena requires knowledge of both the fluid dynamics and the thermodynamics.

Acknowledgements

(a)   (b)
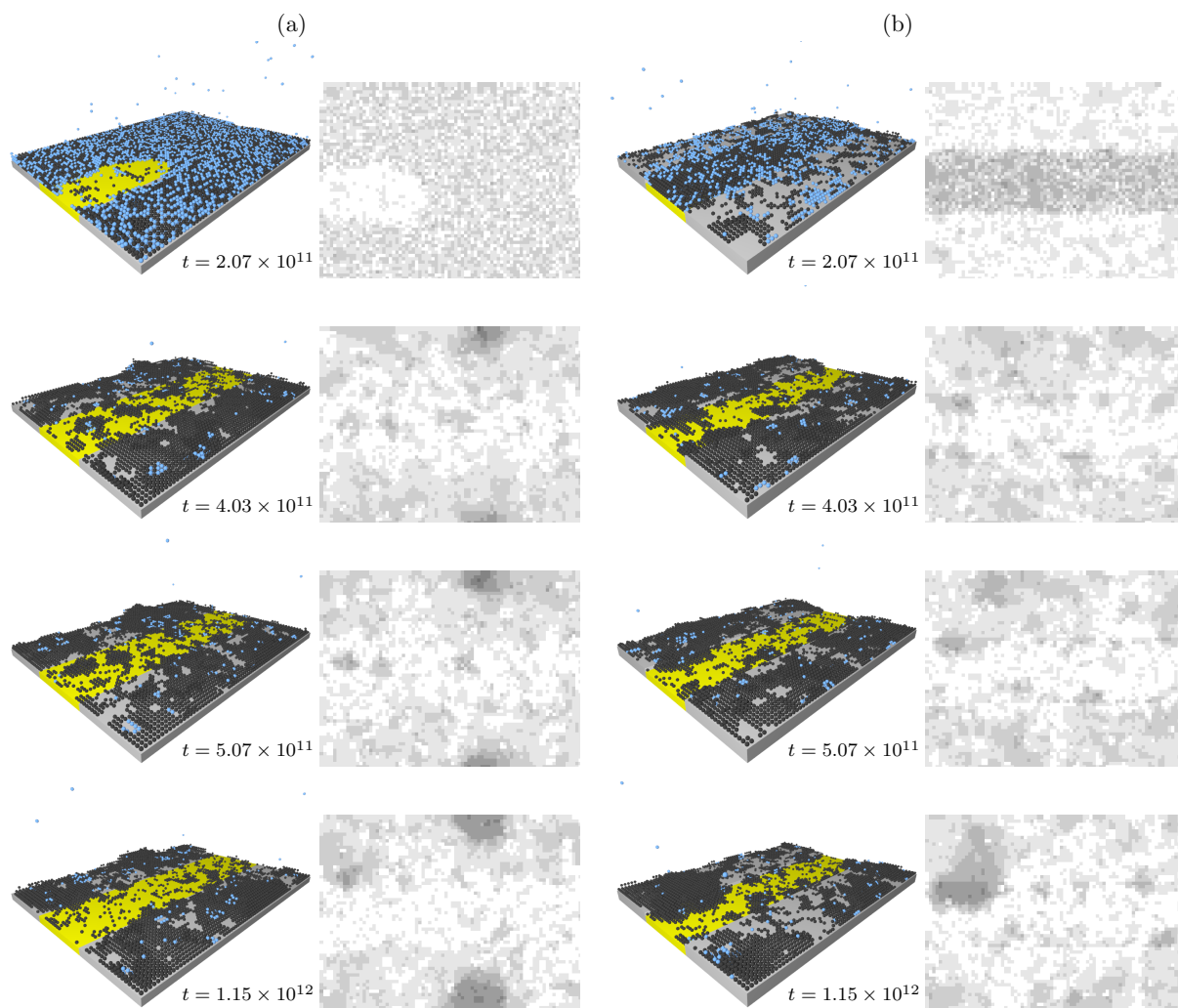
Figure 6.13: Snapshots of a uniform film of nanoparticle suspension drying from a smooth surface. On the right of each is a grey-scale density profile of the nanoparticles viewed from above. The parameter values are the same as in Fig. 6.11 except $k_B T/\varepsilon_{ll} = 0.76$. The results on the left in (a) are for $h = 0$ and those on the right in (b) are with $h = \sigma$.

(a)   (b)
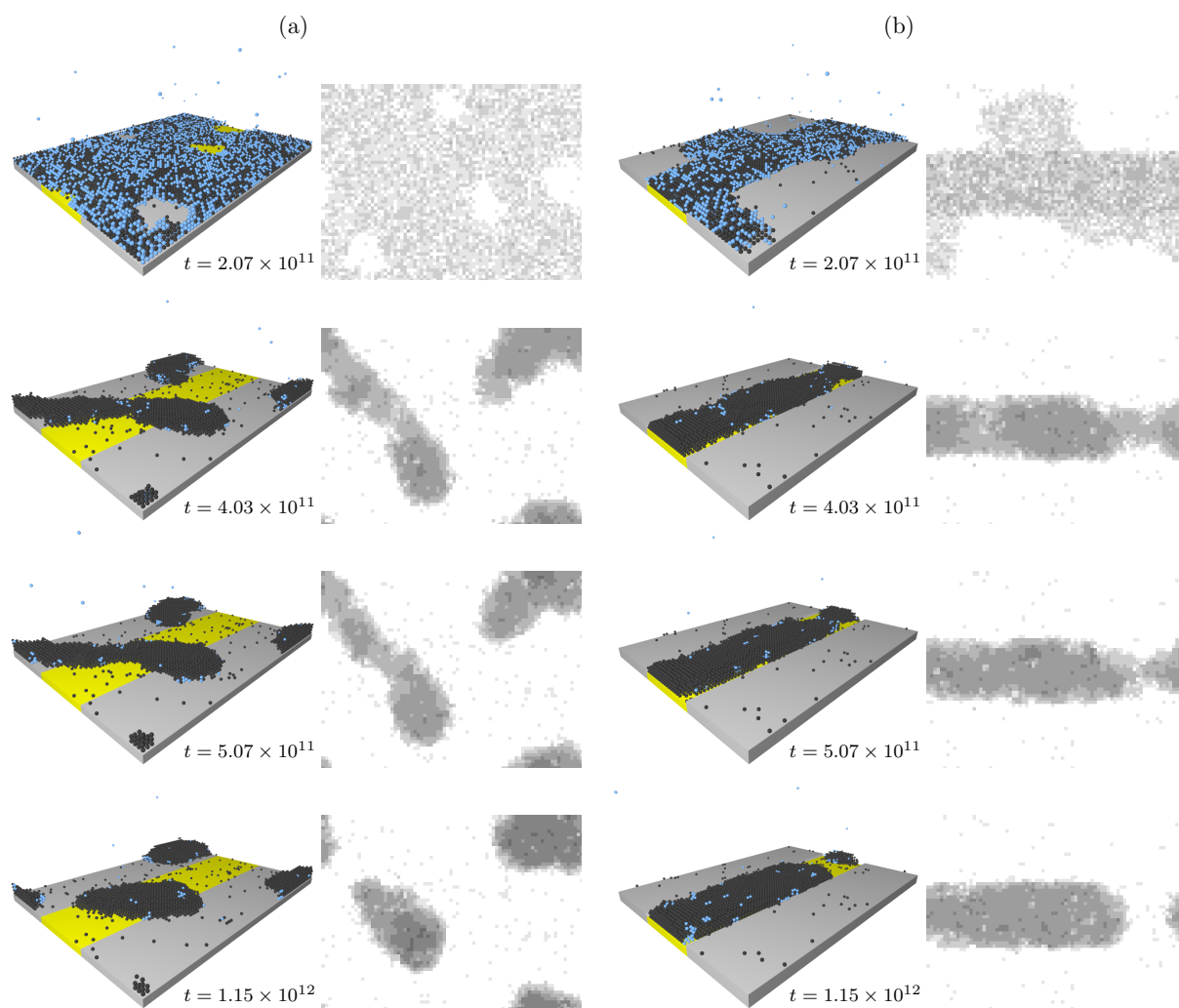
Figure 6.14: Snapshots of a uniform film of nanoparticle suspension drying from a rough surface, modelled via the no-slip dynamic rule. On the right of each is a grey-scale density profile of the nanoparticles viewed from above. The parameter values are the same as in Fig. 6.13. The results on the left in (a) are for $h = 0$ and those on the right in (b) are with $h = \sigma$.

Chapter 7

Dynamical density functional theory for the evaporation of droplets of nanoparticle suspension

We develop a lattice gas model for the drying of droplets of a nanoparticle suspension on a planar surface, using dynamical density functional theory (DDFT) to describe the time evolution of the solvent and nanoparticle density profiles. The DDFT assumes a diffusive dynamics but does not include the advective hydrodynamics of the solvent, so the model is relevant to highly viscous or near to equilibrium systems. Nonetheless, we see an equivalent of the coffee-ring stain effect, but in the present model it occurs for thermodynamic rather the fluid-mechanical reasons. The model incorporates the effect of phase separation and vertical density variations within the droplet and the consequence of these on the nanoparticle deposition pattern on the surface. We show how to include the effect of slip or no-slip at the surface and how this is related to the receding contact angle. We also determine how the equilibrium contact angle depends on the microscopic interaction parameters.

7.1   Introduction

The structures formed on surfaces from the drying of liquid films or droplets containing
suspended colloids or nanoparticles can vary significantly, depending on the nature of the
suspended particles, the solvent, the surrounding airflow, the vapour pressure and the na-
ture of the surface [66, 67, 68, 69]. Whether the surface is rough or smooth, solvophobic
or solvophilic, patterned, curved or in any other way heterogeneous, makes a crucial differ-
ence. Understanding the drying dynamics and pattern formation in such systems is not only
fascinating fundamental science, but there are many practical application that rely on the
behaviour of such fluids at interfaces, ranging from lubrication to the use of ink-jet printing
in advanced manufacturing – see e.g. the recent example in [25].

Perhaps the most typical example of this is the coffee ring stain formed when a spilt
droplet of coffee (or indeed many other liquids containing solutes or suspended particles)
dries on a surface [67, 68, 69, 70, 71]. As the water in the droplet evaporates, the majority
of the coffee is deposited around the edge, in the vicinity of the droplet contact line. This is
despite more of the coffee having been initially in the centre, since it is uniformly dispersed
within the liquid and the centre is where the liquid thickness above the surface is greatest.
The coffee stain is formed because the evaporation of the liquid leads to a hydrodynamic flow
of liquid from the centre of the droplet towards the edge. This flow carries the suspended
particles to the edge of the droplet, where they remain when all the liquid is finally evaporated
[68, 69, 70, 71]. Note however that ring deposition does not alway occur. For example, it can
be suppressed if the particles are elongated instead of roughly spherical [72]. But in general
the effect must be overcome in applications requiring uniform surface deposition, such as in
printing and coating.

Modelling such intricacies present a challenge, because they depend on a fine balance
and interplay of thermodynamic effects related to evaporation and perhaps also phase tran-
sitions within the droplet and hydrodynamic effects related to fluid flow within the droplet
and overall droplet dynamics. These considerations are especially important if there are

advancing or receding contact lines [73]. Thin film hydrodynamic models have been used to to describe many key aspects [26, 27, 28, 29, 30, 31], but such models are unable to describe vertical variations in the local particle concentration and do not fully capture any of the microscopic structure within the liquid. Fully microscopic models based on molecular dynamics (MD) computer simulations, such as those described in Refs. [32, 33, 34, 35], do of course describe every aspect of the structure and dynamics in the droplet. However, these approaches are limited in the size of droplet that can be modelled. The same is to some extent also true when classical density functional theory (DFT) [20, 2, 3] and dynamical DFT (DDFT) [7, 8, 9, 10, 11] are applied to describe the structure and dynamics of droplets – see e.g. Refs. [59, 37, 74, 38, 39] and references therein. That said, because DFT and DDFT are statistical mechanical theories, the scaling of the computational cost with size of the system is better than the scaling with MD [75]. Here we develop a DDFT for droplets containing suspended nanoparticles that is based on a lattice Hamiltonian (generalised Ising) model of the microscopic interactions in the system. The advantage of assuming the nanoparticle suspension can be modelled as a lattice fluid is that it allows us to describe much larger droplets than is feasible using a fully microscopic DFT – see e.g. [39].

Lattice models have been successfully used previously to describe the evolution of liquids and particle suspensions on surfaces. These models were initially 2-dimensional (2D) Monte Carlo (MC) models [66, 40, 41, 42, 43, 76] that assumed there is no vertical variation in the liquid in the direction perpendicular to the solid surface on which the liquid is deposited. However, 3-dimensional (3D) MC models have subsequently also been developed [44, 45, 46, 47, 48, 77]. The present DDFT assumes the same Hamiltonian as the MC model in [77]. Thus, the DDFT presented here is able to fully describe any vertical variations in the local densities within the droplet, such as the formation of a nanoparticle 'crust' on the drying droplet, unlike the 2D DDFT models developed previously [78, 49].

An important aspect of the MC model in [77] is the identification of how the interactions between lattice sites should vary with distance in order to have liquid droplets with a realistic

hemispherical shape, so as to lessen the influence of the underlying grid. Owing to the fact that we base our DDFT on the same Hamiltonian, the present model also has this advantage. An additional feature of the DDFT developed here is that it incorporates the effects of slip, no-slip or partial slip of the liquid at the surface. We show how this affects the evolution of the shape of droplets as they evaporate and how this is connected to the receding contact angle. Since the DDFT incorporates all the thermodynamics related to the degree of solubility of the nanoparticles in the solvent liquid, the model incorporates the effects of phase separation (aggregation) of the nanoparticles as the local nanoparticle concentration increases due to the solvent evaporation. We show that this can lead to a coffee-ring like stain. However, in the present model it is due to the thermodynamics of phase separation, not the usual advective fluid mechanical mechanism [68, 69, 70, 71]. The DDFT we use is one that assumes only diffusive particle motion – i.e. we assume the droplet is not too far from equilibrium. This is the original DDFT of Refs. [7, 8, 9] for both the solvent and the suspended particles, rather than more sophisticated DDFTs that include inertial effects [10, 11] or effects of hydrodynamics [79, 75, 80]. We also show that the thermodynamics of phase separation can lead to the deposition of multiple rings.

This paper is structured as follows: In Section 7.2 we introduce the lattice Hamiltonian for the system and the approximation we use for the free energy of the system that is the input to the DDFT. In Section 7.3 we describe the bulk-mixture phase behaviour and present phase diagrams showing how the vapour-liquid phase separation depends on the model interaction parameters and changes as the concentration of the nanoparticles is varied. In Section 7.4 we calculate equilibrium interfacial properties, including calculating the density profiles of the solvent and the nanoparticles at the vapour-liquid interface, the surface tension and how it depends on temperature and also the equilibrium contact angle. We also compare with the MC results from Ref. [77] to illustrate the accuracy of the DFT. In Section 7.5 we describe the DDFT used to describe the non-equilibrium dynamics of the solvent and the nanoparticles, including how to include the effects of (no)slip at the substrate. In

Section 7.6 we display the results from simulating evaporating droplets of both pure solvent and also containing nanoparticles. We show how the receding contact angle depends on the parameters controlling the slip at the surface and present results for the deposits left by evaporating droplets including a coffee-ring like deposit, a deposit equivalent to multiple rings and also patterns related to spinodal dewetting. Finally, in Section 7.7 we make a few concluding remarks.

7.2   Lattice model for the system

We model the nanoparticle suspension by discretising onto a 3D cubic lattice with lattice spacing σ (which is also the diameter of the particles), with each site on the lattice labelled by the index $\mathbf{i}$, where $\mathbf{i} = (i, j, k) \in \mathbb{Z}^3$. Thus, $\mathbf{i}$ defines the location of the lattice site. Henceforth, we set $\sigma = 1$, defining our unit of length. The energy of the system (Hamiltonian) is given by

$$E = -\sum_{\mathbf{i},\mathbf{j}} \left(\frac{1}{2}\varepsilon_{\mathbf{ij}}^{ll} n_{\mathbf{i}}^l n_{\mathbf{j}}^l + \varepsilon_{\mathbf{ij}}^{nl} n_{\mathbf{i}}^l n_{\mathbf{j}}^n + \frac{1}{2}\varepsilon_{\mathbf{ij}}^{nn} n_{\mathbf{i}}^n n_{\mathbf{j}}^n \right)$$
$$- \mu \sum_{\mathbf{i}} n_{\mathbf{i}}^l + \sum_{\mathbf{i}} \Phi_{\mathbf{i}}^l n_{\mathbf{i}}^l + \sum_{\mathbf{i}} \Phi_{\mathbf{i}}^n n_{\mathbf{i}}^n,$$

(7.2.1)

where $n_{\mathbf{i}}^l$ is the occupation number for the liquid at site $\mathbf{i}$ and $n_{\mathbf{i}}^n$ is the occupation number for nanoparticles at site $\mathbf{i}$, i.e., $n_{\mathbf{i}}^l = 1$ if the site is occupied by liquid and $n_{\mathbf{i}}^l = 0$ if unoccupied by liquid. Similarly, $n_{\mathbf{i}}^n = 0$ or 1 depending on whether or not the site $\mathbf{i}$ is occupied by a nanoparticle. A lattice site can not be occupied by both liquid and a nanoparticle. $\Phi_{\mathbf{i}}^l$ is the external potential due to the surface influencing the liquid at site $\mathbf{i}$ and $\Phi_{\mathbf{i}}^n$ is the external potential for the nanoparticles. The interaction between pairs of liquid particles at sites $\mathbf{i}$ and $\mathbf{j}$ is determined by the matrix $\varepsilon_{\mathbf{ij}}^{ll} = \varepsilon_{ll} c_{\mathbf{ij}}$, which is a discretised pair potential. The parameter ε_{ll} governs the overall strength. Similarly, $\varepsilon_{\mathbf{ij}}^{ln} = \varepsilon_{ln} c_{\mathbf{ij}}$ is the interaction matrix between nanoparticles and liquid, with strength determined by the parameter ε_{ln}, and $\varepsilon_{\mathbf{ij}}^{nn} = \varepsilon_{nn} c_{\mathbf{ij}}$ is the interaction between pairs of nanoparticles, with ε_{nn} determining the

overall strength. $c_{\mathbf{ij}}$ is a dimensionless coefficient which decreases in value as the distance between the pairs of particles increases. We use the following values

$$
c_{\mathbf{ij}} = \begin{cases}
1 & \mathbf{j} \in \{\text{NN } \mathbf{i}\} \\
\dfrac{3}{10} & \mathbf{j} \in \{\text{NNN } \mathbf{i}\} \\
\dfrac{1}{20} & \mathbf{j} \in \{\text{NNNN } \mathbf{i}\} \\
0 & \text{otherwise}
\end{cases}
\tag{7.2.2}
$$

where NN $\mathbf{i}$, NNN $\mathbf{i}$ and NNNN $\mathbf{i}$ stand for nearest neighbours, next nearest neighbours and next-next nearest neighbours, respectively, to lattice site $\mathbf{i}$. The choice of particular values in Eq. (7.2.2) is important, as this leads to liquid droplets on the surface having a hemispherical shape [77]. For example, if instead we just have nearest neighbour interactions, then the system forms unrealistic shaped droplets with facetted surfaces, particularly at low temperatures.

If the nanoparticle suspension is in contact with a planar solid surface, this exerts external potentials that we assume are

$$
\Phi_{\mathbf{i}}^{l} = \begin{cases}
-\frac{12}{5}\varepsilon_{wl} & j = 0, \\
0 & \text{otherwise,}
\end{cases}
\tag{7.2.3}
$$

and

$$
\Phi_{\mathbf{i}}^{n} = \begin{cases}
-\frac{12}{5}\varepsilon_{wn} & j = 0, \\
0 & \text{otherwise,}
\end{cases}
\tag{7.2.4}
$$

where ε_{wl} is the attraction between the surface and the liquid and ε_{wn} is the attraction between the surface and the nanoparticles, and j is the component of $\mathbf{i}$ that varies in the direction perpendicular to the surface. The factor 12/5 in Eq. (7.2.3) comes from assuming a pair potential $\varepsilon_{\mathbf{ij}}^{wl} = \varepsilon_{wl}c_{\mathbf{ij}}$ between wall lattice sites and the liquid. When a liquid particle is next to the wall, summing over the interaction with the neighbouring wall particles leads

to Eq. (7.2.3). Similarly, summing over $\varepsilon_{\mathbf{ij}}^{wn} = \varepsilon_{wn} c_{\mathbf{ij}}$ leads to Eq. (7.2.4).

For the lattice model defined above, one can study both the equilibrium and non-equilibrium behaviour using the Monte-Carlo simulation approach developed in [77]. Here, a statistical mechanical theory based on DFT [20, 2, 3] and DDFT [7, 8, 9] is derived. Thus, we develop a theory for the average densities,

$$\rho_{\mathbf{i}}^l = \langle n_{\mathbf{i}}^l \rangle \quad \text{and} \quad \rho_{\mathbf{i}}^n = \langle n_{\mathbf{i}}^n \rangle, \tag{7.2.5}$$

which are the ensemble average densities at site $\mathbf{i}$, i.e., $\langle \ldots \rangle$ denotes a statistical average. Making a mean field approximation, the Helmholtz free energy for the binary lattice-gas is [59, 81, 82, 83, 38]

$$F(\{\rho_{\mathbf{i}}^l\}, \{\rho_{\mathbf{i}}^n\}) = k_B T \sum_{\mathbf{i}} \left[\rho_{\mathbf{i}}^l \ln \rho_{\mathbf{i}}^l + (1 - \rho_{\mathbf{i}}^l - \rho_{\mathbf{i}}^n) \ln(1 - \rho_{\mathbf{i}}^l - \rho_{\mathbf{i}}^n) + \rho_{\mathbf{i}}^n \ln \rho_{\mathbf{i}}^n \right]$$

$$- \frac{1}{2} \sum_{\mathbf{i},\mathbf{j}} \varepsilon_{\mathbf{ij}}^{ll} \rho_{\mathbf{i}}^l \rho_{\mathbf{j}}^l - \sum_{\mathbf{i},\mathbf{j}} \varepsilon_{\mathbf{ij}}^{ln} \rho_{\mathbf{i}}^l \rho_{\mathbf{j}}^n - \frac{1}{2} \sum_{\mathbf{i},\mathbf{j}} \varepsilon_{\mathbf{ij}}^{nn} \rho_{\mathbf{i}}^n \rho_{\mathbf{j}}^n$$

$$+ \sum_{\mathbf{i}} \left(\Phi_{\mathbf{i}}^l \rho_{\mathbf{i}}^l + \Phi_{\mathbf{i}}^n \rho_{\mathbf{i}}^n \right), \tag{7.2.6}$$

where k_B is Boltzmann's constant and T is the temperature. The above is a discretised DFT for a binary mixture.

7.3 Bulk solvent phase behaviour

The densities can be constants when $\Phi_{\mathbf{i}}^l = \Phi_{\mathbf{i}}^n = 0$, i.e., we have a uniform fluid with $\rho_{\mathbf{i}}^l = \rho_l$ and $\rho_{\mathbf{i}}^n = \rho_n$, for all $\mathbf{i}$. In this case, the sum over neighbours in the interaction terms in the Helmholtz free energy (7.2.6) can be evaluated. The integrated interaction matrix is $\sum_{\mathbf{j}} c_{\mathbf{ij}} = 10$ for all $\mathbf{i}$, so we have $a_{ll} = 10\varepsilon_{ll}$, $a_{ln} = 10\varepsilon_{nl}$ and $a_{nn} = 10\varepsilon_{nn}$ as the integrated strengths of the pair interactions. From Eq. (7.2.6) the average Helmholtz free energy per

lattice site, $f = F/V$, where V is the volume of the system, is given by

$$f = k_B T \left(\rho_l \ln \rho_l + (1 - \rho_l - \rho_n) \ln(1 - \rho_l - \rho_n) + \rho_n \ln \rho_n \right)$$
$$- \frac{1}{2} a_{ll} \rho_l^2 - a_{ln} \rho_l \rho_n - \frac{1}{2} a_{nn} \rho_n^2. \tag{7.3.1}$$

From this we can calculate the spinodal, the locus where $\partial^2 f / \partial \rho^2 = 0$ and where $\rho = \rho_l + \rho_n$ is the total density. The spinodal defines the boundary of the region of the phase diagram where the system is unstable and density fluctuations in a uniform system spontaneously grow, leading to phase separation. For temperatures where two-phase coexistence can occur, the binodal curve gives the coexisting density values for a system in equilibrium. This is calculated by equating the chemical potential, temperature and pressure in each of the coexisting phases. States in the phase diagram outside the binodal are stable and no phase separation occurs.

We can use Eq. (7.3.1) to calculate the binodal since thermodynamic quantities such as the chemical potentials, μ_l and μ_n, and pressure, P, may be obtained using the following relations

$$\mu_l = \frac{\partial f}{\partial \rho_l}, \quad \mu_n = \frac{\partial f}{\partial \rho_n}, \quad P = -\frac{\partial f}{\partial V}. \tag{7.3.2}$$

These give

$$\mu_l = k_B T (\ln \rho_l - \ln(1 - \rho_l - \rho_n)) - a_{ll} \rho_l - a_{ln} \rho_n, \tag{7.3.3}$$

$$\mu_n = k_B T (\ln \rho_n - \ln(1 - \rho_l - \rho_n)) - a_{ln} \rho_l - a_{nn} \rho_n, \tag{7.3.4}$$

$$P = -k_B T \ln(1 - \rho_l - \rho_n) - \frac{1}{2} a_{ll} \rho_l^2 - a_{ln} \rho_l \rho_n - \frac{1}{2} a_{nn} \rho_n^2, \tag{7.3.5}$$

where we have used the fact that in a uniform system the densities $\rho_l = N_l/V$ and $\rho_n = N_n/V$, where N_l and N_n are the total numbers of each species in the system.

For the pure liquid with no nanoparticles present ($\rho_n = 0$), we can use the symmetry of the Hamiltonian (7.2.1) to simplify the calculation of the binodal [49]. This allows us to
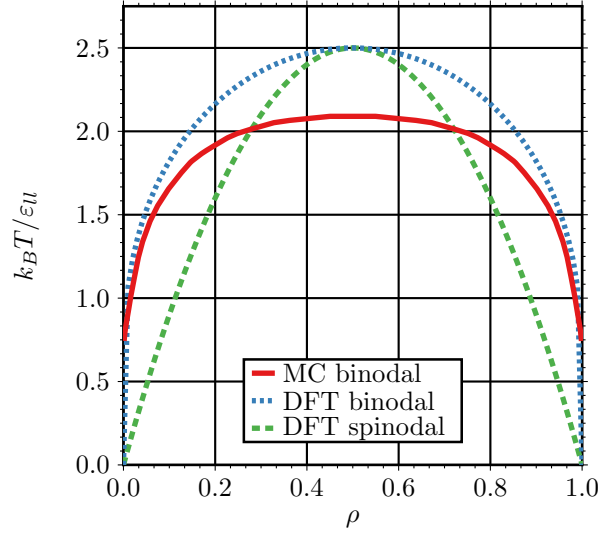
Figure 7.1: Binodal curve for the lattice fluid using both DFT and MC computer simulations in the temperature versus density plane. We also display the spinodal from DFT. The MC results are from Ref. [77].

observe that if ρ_l is the density of the liquid at coexistence then $(1 - \rho_l)$ is the density of the coexisting vapour. On equating the pressure in the two phases we obtain the following equation for the binodal:

$$\frac{k_B T}{\varepsilon_{ll}} = \frac{5(2\rho_l - 1)}{\ln[\rho_l/(1 - \rho_l)]}. \tag{7.3.6}$$

This has a maximum at $\rho_l = 0.5$ which corresponds to a critical temperature of $k_B T/\varepsilon_{ll} = 2.5$. Fig. 7.1 shows a plot of this binodal curve together with the binodal from Ref. [77] that was calculated using MC simulations for the same system, with Hamiltonian given by Eqs. (7.2.1) and (7.2.2). The binodals are qualitatively similar, but at higher temperatures there is a sizeable difference between the two curves since the DFT in Eq. (7.2.6) is a mean field theory. The critical temperature predicted by the DFT is around $0.4 k_B/\varepsilon_{ll}$ higher than the true value. However, for temperatures $k_B T/\varepsilon_{ll} < 1.5$ we see that the coexisting density values from the DFT are in fairly good agreement with those from the MC. This is the regime in which the results below are obtained.

Returning to consider the full binary mixture, to calculate the binodals we have the additional condition that the chemical potential of the nanoparticles, μ_n, is the same in both phases. The phase diagram is no longer symmetric around $\rho_l = 0.5$ when the nanoparticles are present. Thus, we must solve the following simultaneous equations:

$$T^{\mathrm{LDP}} = T^{\mathrm{HDP}}, \tag{7.3.7}$$

$$P^{\mathrm{LDP}} = P^{\mathrm{HDP}}, \tag{7.3.8}$$

$$\mu_l^{\mathrm{LDP}} = \mu_l^{\mathrm{HDP}}, \tag{7.3.9}$$

$$\mu_n^{\mathrm{LDP}} = \mu_n^{\mathrm{HDP}}, \tag{7.3.10}$$

where LDP stands for low density phase, HDP stands for high density phase. The first equation can be trivially satisfied by simply setting the same temperature in both phases. We then also fix the chemical potential of the nanoparticles to some specified value. This then gives us four equations for the four unknowns, namely the densities of the two species in the two different phases [49]. Solving like this for a range of temperatures gives us the phase diagram.

Figs. 7.2 and 7.3 show the binodals for the liquid-nanoparticle mixture for the case when $\varepsilon_{nl}/\varepsilon_{ll} = 1.25$ and $\varepsilon_{nn}/\varepsilon_{ll} = 1.5$ and for different values of the nanoparticle chemical potential μ_n. We see that as μ_n is increased the density of the nanoparticles increases in both phases and can in fact become the majority species for large enough μ_n. Note that Fig. 7.1 can be considered to be the $\mu_n = -\infty$ case in this sequence with varying μ_n, where, of course, $\rho_n = 0$ in both coexisting phases.

In Fig. 7.4 we show results for a case where ε_{nl} is less than both ε_{nn} and ε_{ll}, in contrast to the case in Figs. 7.1–7.3, where $\varepsilon_{nl} = \frac{1}{2}(\varepsilon_{nn} + \varepsilon_{ll})$. In this case it is energetically unfavourable for the nanoparticles to mix with the liquid and so for the case in Fig. 7.4 where $\mu_n/\varepsilon_{ll} = -8$ (a low value), the density of the nanoparticles in both coexisting phases is low. For higher values of μ_n (not displayed) we observe liquid-liquid phase separation similar to that
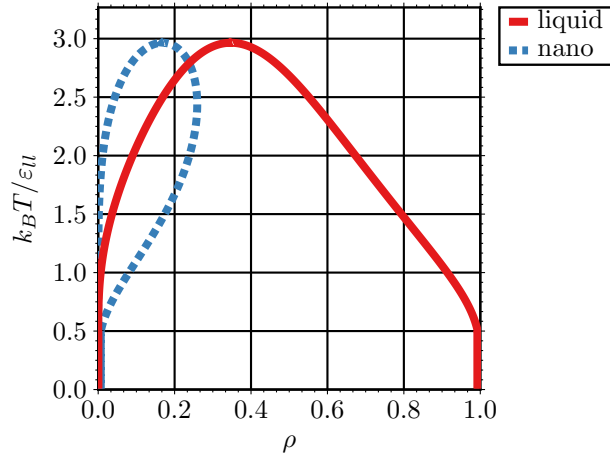
Figure 7.2: Binodal curves for the binary mixture with $\mu_n/\varepsilon_{ll} = -10$, $\varepsilon_{nl}/\varepsilon_{ll} = 1.25$, $\varepsilon_{nn}/\varepsilon_{ll} = 1.5$.

described in Ref. [84].

7.4   Equilibrium interfacial behaviour

Having determined the bulk fluid phase behaviour, we now briefly consider the interface
between the coexisting phases and calculate the surface tension.

7.4.1   Density profiles at the free interface

At the planar interface between the vapour and the liquid phases the density profiles vary
only in the direction perpendicular to the interface. We assume that the index varying in
the direction perpendicular to the interface is j. Recall $\mathbf{i} = (i, j, k)$. The density profiles are
calculated by minimising the grand potential

$$\Omega = F - \mu_l \sum_{\mathbf{i}} \rho_{\mathbf{i}}^l - \mu_n \sum_{\mathbf{i}} \rho_{\mathbf{i}}^n \tag{7.4.1}$$
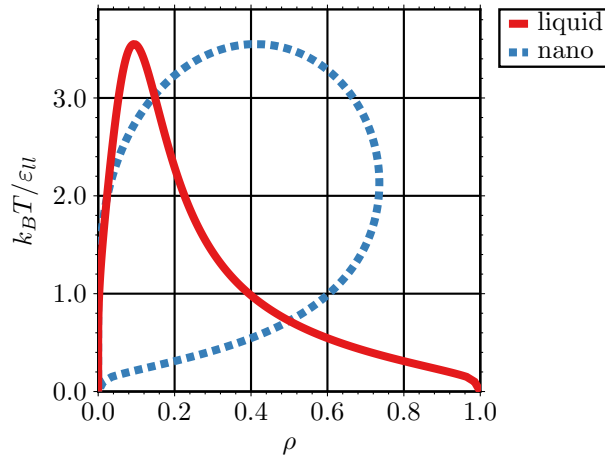
Figure 7.3: Binodal curves for the binary mixture with $\mu_n/\varepsilon_{ll} = -8$, $\varepsilon_{nl}/\varepsilon_{ll} = 1.25$ and $\varepsilon_{nn}/\varepsilon_{ll} = 1.5$.
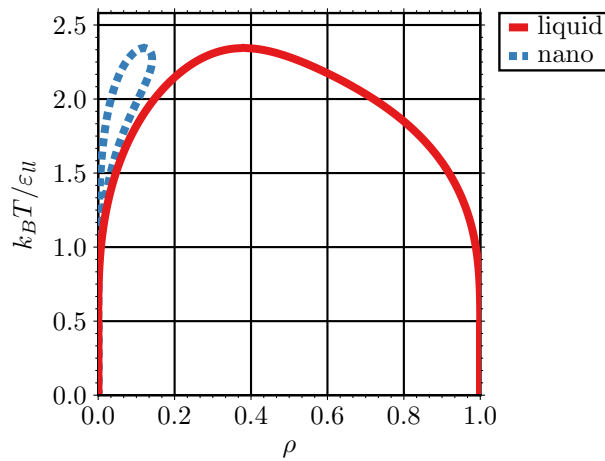
Figure 7.4: Binodal curves for the binary mixture with $\mu_n/\varepsilon_{ll} = -8$, $\varepsilon_{nl}/\varepsilon_{ll} = 0.75$ and $\varepsilon_{nn}/\varepsilon_{ll} = 1.5$.
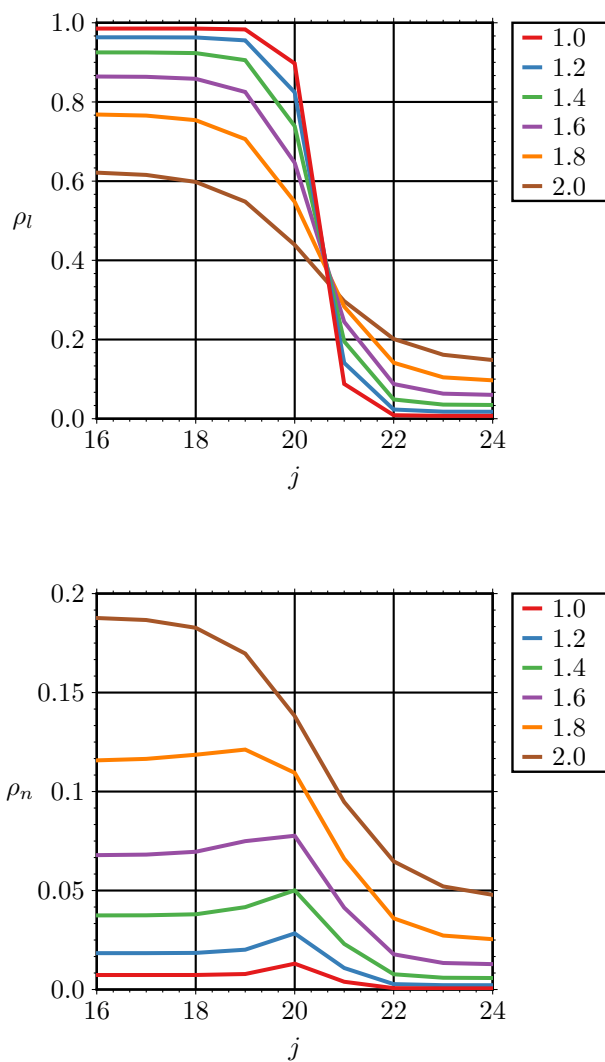
Figure 7.5: Liquid density profiles (top) and nanoparticle density profiles (bottom) at the free liquid-vapour interface for $\varepsilon_{nl}/\varepsilon_{ll} = 0.75$, $\varepsilon_{nn}/\varepsilon_{nl} = 1.5$ at different values of $k_B T/\varepsilon_{ll}$, the dimensionless temperature, as indicated in the key. The corresponding bulk fluid phase diagram is in Fig.7.4.

where the Helmholtz free energy F is given by Eq. (7.2.6) and the chemical potentials μ_l and μ_n are set to be the values at which vapour-liquid phase coexistence occurs. In Fig. 7.5 we display the density profiles of the solvent and the nanoparticles for the case when $\mu_n/\varepsilon_{ll} = -8$, $\varepsilon_{nl}/\varepsilon_{ll} = 0.75$ and $\varepsilon_{nn}/\varepsilon_{ll} = 1.5$ and various temperatures. The corresponding bulk fluid phase diagram is displayed in Fig. 7.4. We see that as the temperature is increased the total density difference between the two coexisting phases decreases. We note also that at lower temperatures, $k_B T/\varepsilon_{ll} \lesssim 1.8$, there is a small enhancement of the nanoparticle density at the interface, indicating that the nanoparticles have a slight propensity towards being surface active [15] for these values of ε_{nl} and ε_{nn}. As we show below, this slight surface enhancement in equilibrium can become greater during non-equilibrium droplet evaporation.

7.4.2 Surface tension

Having calculated interfacial density profiles such as those in the Fig. 7.5, we can then substitute back into Eq. (7.4.1) to calculate the grand potential, Ω, of the whole system, including the interface.

The surface tension is defined as the excess free energy in the system due to the presence of an interface between two coexisting phases. Subtracting the grand potential $\Omega_0 = -PV$ for a system with the same volume V, temperature and chemical potentials but containing either only the uniform vapour or liquid gives the excess grand potential due to the interface. The interfacial tension is then

$$\gamma = \frac{\Omega + PV}{A}, \tag{7.4.2}$$

where A is the area of the interface. From the density profiles in Fig. 7.5, this gives γ_{gl}, the planar liquid-gas interfacial tension. In a similar manner, for the fluid at the wall exerting potentials $\Phi_{\mathbf{i}}^l$ and $\Phi_{\mathbf{i}}^n$ we can calculate γ_{wl}, the wall-liquid interfacial tension and γ_{wg}, the wall-gas interfacial tension. These are all calculated for $\mu_l = \mu_l^{\mathrm{coex}}$ and $\mu_n = \mu_n^{\mathrm{coex}}$, the values at bulk gas-liquid phase coexistence.
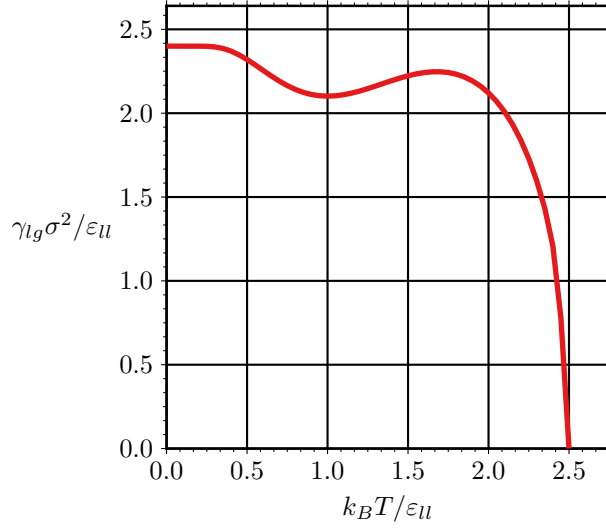
Figure 7.6: The liquid-gas surface tension as a function of temperature, calculated using DFT. The corresponding bulk fluid phase diagram is in Fig. 7.1.

From these interfacial tensions one can then calculate the contact angle a droplet of liquid would have with the surface using Young's equation [14],

$$\theta = \arccos\left(\frac{\gamma_{wg} - \gamma_{wl}}{\gamma_{lg}}\right). \tag{7.4.3}$$

Fig. 7.6 shows the liquid-gas surface tension for the pure liquid ($\mu_n = -\infty$) plotted as a function of temperature. There is a slight local minimum in the surface tension at $k_BT/\varepsilon_{ll} \approx 1.0$. In the limit $T \to 0$ the density of the liquid $\rho_l \to 1$ and the coexisting gas has $\rho_l \to 0$. It is then straightforward to see from Eq. (7.2.1) or Eq. (7.2.6) that for $T \to 0$ the surface tension $\gamma_{lg}/\varepsilon_{ll} \to 12/5$. At the critical temperature, $T = T_c = 2.5\varepsilon_{ll}/k_B$, the density difference between the two coexisting phases goes to zero, so as $T \to T_c$, $\gamma_{lg} \to 0$.

Fig. 7.7 shows the contact angles calculated from the DFT for the pure liquid at the temperature $k_BT/\varepsilon_{ll} = 1.0$, as the attraction due the surface is varied. We see that for $\varepsilon_{lw}/\varepsilon_{ll} > 0.97$ the contact angle $\theta = 0$, i.e. the liquid wets the surface. In contrast, for $\varepsilon_{lw}/\varepsilon_{ll} < 0.97$ the liquid is only partially wetting. As the attraction to the surface ε_{lw}

is decreased below this value, the contact angle θ increases and can become large, as the surface becomes increasingly solvophobic. It is also possible to directly measure the contact angle by fitting a circle to an equilibrium droplet density profile calculated using DFT (e.g. using the method in [55]), which gives almost identical results [38]. Such a droplet density profile is calculated by constraining the total volume of liquid in the system to be fixed and also allowing the density to vary in both perpendicular and parallel directions to that surface – see Ref. [38] for further details. For comparison, in Fig. 7.7 we also show the contact angles measured by fitting a circle to equilibrium density profiles calculated in [77] using MC simulations of droplets on surface, using Hamiltonian (7.2.1). At higher values of $\varepsilon_{lw}/\varepsilon_{ll}$ the curves are almost identical but at lower values the MC simulations give a higher contact angle. We believe this is due to the fact that at higher values of ε_{lw} the energetic contributions to the free energy dominate and so the DFT describes the droplet accurately. However, for smaller ε_{lw}, i.e., a solvophobic surface, the fluctuations of the liquid near the surface and in the contact line region are significant [85, 86] and so the mean-field DFT, which neglects some fluctuation contributions to the free energy, does less well. We should emphasise, however, that interfacial tensions and especially the contact angle θ are quantities that depend very sensitively on approximations, so the agreement in Fig. 7.7 is actually rather good.

7.5   Theory for the non-equilibrium dynamics

We assume that the non-equilibrium fluid dynamics is described by DDFT [7, 8, 9]. This is a good assumption to make for the nanoparticle dynamics, since it is a theory for Brownian particles suspended in a liquid, as derived in [7, 8, 9]. However as discussed in [10, 11], the theory can also approximate the dynamics of molecular liquids, especially when the fluid is not too far from equilibrium, which is certainly true for the cases of interest here. For a two
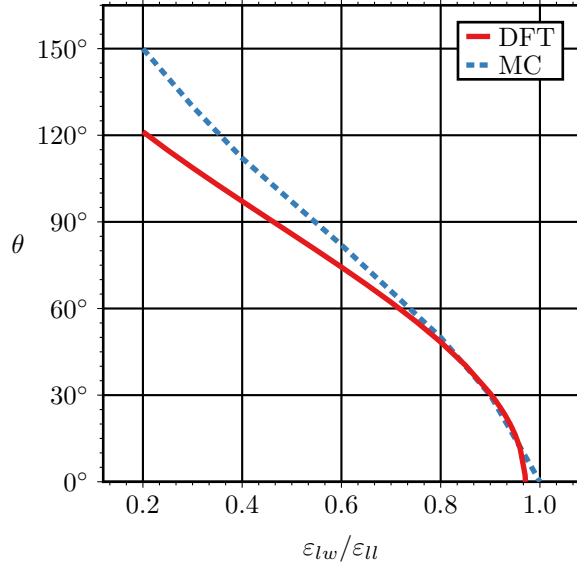
Figure 7.7: The contact angle for a droplet on a surface with temperature $k_B T / \varepsilon_{ll} = 1.0$. The solid line is the result from DFT using the interfacial tensions together with Young's equation (7.4.3). The dashed line is the corresponding results from MC simulations [77].

component system, DDFT generalises to give the following pair of coupled equations [87]

$$\frac{\partial \rho_{\mathbf{i}}^l}{\partial t} = \nabla \cdot \left[M_{\mathbf{i}}^l \rho_{\mathbf{i}}^l \nabla \frac{\partial F}{\partial \rho_{\mathbf{i}}^l} \right], \tag{7.5.1}$$

$$\frac{\partial \rho_{\mathbf{i}}^n}{\partial t} = \nabla \cdot \left[M_{\mathbf{i}}^n \rho_{\mathbf{i}}^n \nabla \frac{\partial F}{\partial \rho_{\mathbf{i}}^n} \right], \tag{7.5.2}$$

where $M_{\mathbf{i}}^l$ and $M_{\mathbf{i}}^n$ are the mobility coefficients for the liquid and nanoparticles and F is the Helmholtz free energy. The average densities of the liquid and nanoparticles at site $\mathbf{i}$, $\rho_{\mathbf{i}}^l$ and $\rho_{\mathbf{i}}^n$, respectively, are now both functions of time t. Note that since the system we consider here is a lattice model, the ∇ operators in Eqs. (7.5.1) and (7.5.2) are implicitly the finite difference approximations. For more details on this, see Ref. [49] and also the Appendix below.

Here, we generalise the mobilities $M_{\mathbf{i}}^l$ and $M_{\mathbf{i}}^n$ to be mobility matrices which depend on both position $\mathbf{i}$ and the direction of the fluid flow, so as to model the effect of slip, partial-slip

or no-slip at the surface. Thus we set the mobility matrix at site $\mathbf{i}$ for species c to be

$$
M_{\mathbf{i}}^c =
\begin{cases}
m_{\mathbf{i}}^c \begin{pmatrix} s & 0 & 0 \\ 0 & v & 0 \\ 0 & 0 & s \end{pmatrix} & j = 1, \\[2em]
m_{\mathbf{i}}^c \begin{pmatrix} 1 & 0 & 0 \\ 0 & 1 & 0 \\ 0 & 0 & 1 \end{pmatrix} & \text{otherwise,}
\end{cases}
\tag{7.5.3}
$$

where s and v are parameters that allows us to model the effects of slip at the surface. $m_{\mathbf{i}}^c$ is the local mobility coefficient for species c. For the liquid, we set $m_{\mathbf{i}}^l$ to be a constant, m_l. However, following Ref. [49], for the nanoparticles we set

$$
m_{\mathbf{i}}^n = \frac{m_n}{2}\left(\tanh(8\rho_{\mathbf{i}}^l - 4) + 1\right).
\tag{7.5.4}
$$

This is a smooth function that is $\approx m_n$ when the solvent density is high and ≈ 0 when the solvent density is low. This reflects the fact that the origin of the nanoparticle motion is due to the Brownian motion from being suspended in the solvent and so the nanoparticles should be immobile when there is no solvent liquid surrounding them [77, 49]. It also prevents the nanoparticles from moving around once the liquid has evaporated. Henceforth we set $m_n = m_l = 1$, so that all times are given in terms of the Brownian timescale $\tau_B = \sigma^2/m_n k_B T$.

The parameter s in Eq. (7.5.3) determines the fluid mobility parallel to the surface in the first layer of lattice sites ($j = 1$). The parameter v controls the mobility from the first to the second layer, in the direction perpendicular to the surface. If there is slip, then $s = v = 1$. When there is no-slip or partial-slip then $s = 0$ and $v \ll 1$. As we show below, the receding fluid contact angles are determined by the value of v.

We solve this system numerically on a lattice with a finite time step. The divergence and gradients in Eqs. (7.5.1) and (7.5.2) are performed using nearest neighbour finite difference

approximations. Care in how these are done is needed to prevent numerical instabilities. We use a mix of forward and backward finite differences. At a particular time step, if a forward finite difference for the gradient is used then a backward finite difference is used for the divergence. As time precedes the direction of the spatial finite difference is alternated to prevent a directional bias that can lead to droplets drifting across the surface. More detail about the finite difference integration scheme is given in the Appendix.

7.6 Evaporating droplets

7.6.1 Influence of slip at the surface

First, we discuss the behaviour of evaporating liquid ridges that do not contain any nanoparticles. We assume that the fluid density profile only varies in one of the directions parallel to the surface in order to simplify the numerics. However, we expect the results to be similar to those one would obtain for a droplet that is initially circularly symmetric with diameter equal to the width of the liquid ridge, so henceforth we refer to them as 'droplets'. Evaporation is simulated by fixing the liquid density of the lattice sites at the top of the simulation box to a very low value (10^{-8}). This emulates an open system with a mechanism, (e.g. air-flow over the top of a container) for taking the solvent vapour out of the system. The evaporation rate of a droplet depends very sensitively on the distance from the top layer of lattice sites from which the liquid is removed down to the top of the droplet. If the distance is small the droplet evaporates relatively quickly. On the other hand, if the distance to the top of the container is large, the droplet evaporation is slow. Here, we set the system size to be three times the height of the initial droplet. This sets the overall timescale for evaporation: it is determined by the time it takes for the vapour to diffuse the height of the system.

In Fig. 7.8 we display results for a surface with the slip parameters $s = v = 1$, for the evaporation of a droplet that initially has semicircular cross-section and with equilibrium contact angle $\approx 90°$. As it evaporates, the droplet retains its semicircular shape and has a
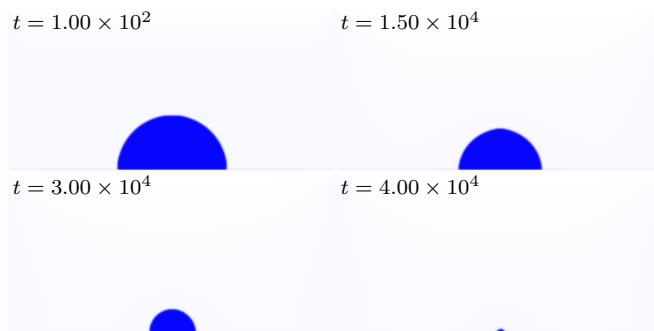
Figure 7.8: Snapshots of a droplet evaporating from a surface calculated using DDFT with $s = v = 1$ (corresponding to slip at the surface), $\varepsilon_{wl}/\varepsilon_{ll} = 0.45$, $k_B T/\varepsilon_{ll} = 1.3$ in a 128×64 system. The times at which the snapshots occur are given on each figure and are in units of the Brownian timescale τ_B.
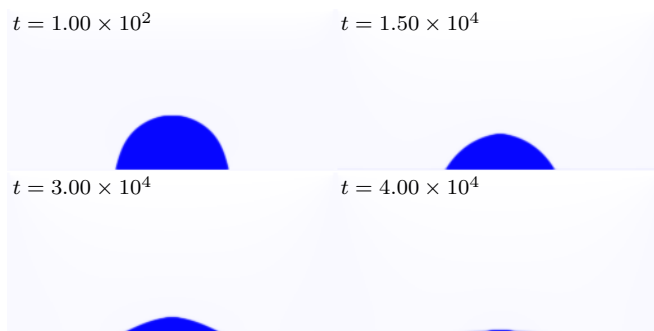
Figure 7.9: Snapshots of a droplet evaporating from a surface with $s = 0$, $v = 0.001$ (corresponding to no-slip at the surface and a small receding contact angle), $\varepsilon_{wl}/\varepsilon_{ll} = 0.45$, $k_B T/\varepsilon_{ll} = 1.3$ in a 128×64 system. The times are given on each snapshot.

receding contact angle that remains almost equal to the equilibrium contact angle. This is a consequence of the smoothness of the surface on which the droplet is sitting and due to the slip at the surface, since $s = v = 1$. However, most observed evaporating droplets have (at least initially) a pinned contact line. This is due to the fact that almost all real surfaces are rough, at least on the microscopic scale. It is also interesting to note in Fig. 7.8 the slight vertical density gradient in the vapour, due to the absorbing upper boundary.

By setting the slip parameter $s = 0$ we prevent any density exchange between neighbouring lattice sites directly above the surface, i.e. those in the $j = 1$ layer. The density in these lattice sites can only vary by exchanging mass with the $j = 2$ lattice sites above them. The rate at which this occurs is set by the parameter v. Fig. 7.9 shows snapshots of a droplet
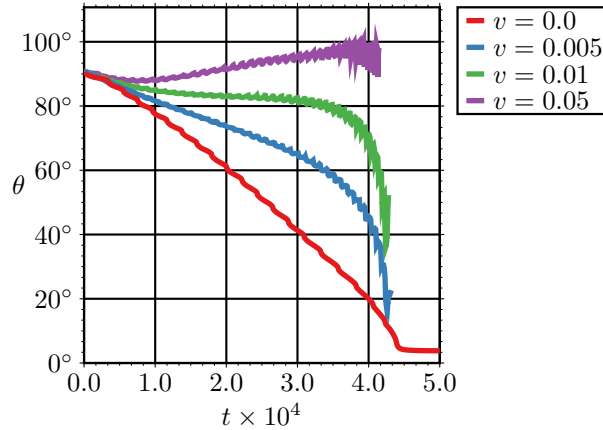
Figure 7.10: The contact angle as a function of time for slip parameters $s = 0$ and various values of v, as given in the key. The line stops when the droplet has evaporated (in the $v = 0$ case the droplet never fully evaporates since for this case the $j = 1$ layer directly above the surface is completely immobile). The value $v = 0.05$ gives very similar results to $v = 1$, i.e. for $v \geq 0.05$ the behaviour is independent of v.

evaporating from a surface when the slip parameters $s = 0$ and $v = 0.001$. We see that the effect of this decreased mobility near the surface is to pin the contact line, modelling the effect of surface roughness. The contact lines stay almost stationary at the beginning of the simulation until the droplet reaches the receding contact angle (in the case in Fig. 7.9, this is rather small in value). At this stage the droplet continues evaporating with a moving contact line until it has completely evaporated. We calculate the contact angle over time using the circle-fitting method of Refs. [77, 55] (see also section 7.4.2). Results from doing this are shown in Fig. 7.10, for various values of v. We see that when $s = 0$ the selected value of v specifies the receding contact angle. Note that there are small oscillations over time in the value of the receding contact angle created by the top of the droplet moving from one layer of lattice sites to another. This artefact of the lattice can also be seen in the underlying binding potential, as discussed in Ref. [38]. Note also that in the final stages the droplet becomes very small so the circle fitting becomes less and less accurate until eventually it becomes ill-defined.

7.6.2   Evaporating droplets of nanoparticle suspension

Now we consider the evaporation of droplets containing nanoparticles. Since the vapour
density near the top of the simulation box is always low, due to Eq. (7.5.4) there is a
very low probability of nanoparticles entering the vapour and escaping the system. The
method for incorporating the effects of surface roughness (i.e. no-slip) via Eq. (7.5.3) is also
applied to the nanoparticles, using the same values of s and v. We assume that the initial
density of the nanoparticles in the liquid droplet is $\rho_n = 0.05\rho_l$, i.e. the initial concentration
$\rho_n/(\rho_l + \rho_n) \approx 0.048$.

Fig. 7.11 shows snapshots of a droplet of nanoparticle suspension evaporating from a
surface with almost no-slip ($s = 0$, $v = 0.005$). As evaporation proceeds the local density
of the nanoparticles at the gas-liquid interface builds up to form a crust on the surface of
the droplet, with the nanoparticle density at the interface becoming approximately twice
the density inside the droplet. By the time $t = 2.98 \times 10^4$ a buildup of nanoparticles at the
contact line has started to appear, as can be seen in Fig. 7.12. This is the start of significant
change in the nanoparticle density distribution. A short time thereafter $t = 3.00 \times 10^4$,
the majority of the nanoparticles have collected together at the contact line. This occurs
due to phase separation within the droplet, between a nanoparticle rich phase (with a low
density of the solvent) and a nanoparticle poor phase (with a high density of the solvent)
– i.e. a liquid-liquid phase separation. The phase separation is driven by the fact that as
the solvent evaporates, the concentration of the nanoparticles within the droplet slowly rises.
The separation is triggered when the nanoparticle density reaches the value where the system
becomes unstable to demixing. The phase separation occurs relatively rapidly, depositing
the nanoparticles in two piles at the contact lines. By the time $t \approx 4.8 \times 10^4$ the bulk of the
solvent has evaporated and the majority of the nanoparticles are at the contact lines. Beyond
this time, the density profiles no longer change in time. Recall that we have assumed that
the system is invariant in one direction, i.e. an evaporating liquid ridge. Thus, the deposited
nanoparticles correspond to two parallel lines of nanoparticles deposited where the edges of
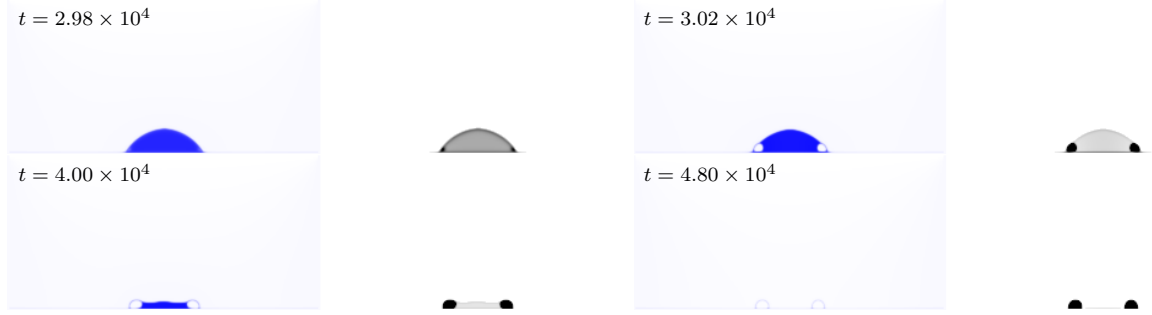
Figure 7.11: Snapshots during the evaporation of a droplet of nanoparticle suspension from a surface with $\varepsilon_{wl}/\varepsilon_{ll} = 0.8$, $\varepsilon_{ln}/\varepsilon_{ll} = 0.75$, $\varepsilon_{nn}/\varepsilon_{ll} = 1.5$ and $k_B T/\varepsilon_{ll} = 1.3$, $s = 0$ and $v = 0.005$ in a 256×128 system. In each pair of density profiles, the solvent is on the left and the nanoparticle density profile is on the right.

Figure 7.12: Magnification of a portion of the time $t = 2.98 \times 10^4$ nanoparticle density profile in Fig. 7.11, in the contact line region.

the liquid ridge was initially located. However, if the droplet had initially been circular, then the nanoparticle deposit would correspond to a ring, like a coffee stain. Note, however, that the mechanism just described for the formation of this structure is completely different from that which is normally invoked for coffee ring stain formation, where it is the advective hydrodynamic fluid flow within the droplet from the centre towards the edge, driven by the evaporation, that leads to a pile-up of the suspended particles at the pinned contact line. In the present model there is no advective hydrodynamics and it is for thermodynamic reasons (i.e. the phase separation) that the nanoparticles are deposited at the contact line.

In Fig. 7.13 we present results for a case where there is slip at the surface (i.e. $s = 1$, $v = 1$), in contrast to the previous case in Figs. 7.11 and 7.12. Fig. 7.13 displays snapshots from the evaporation of a wider droplet that is initially pancake-like, with a flat top. As

$t = 5.00 \times 10^1$ $t = 5.00 \times 10^3$

$t = 1.50 \times 10^4$ $t = 2.50 \times 10^4$

Figure 7.13: Snapshots taken from simulating a droplet of nanoparticle suspension evaporating from a surface with $\varepsilon_{wl}/\varepsilon_{ll} = 0.8$, $\varepsilon_{ln}/\varepsilon_{ll} = 0.75$, $\varepsilon_{nn}/\varepsilon_{ll} = 1.5$, $k_BT/\varepsilon_{ll} = 1.3$ and slip $s = v = 1$ in a 128×64 system.

the liquid evaporates, a crust of nanoparticles still forms at the gas-liquid interface, but in this case the contact line also recedes, due to the slip at the surface. There is a buildup of nanoparticles at the contact line, which is enhanced compared to the case in Figs. 7.11 and 7.12, due to the fact that the contact line is receding. As it recedes, the demixing transition is triggered, so there is a deposition of the nanoparticles partway between the initial location of the contact line and the centre of the droplet. Furthermore, not all of the nanoparticles are deposited at this stage, due to the larger size of the droplet. As evaporation continues, the contact lines de-pin from the nanoparticle deposits and further recede. There is therefore again an increase in the concentration of the nanoparticles in the droplet and also a build up at the contact line untill again the phase transition is triggered, leading to a second deposition of nanoparticles closer to the centre. These deposits are somewhat smaller than the first. We believe that for different parameter values and for even larger droplets, this process could lead to the formation of a deposit consisting of a greater number of concentric rings and perhaps even of a periodic nanoparticle deposition. This would appear similar to the periodic nanoparticle deposition process described in Refs. [69, 28, 30, 31] and the (experimental) references therein. However, the mechanism here is entirely different: it is due to the thermodynamics of phase separation, rather than due to advective fluid-dynamics.

For the parameter values used here, when we keep the initial height of the droplet the same, but make the width greater, we see in Fig. 7.14 something different: At the receding

contact line, we still see the deposition just described. However, in the middle of this wide pancake-like droplet, when the concentration of the nanoparticles reaches a high enough level due to the evaporation, we see spinodal demixing occurring in the middle of the film. This has a characteristic wavelength and so leads to a periodic array of nanoparticle deposits on the surface. Such spinodal dewetting may be triggered through the coupling of film height and solute concentration flucations [88]. In the present system it is not clear whether it is a surface instability, a bulk instability or a coupling of the two that selects the wavelength of the structure in the centre of the droplet in Fig. 7.14. The characteristic wavelength is also seen in the small amplitude periodic modulation in the thickness of the liquid film, that is a precursor to the demixing. The nanoparticle deposits occur where the troughs are located. In this situation the film is so thin that the surface and what is left of the bulk of the film are strongly coupled. The coupling of demixing within the film to the film height has been observed e.g. in films of polymer blends [89]. For a detailed discussion of demixing in thin liquid films and how this may couple to the film height profile, see Ref. [90]. There may be regimes where this leads to demixing induced front instabilities [76, 91].

7.7 Concluding remarks

We have described a DDFT model for the evaporation of droplets of a nanoparticle suspension from surfaces. We have shown that the model can include the effects of (no)slip at the surface, nanoparticle crust formation and nanoparticle aggregation which leads to the deposition of ring deposits and other more complex structures.

A particularly striking result of the present work is the observation that the coffee stain effect can still arise in a system with no advective hydrodynamics to carry the suspended nanoparticles to the contact line. Here we show that the thermodynamics of aggregation and phase separation can also lead to the formation of ring stains. Furthermore, it can also lead to the formation of multiple rings. Further work is required to see if there is a regime within the
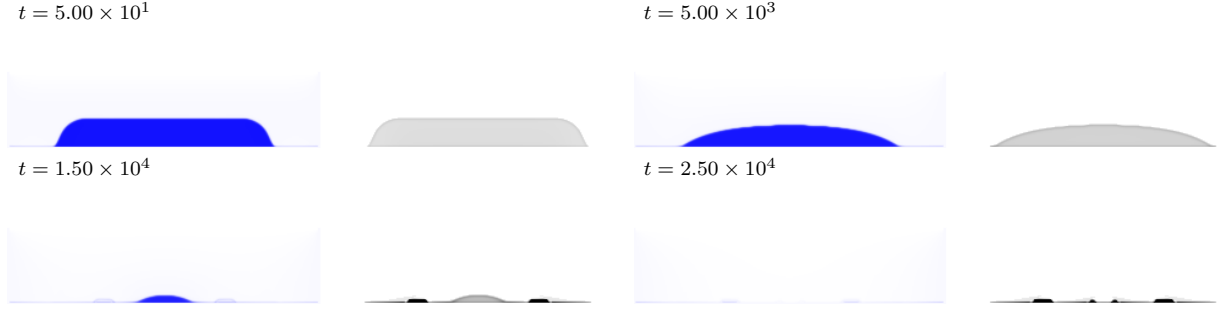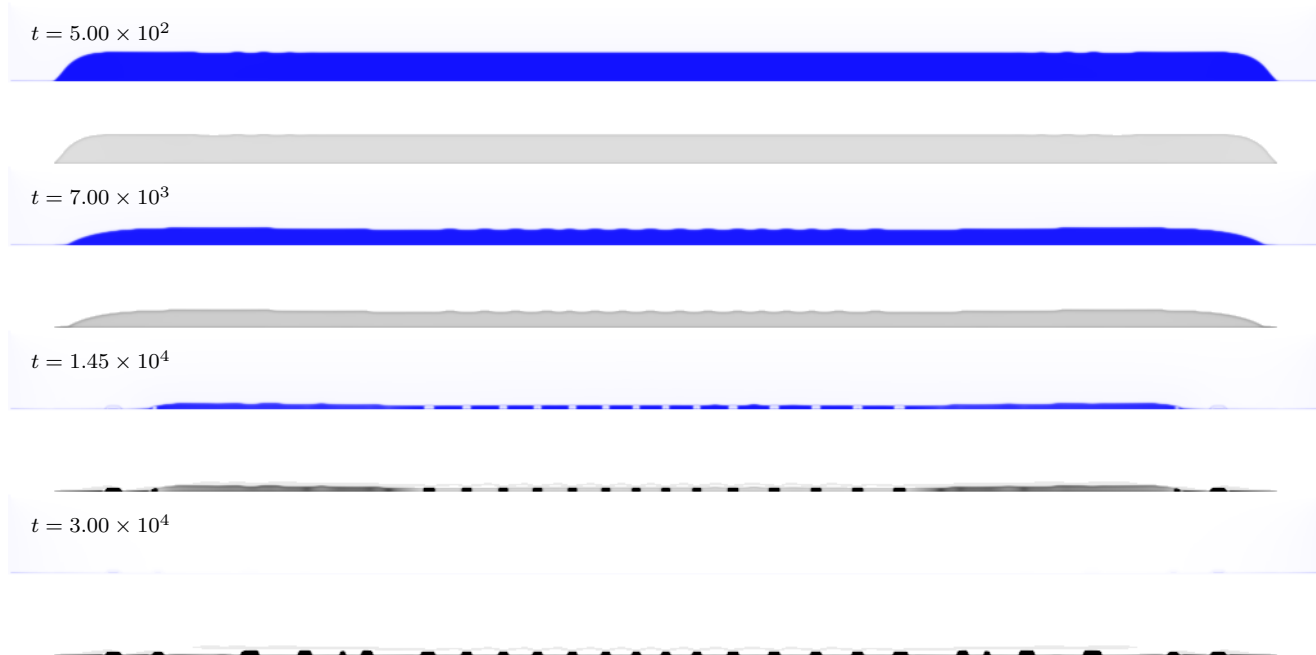
Figure 7.14: Snapshots taken from simulating a pancake-like droplet of nanoparticle suspension evaporating from a surface with $\varepsilon_{wl} = 0.8$, $\varepsilon_{ln} = 0.75$, $\varepsilon_{nn} = 1.5$ and $k_B T / \varepsilon_{ll} = 1.3$ in a 1024×64 system.

present model where periodic line deposition can be observed, as in certain hydrodynamic models [30, 31]. We believe there probably is a regime where periodic deposition occurs, however for the parameter values and system sizes we have so far explored, we have not observed this.

The main direction where the present approach should be extended is to incorporate the advective hydrodynamics of the solvent liquid. The DDFT is certainly adequate for describing the dynamics of the nanoparticles. However, for the solvent dynamics, especially for situations such as sliding droplets on inclined planes (see e.g. [92]), then the present approach is likely not adequate. That said, since the theory is based on a free energy functional incorporating the correct thermodynamics, it should remain qualitatively correct, at least for when the system is not driven too far from equilibrium.

Indeed, this is one of the great advantages of using DFT and DDFT as the theoretical foundation: these base the theory on a free energy function(al) – in the present case, Eq.

(7.2.6) – so as a result, this gives easy access to important thermodynamic quantities such as the pressure, surface tension and equilibrium contact angle. Obtaining these from MC simulations or other approaches is generally more complicated and requires more lengthy computations [77].

Acknowledgements

7.8 Appendix

We integrate the coupled Eqs. (7.5.1) and (7.5.2) forward in time using the Euler algorithm:

$$\rho_{\mathbf{i}}^c(t + \Delta t) = \rho_{\mathbf{i}}^c(t) + \frac{\partial \rho_{\mathbf{i}}^c}{\partial t} \Delta t, \qquad (7.8.1)$$

where $c = l, n$ and we replace the terms $\partial \rho_{\mathbf{i}}^c / \partial t$ by the respective expressions in either the right hand side of Eq. (7.5.1) or Eq. (7.5.2). We use the value $\Delta t = 10^{-5}$.

To evaluate the spatial finite differences in the direction parallel to the surface, we do the following: Let d be the direction in which we take the derivative. d alternates between 1 and -1 from one time step to the next to prevent any direction bias. The following quantity

$$\rho^c \nabla \left. \frac{\partial F}{\partial \rho^c} \right|_{(i,j)} = \left(I_{(i,j)}^c, J_{(i,j)}^c \right), \qquad (7.8.2)$$

which occurs in the right hand sides of Eqs. (7.5.1) and (7.5.2), is evaluated as

$$
I^c_{(i,j)} = \frac{\rho^c_{(i,j)} + \rho^c_{(i+d,j)}}{2} \left(\left. \frac{\partial F}{\partial \rho^c} \right|_{(i+d,j)} - \left. \frac{\partial F}{\partial \rho^c} \right|_{(i,j)} \right),
\tag{7.8.3}
$$

$$
J^c_{(i,j)} = \frac{\rho^c_{(i,j)} + \rho^c_{(i,j+1)}}{2} \left(\left. \frac{\partial F}{\partial \rho^c} \right|_{(i,j+1)} - \left. \frac{\partial F}{\partial \rho^c} \right|_{(i,j)} \right).
\tag{7.8.4}
$$

Note that we have assumed that for all time the densities remain invariant in the direction indexed by k, where $\mathbf{i} = (i, j, k)$. If this is not the case, then there is an additional component of the same form as Eq. (7.8.3).

Multiplying Eq. (7.8.2) by the respective mobility matrix from Eq. (7.5.3) we obtain

$$
(X^c_{\mathbf{i}}, Y^c_{\mathbf{i}}) = M^c_{\mathbf{i}} \rho^c_{\mathbf{i}} \nabla \frac{\partial F}{\partial \rho^c_{\mathbf{i}}}.
\tag{7.8.5}
$$

Now when we take the divergence we use the opposite direction d:

$$
\nabla \cdot (X^c_{\mathbf{i}}, Y^c_{\mathbf{i}}) = X^c|_{(i,j)} - X^c|_{(i-d,j)} + Y^c|_{(i,j)} - Y^c|_{(i,j-1)}.
\tag{7.8.6}
$$

This is the expression we use for $\partial \rho^c_{\mathbf{i}} / \partial t$ in Eq. (7.8.1).

Chapter 8

Two-dimensional colloidal fluids exhibiting pattern formation

Two-dimensional colloidal fluids exhibiting pattern formation

Blesson Chacko, Christopher Chalmers, and Andrew J. Archer

Department of Mathematical Sciences, Loughborough University, Loughborough, Leicestershire, LE11 3TU, UK

Fluids with competing short range attraction and long range repulsive interactions between the particles can exhibit a variety of microphase separated structures. We develop a lattice-gas (generalised Ising) model and analyse the phase diagram using Monte Carlo computer simulations and also with density functional theory (DFT). The DFT predictions for the structures formed are in good agreement with the results from the simulations, which occur in the portion of the phase diagram where the theory predicts the uniform fluid to be linearly unstable. However, the mean-field DFT does not correctly describe the transitions between the different morphologies, which the simulations show to be analogous to micelle formation. We determine how the heat capacity varies as the model parameters are changed. There are peaks in the heat capacity at state points where the morphology changes occur. We also map the lattice model onto a continuum DFT that facilitates a simplification of the stability analysis of the uniform fluid.

I. INTRODUCTION

When the forces between colloidal particles suspended in a liquid are sufficiently strongly attractive, they can exhibit phase separation into a high density colloidal fluid, referred as a colloidal "liquid" and low density suspension, a colloidal "gas".[1] However, in some circumstances, the interactions can be attractive at short ranges when the particle cores are close to one another, but at longer ranges be repulsive. These short-range attractive, long-range repulsive (SALR) potentials can arise in certain suspensions of charged colloids and polymers[2] and also in protein solutions.[3] Self-consistent Ornstein-Zernike approximation (SCOZA) integral equation theory for a model of such systems,[4,5] showed that when the long range repulsion is not too strong there is a large region of the phase diagram where the correlations in the fluid show significant fluctuation effects and where the compressibility increases significantly. The SCOZA theory (which is sophisticated and rather accurate) was also compared with results from DFT,[6] which showed good agreement between the theories for the liquid structure. When the long range repulsion is further increased, the SALR interaction between the particles gives rise to pattern formation in the fluid state, such as gathering to form clusters, stripes (lamellas) and holes (bubbles), referred to as microphase separation. In Ref. 7 Monte Carlo (MC) computer simulations and integral equation theory was used to understand the details of the relation between the liquid-vapour transition line and the occurrence of any microphase separated phases. As the repulsion strength is increased, starting from the critical point, the gas-liquid phase separation is replaced by microphase separation. In Ref. 8, a study of the cluster formation showed that it is very similar to micelle formation in aqueous surfactant solutions. However, for the system considered in Ref. 9, discontinuities in thermodynamic quantities were observed at the onset of cluster formation, suggesting it is indeed a phase transition.

Further understanding of the phase ordering in SALR systems was recently gained by Pekalski and co-workers[10]

by studying a simple one-dimensional lattice model, in which the SALR interaction was modelled using an attractive interaction between neighbouring particles, repulsion between the third neighbours and no interaction between second neighbours or any other neighbours. An exact solution was presented using the transfer matrix method. The same SALR system was then extended to two-dimensions (2D) on a triangular lattice,[11,12] where microphase separated phases and also a reentrant uniform liquid is observed in the phase diagram. This approach, based on using lattice models to elucidate the nature of the structure formation in systems with competing interactions, has a long track record, going back to seminal works, such as Refs. 13,14. There are several advantages of using lattice models stemming from the fact that they are much more straightforward to analyse than the equivalent continuum models and also the computations are much simpler, allowing larger systems to be simulated over longer times. Due to the fact that the clusters and other structures formed can be more than an order of magnitude larger than the size of the individual particles, to properly observe the microphase formation, the system size generally needs to be much larger than that one would use for studying simple gas-liquid systems. There have also been other (field) theoretical and simulation studies considering aspects of the phase behaviour of a variety of fluids interacting via SALR potentials.[15–18]

The more recent interest in SALR systems in 2D stems from the experimental observation of microphase-ordering of nanoparticles at a water-air interface,[19,20] which led to theoretical and simulation work to understand the nature of the structures that are formed. Imperio and Reatto[21–23] made a detailed study of the phase diagram using parallel-tempering MC simulations to determine the location in the phase diagram of the microphase separated states for a 2D fluid of particles interacting via the double-exponential pair potential

$$u(r) = \begin{cases} \infty, & \text{if } r < \sigma \\ -\dfrac{\varepsilon_a \sigma^2}{R_a^2} e^{-r/R_a} + \dfrac{\varepsilon_r \sigma^2}{R_r^2} e^{-r/R_r}, & \text{otherwise} \end{cases} \quad (1)$$

where r is the distance between the centres of the particles, which have a hard-core of diameter σ. The short range attraction has strength determined by ε_a and range R_a. Similarly, the repulsion strength is determined by ε_r and has range R_r. When $R_a = \sigma$, $R_r = 2\sigma$ and $\varepsilon_a = \varepsilon_r = \varepsilon$, microphase ordering is observed for temperatures $k_B T/\varepsilon \lesssim 0.6$, where k_B is Boltzmann's constant. At lower densities this takes the form of clusters or "droplets", whilst at higher densities striped structures were observed. At even higher densities a hole phase is observed, although here the simulations can be difficult to perform. Imperio and Reatto[21–23] showed that at the onset of microphase ordering, one observes a peak in the heat capacity and this was used to identify the location in the phase diagram of the microphase ordered states. Following this, a DFT model for this system was developed,[24] which is in good qualitative agreement with simulation results with regard to the topology of the phase diagram and the structure of the fluid and inhomogeneous phases. The DFT also predicts that the transitions from the uniform to the modulated fluid phases are all either first or second order phase transitions,[24] However, the DFT is a mean-field theory and so one should be cautious about accepting this prediction of the theory.

The aim of the work described here is to study the formation of patterns using both MC computer simulations and also DFT for a 2D lattice model in order to determine the nature of the transitions to and between the different microphase ordered structures and also to compare between the methods in order to elucidate what aspects of the microphase ordering the mean-field DFT is able to describe. We fix the strength of the repulsion between the particles to a particular value and we also fix the temperature and then calculate the properties of the fluid as the density and the strength of the attractive interactions between the particles are varied. In particular, we calculate the heat capacity and determine the phase diagram. We also map the lattice model onto a continuum DFT that allows a simple calculation of roughly where in the phase diagram one can expect to find the microphase ordering. This takes the form of a linear stability analysis.

This paper is laid out as follows: In Sec. II we define the model fluid and in Sec. III we present MC computer simulation results, including for the heat capacity, for the ratio of particles in the system within the clusters as the total density in the system is increased and for the static structure factor. In Sec. IV we present the lattice DFT results, comparing with the MC results and calculating the fluid phase diagram. In Sec. V we map onto a continuum DFT and discuss the linear stability of the fluid. Finally, in Sec. VI we draw our conclusions.

II. THE MODEL FLUID

We assume that the colloids interact via the pair potential

$$u(r) = \begin{cases} V(r) & r \geq \sigma \\ \infty & r < \sigma, \end{cases} \quad (2)$$

where r is the distance between the centres of the two particles and the tail of the potential is given by the double-Yukawa potential[7]

$$V(r) = \begin{cases} -\dfrac{\varepsilon e^{-z_1(r-\sigma)/\sigma}}{r/\sigma} + \dfrac{A e^{-z_2(r-\sigma)/\sigma}}{r/\sigma} & r \geq \sigma \\ 0 & r < \sigma \end{cases} \quad (3)$$

where ε is the attraction strength coefficient and A is the repulsion strength coefficient. The parameters z_1 and z_2 determine the range of the attraction and repulsion, respectively. σ is the diameter of the particles, which we set to be our unit of length. We fix the coefficients $z_1 = 2$ and $z_2 = 0.2$ so that the potential is of the form illustrated in Fig. 1.

In order to simplify the analysis and to reduce the computational costs, we assume that the positions of the particles are discrete variables, and represent the fluid via a 2D lattice model, containing M lattice sites and with periodic boundary conditions. We use a square lattice of size $L \times L$, with lattice spacing equal to the diameter of the particles σ and we assume that each lattice site can be occupied by at most one colloid. We denote a particular configuration of particles by a set of occupation numbers $\{n_i\}$, such that, if the site i is empty, then $n_i = 0$ and $n_i = 1$, if it is occupied. Note that i here is used as a short form for the position on the 2D lattice, at point (j, k). We treat the system in the grand canonical ensemble and so the Hamiltonian of our lattice model can be written as[25]

$$E\left(\{n_i\}\right) = \sum_{i=1}^{M} n_i(\Phi_i - \mu) + \frac{1}{2}\sum_{i,j} V_{i,j} n_i n_j, \quad (4)$$

where Φ_i is the external potential at the lattice site i and μ is the chemical potential which determines the number
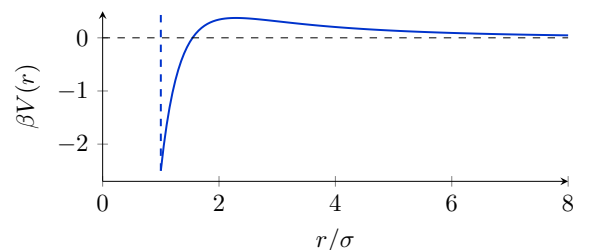

FIG. 1: The double-Yukawa pair interaction potential between the particles, in the case when the parameters are $\beta A = 1.5$, $z_1 = 2$, $z_2 = 0.2$ and $\beta\varepsilon = 4$.

of particles in the system N. The final term is the energy contribution due to the interactions between particles, where $V_{i,j}$ is the pair interaction potential between two particles at sites i and j, which is the discrete lattice version of the potential in Eq. (3), i.e. evaluated by taking r in Eq. (3) to be the distance between sites i and j. We also assume that there are no three-body or higher-body interactions between the particles. Since here we only consider the ordering in the bulk fluid, we henceforth assume that $\Phi_i = 0$, $\forall i$. Also, in all our MC and DFT results below, we truncate the tail of the pair potential beyond $r = r_c = 16\sigma$. It is also worth noting that the lattice model Hamiltonian (4) has a symmetry between particles and holes (i.e. replacing $n_i \to 1-n_i$) that, as we show below, results in the phase diagram of the system being symmetric around the density $\rho = \langle n_i \rangle = 1/2$.

III. MONTE CARLO

We study the system using standard Metropolis MC simulations.[26] The lattice is initiated in a state where all the sites are randomly occupied by a particle with probability 0.5. At each step during the simulation, a random lattice site i is selected and we then calculate the change in energy ΔE using Eq. (4) when the occupation number for that lattice site is replaced $n_i \to (1 - n_i)$. Thus, if the site is already occupied, the trial change is to remove the particle and if the site is unoccupied, the trial move it to insert a particle at that site. If ΔE is negative, then we keep the change. Otherwise, we only keep the change with probability, $e^{-\beta \Delta E}$.

In Fig. 2, we display typical snapshots from our MC simulations for a range of state points, for various average densities $\rho = \langle N \rangle / M$ (determined by the value of the chemical potential μ) and several values of the inverse attraction strength parameter, $(\beta \varepsilon)^{-1}$. At low values of $(\beta \varepsilon)^{-1}$, as the average density is increased, the system exhibits a sequence of microphase separated structures. At very low densities, the system forms a gas phase. Increasing ρ, when the value of $(\beta \varepsilon)^{-1}$ is low enough, we see the particles are arranged into clusters of a characteristic size. Further increasing ρ, we observe stripe like patterns for $\rho \sigma^2 \sim 0.5$. At even higher densities, we observe a fluid containing 'bubbles', again with a characteristic size. Finally, for large ρ, the system is almost entirely full of particles, forming a dense liquid. Increasing $(\beta \varepsilon)^{-1}$ leads to the particles becoming less correlated, making it difficult to identify what microphase separation occurs, if any.

A. Heat Capacity

We calculate the heat capacity as the chemical potential μ is varied, in order to identity the regions of the phase diagram where the microphase separation occurs. At a phase transition, in the thermodynamic limit, there

is normally either a discontinuity or a divergence in the heat capacity. For finite size systems, these show up as peaks in the heat capacity. Recall also that a "bump" in the heat capacity was observed at the onset of microphase ordering in the simulations of Imperio and Reatto.[22] The heat capacity at constant volume can be obtained from the following derivative with respect to temperature,[27]

$$C_V = \left(\frac{\partial U}{\partial T} \right)_V, \tag{5}$$

where the internal energy $U = \langle E \rangle$. Alternatively, it can be calculated by measuring the energy fluctuations within the system,[28]

$$C_V = \frac{\langle E^2 \rangle - \langle E \rangle^2}{k_B T^2}. \tag{6}$$

A plot of the heat capacity of a system of size $40\sigma \times 40\sigma$ as a function of μ and for various values of $(\beta \varepsilon)^{-1}$ calculated via Eq. (6) is shown in Fig. 3. The heat capacity tends to zero when the system is completely empty or fully filled. This is as expected, since the system contains hardly any particles to give rise to energy fluctuations at lower values of the chemical potential, $\mu \to -\infty$, and in the opposite limit $\mu \to \infty$, the system is almost completely full of particles, so that the energy of the system, E, also does not fluctuate much in value.

For higher values of $(\beta \varepsilon)^{-1}$, we see in Fig. 3 that the heat capacity varies smoothly as μ is increased. However, for lower values of $(\beta \varepsilon)^{-1}$, we see four clear peaks in the heat capacity. These peaks correspond to changes in the structure of the fluid (see Fig. 2). Increasing μ, the first peak corresponds to a change from a low density gas to a clustered structure. The second peak corresponds to the change from the cluster to the stripe morphology. The third peak to the change from stripe to bubble and then the final fourth peak to the change from a liquid containing bubbles to a dense liquid without bubbles. As $(\beta \varepsilon)^{-1}$ is increased, these peaks become smaller in height, eventually being so small that they cannot be identified.

The overall energy fluctuations in the system also get larger as one increases $(\beta \varepsilon)^{-1}$. The large (peak) values of the heat capacity C_V corresponds to state points where there are large fluctuations in the energy of the system. Hence, the peak in C_V identifies state points where there are multiple types of typical configurations, each with different energy E.

The presence of these peaks in the heat capacity at state points where the fluid changes morphology naturally leads to the question: are these phase transitions, or just changes in the nature of the fluid correlations? For the low density and high density peak, this question is addressed in the following section.

B. Cluster Formation

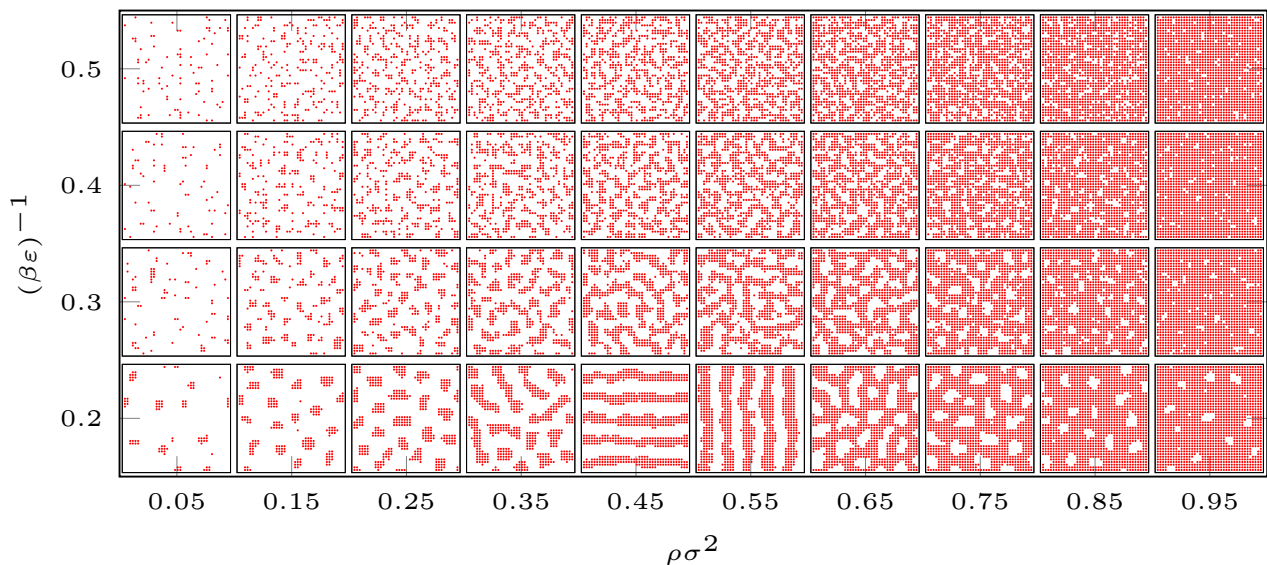To answer the question just posed above: no, the cluster formation is not a phase transition, it is a continuous

FIG. 2: Snapshots of typical configurations for a $40\sigma \times 40\sigma$ size system with $\beta A = 1.5$, $z_1 = 2$ and $z_2 = 0.2$, obtained from grand-canonical MC simulations for various values of the average density and varying values of $(\beta\varepsilon)^{-1}$.
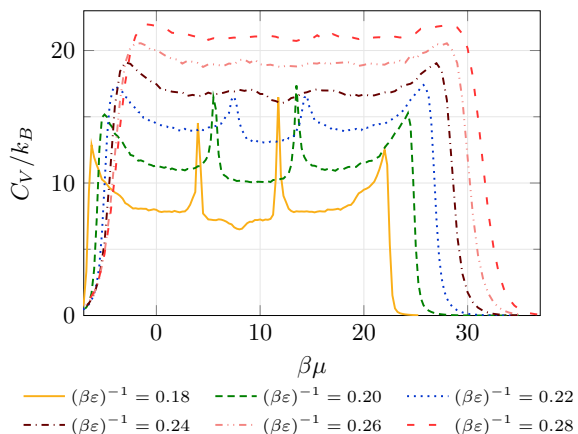

FIG. 3: Heat capacity verses chemical potential, μ, for different values of $(\beta\varepsilon)^{-1}$, obtained from Monte Carlo simulations for a $40\sigma \times 40\sigma$ size system with $\beta A = 1.5$, $z_1 = 2$ and $z_2 = 0.2$.

change analogous to micellisation in surfactants.

Recall that N is the total number of particles in the system, which changes over time in a grand canonical system. We denote the average total number of particles to be $\langle N \rangle$, and $\langle N_1 \rangle$ be the average number of particles that have no nearest or next nearest neighbours, which we refer to as "lone particles". We also calculate the ratio of lone particles to the total number of particles, $R = \langle N_1 \rangle / \langle N \rangle$, and how this quantity depends on the average density and chemical potential of the system.

In Fig. 4, we see that at lower values of chemical potential (i.e. low density), almost all the particles are lone

particles and so $R \approx 1$. This is because when we have a small overall number of particles in the system, we are likely to find them all to be alone. As the attraction strength is increased (i.e. as $(\beta\varepsilon)^{-1}$ is decreased), we see that the drop in value from $R \approx 1$ for low μ, to a value $R \ll 1$, becomes much steeper. For example, we see in Fig. 4(a) that when $(\beta\varepsilon)^{-1} = 0.2$, there is a very sudden drop in the value of R at $\beta\mu \approx -5$. This corresponds to the change in morphology of the system from being mostly full of lone particles to the cluster phase. However, as can be seen in Fig. 4(b), where we display the variation of R with the average density ρ on a logarithmic scale, we see that actually the change in R is continuous. The results in Fig. 4 were calculated for a $40\sigma \times 40\sigma$ size system, but these results do not change as the system size is increased (see also section III C below).

As we increase $(\beta\varepsilon)^{-1}$, we see the ratio of lone particles, R tends towards the value that one would obtain for a system with $\varepsilon = 0$ and $A = 0$, i.e. where the particles are randomly distributed in the system. This is due to the decrease in particle correlations at higher values of $(\beta\varepsilon)^{-1}$, where the structure is essentially that of a highly supercritical fluid. Since the change in the ratio of lone particles is smooth and continuous as we increase the chemical potential (density) of the system, it is clear that the transition that we observe is not a phase transition, instead it is a structural change in the fluid much like micellisation at the critical micelle concentration (CMC).[29]

Micellisation is the spontaneous self assembly of amphiphilic molecules in fluids. The forces that hold the amphiphiles together are generally weak, so that the structure within the micelles is fluid-like. Varying the solvent in which the micelles are suspended changes the inter-
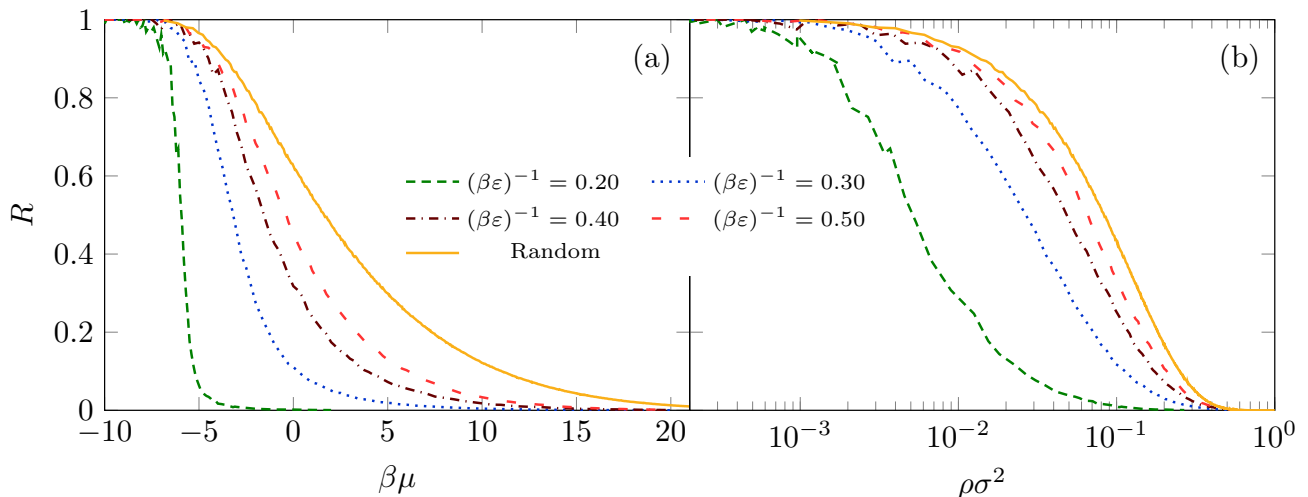
FIG. 4: Ratio of lone particles in the system, R, for different values of $(\beta\varepsilon)^{-1}$, as a function of: (a) the chemical potential and (b) the average density. The solid line labelled "Random" corresponds to the value of R for the entirely random uncorrelated configurations that the system with $\varepsilon = 0$ and $A = 0$ exhibits. All other results are for the system with $\beta A = 1.5$, $z_1 = 2$ and $z_2 = 0.2$.

actions and so determines the structure and size of the micelles.[29] The clusters we see are equivalent to spherical micelles, the bubbles are analogous to inverted micelles and the stripes to lamellar bilayer micelles. The similarities between the self-assembly of colloids and amphiphilic molecules have been observed in many experimental, simulation and theoretical studies.[7,18,22,30,31] Indeed, Ciach and co-workers were able to describe both the SALR colloidal system and amphiphilic systems using the same functional,[32] highlighting the many parallels between these systems.

Further support for the above conclusion about the nature of the structural changes in the system can be garnered from noting that the static structure factor $S(\mathbf{k})$ varies smoothly as μ is changed, taking the system from the low density gas state to the cluster morphology. $S(\mathbf{k})$ is a non-local quantity and so is sensitive to any onset of long range order, in contrast to R, which characterises only local (nearest neighbour) ordering. The static structure factor we compute is[1,21]

$$S(\mathbf{k}) = N^{-1} \langle \rho_{\mathbf{k}} \rho_{-\mathbf{k}} \rangle$$
$$= N^{-1} \left\langle \left(\sum_{j=1}^{N} \cos(\mathbf{k} \cdot \mathbf{r}_j) \right)^2 + \left(\sum_{j=1}^{N} \sin(\mathbf{k} \cdot \mathbf{r}_j) \right)^2 \right\rangle,$$
(7)

where $\rho_{\mathbf{k}} = \sum_{j=1}^{N} \exp(i\mathbf{k} \cdot \mathbf{r}_j)$, N is the number of particles in the system, and $\mathbf{r}_j$ is the position on the lattice of each of the particle. In our calculations presented here, we fix the wavevector $\mathbf{k} = (k, 0)$.

In Fig. 5(a) we display results for $S(k)$ for a range of state points where the cluster phase is observed, for fixed $(\beta\varepsilon)^{-1} = 0.18$. At lower densities (i.e. lower values

of the chemical potential μ), the peak in $S(k)$ is fairly broad with a maximum at $k\sigma = 0.15\pi \approx 0.47$, but for higher densities, the peak is sharper, with a maximum at $k\sigma = 0.2\pi \approx 0.63$. This is because at the higher densities the clusters interact more strongly with one another and the cluster-cluster correlations become significant. When $(\beta\varepsilon)^{-1} = 0.18$, the peak in the heat capacity for the gas to cluster transition occurs at $\beta\mu \approx -6$ [see Fig. 3]. Fig. 5(b) shows that as μ is varied around this value, $S(k)$ varies smoothly, indicating there is no phase transition. This can also be seen from the plot in Fig. 6, where we plot $S(k)$ for fixed values of k as the chemical potential μ is varied, going from the low density gas state to deep in the region of the phase diagram where the cluster morphology occurs. One further interesting feature of the results in Fig. 6 is that in the cluster phase, the value of $S(k\sigma = \pi/4)$ is almost constant.

We also calculate the histogram of the probability of finding a given instantaneous density $\rho = N/M$ (not displayed). This has a single peak for all values of the chemical potential $\beta\mu \approx -6$, where the heat capacity peak occurs. This is in contrast to the three dimensional system considered in Ref. 7, where a double peaked histogram is observed at the onset of cluster formation.

C. Changing Box Size

Our MC simulations are performed in a finite size box with periodic boundary conditions to approximate an infinite system. However, for some of the transitions, it turns out that the box size is significant in determining the properties of the system. In Fig. 7 we plot the heat capacity for $(\beta\varepsilon)^{-1} = 0.18$, calculated for simulations in

FIG. 6: The static structure factor $S(k)$ for a range of different wavevectors k, as the chemical potential μ is varied, for fixed attraction strength $(\beta\varepsilon)^{-1} = 0.18$.
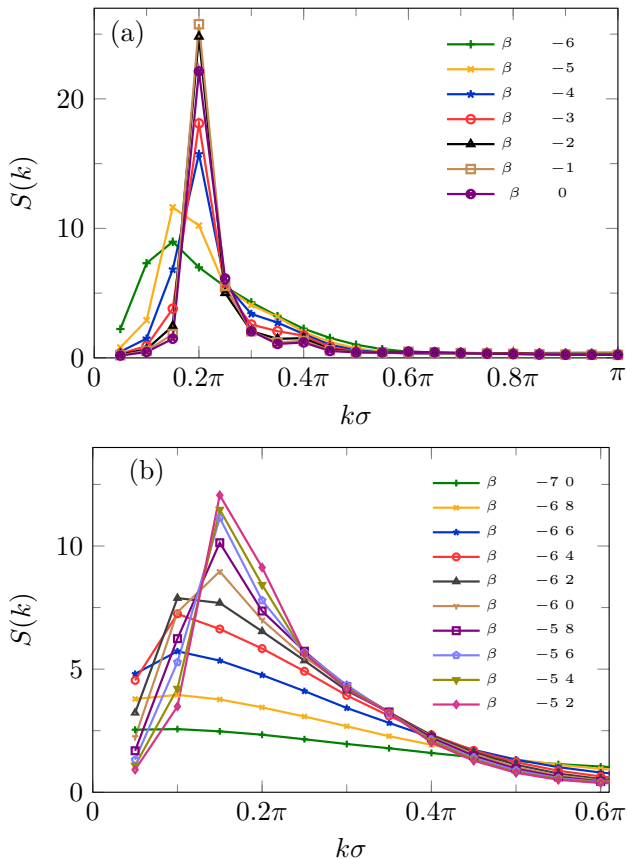

FIG. 5: In (a) we display the static structure factor $S(k)$ for fixed $(\beta\varepsilon)^{-1} = 0.18$ and for a range of different values of the chemical potential μ where the cluster morphology is observed. The gas to cluster morphology change occurs at $\beta\mu \approx -6$, where there is a peak in the heat capacity (c.f. Fig. 3). In (b) we display $S(k)$ over a smaller range of values of μ, going from the gas to the cluster morphology. We see that $S(k)$ varies smoothly as μ is varied – see also Fig. 6.

a box of size $40\sigma \times 40\sigma$ and compare with results for a larger box of size $60\sigma \times 60\sigma$.

In Fig. 7, we do not observe any effect of the finite box size on the value of the heat capacity at the peaks corresponding to the gas to cluster transition and also the bubbles to liquid transition. This confirms the conclusion in the previous section that this transition is akin to micellisation, and that there are no discernable effects in the above results due to a finite system size. However, for the heat capacity peaks corresponding to the cluster to stripe and the stripe to bubble transitions, in Fig. 7 we do see significant finite size effects. These peaks shift and become sharper and higher as the system size is increased. This might be seen as indicative that these are second order phase transitions, with a heat capacity divergence in the thermodynamic limit. However, recall that at a phase transition, in a small finite size simulation box the system fluctuates between the two phases. This leads to a double peak in the density histogram at

FIG. 7: The heat capacity versus chemical potential μ, for two different box sizes for $(\beta\varepsilon)^{-1} = 0.18$ [c.f. Fig. 3].

that state point (or indeed the histogram of any other quantity that is a suitable order parameter for the transition). However, as can be seen in Fig. 8, where we display the density histogram calculated at the value of μ corresponding to the peak in the heat capacity, there is a single peak (the corresponding chemical potential values are $\beta\mu \approx 4.0$ and $\beta\mu \approx 3.1$ for $L = 40\sigma$ and $L = 60\sigma$, respectively). We obtain very similar distributions for state points either side of where the heat capacity peak occurs. An alternative order parameter that is more sensitive to periodic ordering is the density Fourier mode amplitude,

$$|\rho_{\mathbf{k}}| = \sqrt{\left(\sum_{j=1}^{N} \cos(\mathbf{k} \cdot \mathbf{r}_j)\right)^2 + \left(\sum_{j=1}^{N} \sin(\mathbf{k} \cdot \mathbf{r}_j)\right)^2}. \quad (8)$$

FIG. 8: Probability of finding a certain instantaneous density $\rho = N/M$ calculated at the cluster to stripe transition (i.e. at the second peak in the heat capacity) for two different box size for $(\beta\varepsilon)^{-1} = 0.18$.

FIG. 9: Probability distribution for the density Fourier mode amplitude $|\rho_{\mathbf{k}}|$, with $k\sigma = 0.2\pi$, calculated at the cluster to stripe transition (i.e. at the second peak in the heat capacity) for two different box sizes L and for $(\beta\varepsilon)^{-1} = 0.18$.

In Fig. 9 we display the histogram of $|\rho_{\mathbf{k}}|$ for the wavevector $\mathbf{k} = (k_p, 0)$, where $k_p\sigma = 0.2\pi$, which is the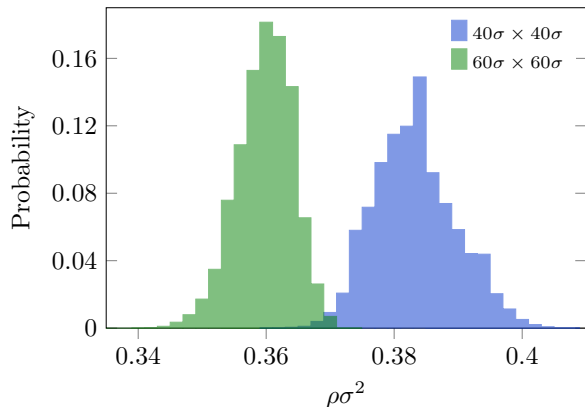 value where there is a peak in $S(k)$. This order parameter histogram also has a single peak for values of μ where the heat capacity exhibits a peak.

From the fact that there is only a single peak in Figs. 8 and 9, we infer that the transition from the cluster to striped state is simply a change in morphology, much like the micellisation process. We infer the same for the transition from the stripe to the bubble morphology. For low values of $(\beta\varepsilon)^{-1}$, we believe that the large heat capacity peak at the transition to the stripe phase and the strong finite-size effects are due to the fact that the stripes that are formed span the simulation box (see Fig. 2). The finite size box stabilises the stripes, damping some of the long wavelength fluctuations.

IV. LATTICE DFT

We now present results for the structure and thermodynamics of the fluid, which are calculated using density functional theory, and compare with the MC simulation results. The mean-field DFT that we use is a generalisation of the theory presented in Ref. 25 (see also references therein for other applications of the theory). The thermodynamic grand potential is approximated by

$$\Omega = k_B T \sum_{i=1}^{M} \left[\rho_i \ln(\rho_i) + (1 - \rho_i)\ln(1 - \rho_i)\right]$$
$$+ \frac{1}{2}\sum_{i,j} V_{i,j}\rho_i\rho_j + \sum_{i=1}^{M}(\Phi_i - \mu)\rho_i. \quad (9)$$

The equilibrium density profile is that which minimises Ω, i.e. is the solution of

$$\frac{\partial\Omega}{\partial\rho_i} = 0, \text{ for all } i. \quad (10)$$

Thus, from Eqs. (9) and (10) we obtain

$$\rho_i = (1 - \rho_i)\exp\left[\beta\left(-\sum_j V_{i,j}\rho_j - \Phi_i + \mu\right)\right]. \quad (11)$$

This set of coupled equations are solved by Picard iteration.[25] In order to make sure ρ_i does not fall outside the interval $(0, 1)$ during the iteration process, we introduce a mixing parameter, α. The idea is that after each iteration, we mix the new density value with the previous one,

$$\rho_i = \alpha\rho_i^{\text{new}} + (1 - \alpha)\rho_i^{\text{old}}. \quad (12)$$

The mixing parameter α typically takes a value in the range $(0.01, 0.2)$. Too large a value of α leads to instabilities in the iteration, whilst if α is too small, it leads to slow convergence.

DFT results and comparison with MC

In Fig. 10, we display examples of density profiles calculated using the lattice DFT for various values of the attraction strength parameter $(\beta\varepsilon)^{-1}$. These are obtained by initiating the Picard iteration with a flat density profile, to which is added a small amplitude random value at each lattice site. The density profiles show the same sequence of structures as observed in Fig. 2 from the MC simulation, namely uniform, cluster, stripe, bubble

FIG. 10: A series of density profiles for varying values of $(\beta\varepsilon)^{-1}$ calculated using the lattice DFT for a $40\sigma \times 40\sigma$ size system with random initial conditions, for $\beta A = 1.5$, $z_1 = 2$ and $z_2 = 0.2$ [c.f. Fig. 2]. The colours associated with each density value can be deduced from the top row of profiles, which are for $(\beta\varepsilon)^{-1} = 0.5$.
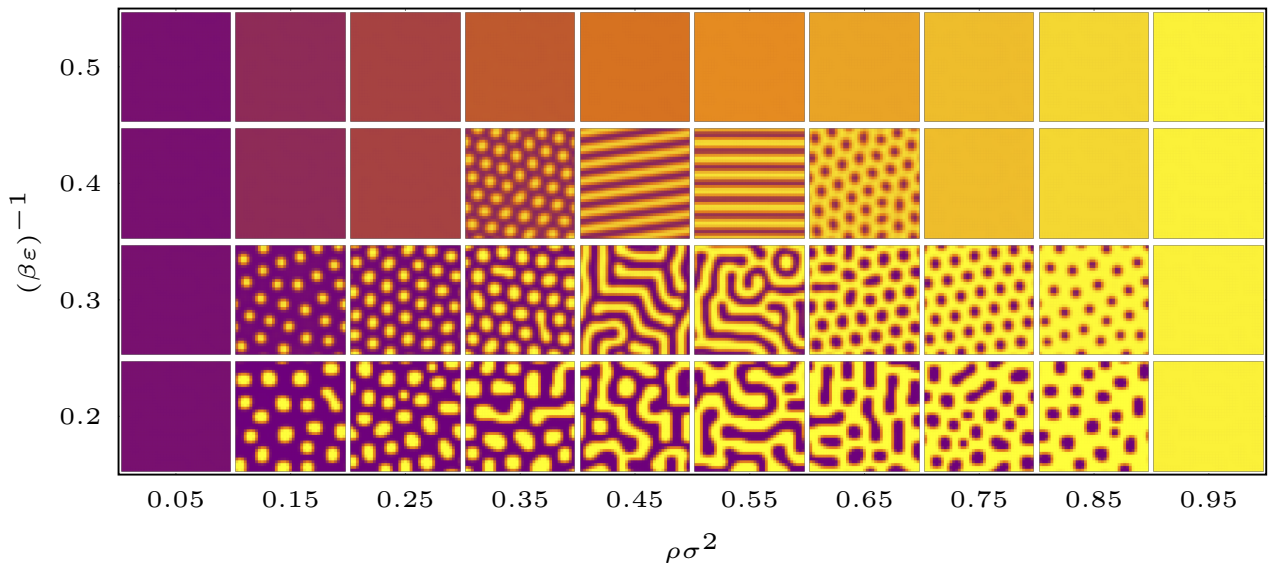
and uniform as the chemical potential (density) is increased. The agreement between Fig. 10 and Fig. 2 is rather good. Within the DFT each of these different structures correspond to different solution branches of the grand potential. The global minimum structure for a given state point contains no defects. Thus, in Fig. 10 the vast majority of the structures displayed are not global minima of Ω. To calculate the phase diagram, we calculate the free energy for defect-free structures, which are obtained by initiating the Picard iteration from profiles with the required structure, rather than from random initial conditions. As μ is increased, there are points where these branches cross. At these points the solutions on the different branches have the same μ, T and pressure $p = -\Omega/V$, where $V = M\sigma^2$ is the area of the 2D system. Thus, the (incorrect) prediction from the mean-field DFT is that there are first order phase transitions between all the different structures.

We calculate the lines of thermodynamic coexistence in the phase diagram predicted by the DFT by selecting an initial lattice with a certain microphase separation and then change the chemical potential μ and follow that particular branch of solutions. For example, to find the coexistence curve for the gas to cluster transition, we start the DFT iteration with a uniform gas profile and increase μ with the new guess being the minimised density profile from the previous value of μ. While doing this we record the grand potential Ω. Also, we start with an initial density profile corresponding to the cluster structure at a higher value of μ and then decrease μ following this branch of solutions. Coexistence is found when the pressure, temperature and chemical potential of the two

structures are equal. The lines of coexistence define the boundaries in the phase diagram of where the different microphase separated structures occur.
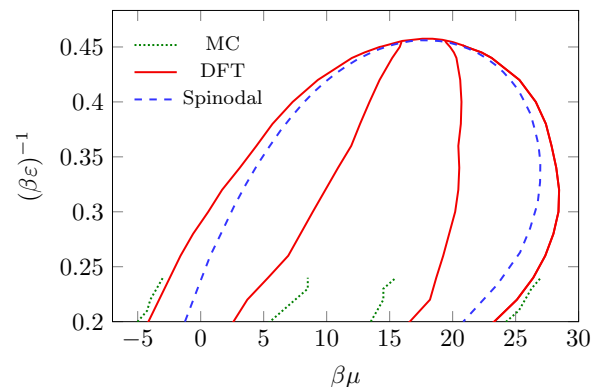
FIG. 11: Phase diagram showing the instability threshold (spinodal, displayed as the blue dashed line) and the coexistence lines (red solid lines) obtained from DFT for varying values of the chemical potential μ and attraction strength $(\beta\varepsilon)^{-1}$. The location of the peaks in the heat capacity determined from the MC simulations for a $40\sigma \times 40\sigma$ system are also shown, as the green dotted line. Note that these lines terminate where the peaks disappear (c.f. Fig. 2).

As shown in Fig. 11, we see that at the highest values of $(\beta\varepsilon)^{-1}$ (weak attraction) there is no microphase separation and the system exhibits a single uniform fluid phase. The DFT predicts microphase separation for values of $(\beta\varepsilon)^{-1} < 0.45$. For the higher values in this range, e.g. $(\beta\varepsilon)^{-1} = 0.4$, the heat capacity from MC simulations

in Fig. 3 has no discernible peaks. Nonetheless, comparing Fig. 10 and Fig. 2, we see that the DFT is correctly predicting the structures formed, it is solely failing to describe the nature of the transition to the modulated structures.

We also see a general shift of the occurrence of microphase ordering to higher values of μ as we increase $(\beta\varepsilon)^{-1}$. In Fig. 11 we also display as green dotted lines the locations of the peaks in the heat capacity, from the MC simulations for a system of size $40\sigma \times 40\sigma$. We see that these peaks lie close to the DFT coexistence lines for the gas to cluster transition and also the bubble to liquid transition. However, for the transitions to the stripe state, they are further away. We should emphasise, however, that these are subject to significant finite size effects. For a larger system, these are much closer to the DFT coexistence line.

The linear instability threshold line in Fig. 11 is calculated numerically by starting from an initial density profile with the given average value of the density, but with small amplitude random fluctuations. We then determine whether the fluctuations grow over time as we iterate. The boundary of the region where they do grow is referred to as the spinodal in Fig. 11. We can also see that the instability line is completely inside the coexistence line. An alternative (but entirely equivalent) way to calculate the spinodal is to determine when the uniform density solution to Eq. (9) ceases to be a minimum. Consider a small amplitude harmonic density perturbation of the form

$$\rho_i = \rho + ae^{i\mathbf{k}\cdot\mathbf{r}_i}, \tag{13}$$

where the amplitude a is a small parameter, $\mathbf{r}_i$ is the location of lattice site i and $\mathbf{k}$ is any wavevector that is commensurate with the lattice. Substituting Eq. (13) into Eq (9) and then requiring that there is no solution except when $a = 0$, is equivalent to the requirement that

$$\frac{1}{1-\rho} + \rho\beta V_d(\mathbf{k}) > 0, \tag{14}$$

where $V_d(\mathbf{k}) = \sum_j V_{i,j}e^{-i\mathbf{k}\cdot\mathbf{r}_{i,j}}$ is the discrete Fourier sum of the potential, where $\mathbf{r}_{i,j} = \mathbf{r}_i - \mathbf{r}_j$. The quantity on the left hand side of Eq. (14) is equal to $1/S_{DFT}(\mathbf{k})$, where $S_{DFT}(\mathbf{k})$ is the static structure factor predicted by the DFT. Within the spinodal displayed in Fig. 11, Eq. (14) is no longer true for all $\mathbf{k}$ and thus the uniform density profile is no longer a minimum of the free energy.[24]

In Fig. 12 we compare how the average density varies with chemical potential in the MC simulations with the results from DFT. We see that the MC simulation results show a smooth increase in the density. However, for sufficiently low values of $(\beta\varepsilon)^{-1}$, the DFT gives jumps in the density as we increase μ. The jumps are plotted as dots in Fig. 12, which corresponds to the values of μ where microphase separation occurs. The magnitude of the jumps decreases as we increase $(\beta\varepsilon)^{-1}$. The jumps in the DFT occur because of various local minima in the free energy.
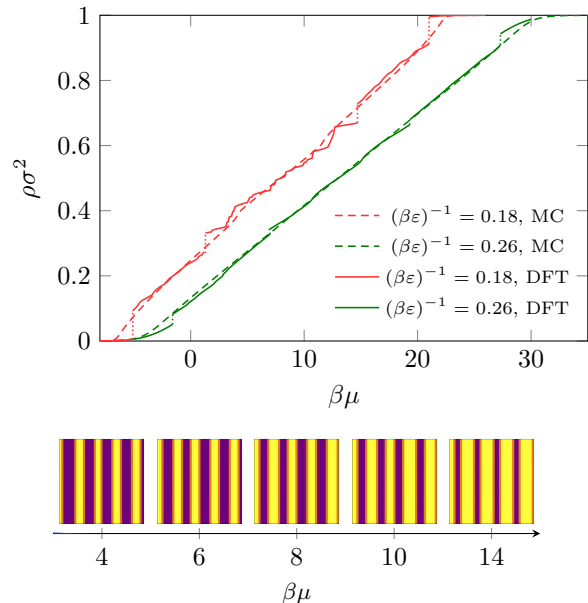
FIG. 12: Top: a comparison of the average density as a function of μ for two different values of $(\beta\varepsilon)^{-1}$ from the MC simulations (dashed lines) and DFT (solid lines). The dotted line in the DFT curves show the jumps at which the transitions between the different morphologies occurs. Bottom: DFT density profiles showing the discontinuous changes in the stripes as we vary μ for fixed $(\beta\varepsilon)^{-1} = 0.18$, resulting in the non-smooth curves in the density plot above.

Hence, the DFT has a tendency to stick to the initial density profile (local minimum) that we start from. Thus, the initial density profile is important for determining if the grand potential minimum that the iteration goes to is actually the global minimum. Different initial density profiles give us different local minima, which also depends on the box size, as expected. The DFT results are closer to the MC simulation results at higher values of $(\beta\varepsilon)^{-1}$ where there are more fluctuations in the system and the structural changes that occur in the system are smoother.

For example, when $(\beta\varepsilon)^{-1} = 0.18$ (typical of low values of $(\beta\varepsilon)^{-1}$), the DFT exhibits many discontinuities as we increase the chemical potential. This can be easily noticed in the middle portion of the curve in Fig. 12 which corresponds to the stripe region. This is due to discontinuous changes in the width of the stripes that arise as we change the chemical potential. This is illustrated in the lower plots in Fig. 12, where we see that the width of individual stripes varies with changing chemical potential - i.e. not all stripes in Fig. 12 have the same width. This confirms that the pattern formed is not necessarily the global equilibrium, since we expect the width of all the individual stripes to be identical at a global minimum.

Plotting the value of $(\beta\varepsilon)^{-1}$ at which the transitions occur as a function of density, we see that in this representation the phase diagram is symmetric around $\rho\sigma^2 = 0.5$ (see Fig. 13). The instability line is fully within the re-
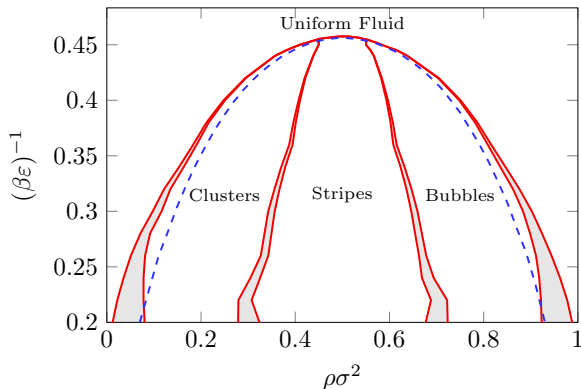
FIG. 13: Phase diagram showing the instability line (blue) and the coexistence lines (red) from DFT for varying values of the density ρ and attraction strength ε, for fixed $\beta A = 1.5$, $z_1 = 2$ and $z_2 = 0.2$.

gion of the phase diagram where the uniform liquid is metastable. The shaded regions are the regions of coexistence between the two phases. We also see that the density range over which there is coexistence decreases as we increase $(\beta\varepsilon)^{-1}$.

V. CONTINUUM DFT APPROXIMATION

We now approximate the discrete lattice model by treating it with a continuum DFT, that enables a more straightforward calculation of quantities such as the linear instability threshold (spinodal) and other related quantities. This mapping from the lattice to a continuum assumes that the density profile ρ_i varies slowly enough that we can treat it as a discretised representation of a continuous profile $\rho(\mathbf{r})$. This also enables us to convert the sums over lattice sites into integrals. Hence, the Helmholtz free energy $F = \Omega + \mu\langle N\rangle$ [cf. Eq. (9)], can be written as the following functional:

$$F = \int f(\rho(\mathbf{r}))\,\mathrm{d}\mathbf{r} + \frac{1}{2}\iint \rho(\mathbf{r})\rho(\mathbf{r}')V(|\mathbf{r}-\mathbf{r}'|)\,\mathrm{d}\mathbf{r}\,\mathrm{d}\mathbf{r}'$$
$$+ \int \rho(\mathbf{r})\Phi(\mathbf{r})\,\mathrm{d}\mathbf{r} \qquad (15)$$

where $V(r)$ is the pair potential in Eq. (3), $\Phi(\mathbf{r})$ is the external potential and f is a local free energy per unit area given by

$$f(\rho) = k_B T\left[\rho\ln(\rho) + (1-\rho)\ln(1-\rho)\right] - \frac{\chi}{2}\rho^2. \quad (16)$$

The first term is the free energy for a non-interacting ($\varepsilon = A = 0$) lattice gas. The second term involving the parameter χ is a term to correct for the effect of the mapping from the lattice to the continuum, so that the continuum model gives the same free energy for the uniform fluid as the lattice model. The parameter χ is the following integrated difference between the continuum pair

potential and the lattice potential:

$$\chi = 2\pi \int_\sigma^{r_c} rV(r)\,\mathrm{d}r - \sum_{<i,j>} V_{i,j}. \qquad (17)$$

The reason for mapping to a continuum model is that the following linear stability analysis is made somewhat more simple. The aim of the linear stability analysis is to determine where in the phase diagram the uniform fluid state becomes unstable, i.e. we locate the region of the phase diagram in which the microphase ordering occurs.

Consider a uniform fluid with density ρ_0. We wish to know whether any small amplitude density modulation will grow over time (fluid is unstable) or whether the amplitude will decrease (fluid is stable). Specifically we consider a density fluctuation of the form [c.f. Eq. 13]

$$\rho = \rho_0 + \delta\rho(\mathbf{r}, t)$$
$$= \rho_0 + \xi e^{i\mathbf{k}\cdot\mathbf{r}+\omega t}, \qquad (18)$$

where ξ is the initial amplitude of the sinusoidal perturbation that has wavenumber $\mathbf{k}$. The growth/decay rate of this mode is given by the dispersion relation $\omega = \omega(k)$, where $k = |\mathbf{k}|$.[33]

To determine the time evolution of this non-equilibrium density profile, we require a theory for the dynamics of the colloids. This is supplied by dynamical density functional theory (DDFT), which shows that for Brownian colloidal particles the time evolution of $\rho(\mathbf{r}, t)$ is governed by[1,33,34]

$$\frac{\partial\rho}{\partial t} = D\nabla \cdot \left[\rho\nabla\frac{\delta\beta F}{\delta\rho}\right], \qquad (19)$$

where D is the diffusion coefficient of the colloids. Note that for an equilibrium fluid, the chemical potential[1,35,36]

$$\mu = \frac{\delta F}{\delta\rho} \qquad (20)$$

is a constant. Thus, in Eq. (19), it is gradients in the chemical potential of the non-equilibrium fluid that drives the dynamics. Substituting Eq. (18) into Eq. (19) together with Eq. (15) with the external potential $\Phi = 0$, and then linearising in $\delta\rho$, we obtain the following expression for the dispersion relation[33] [c.f. Eq. (14)]

$$\omega = -Dk^2\left(\frac{1}{1-\rho_0} - \beta\chi\rho_0 + \beta\rho_0\hat{V}(k)\right), \qquad (21)$$

where $\hat{V}(k)$ is the 2D Fourier Transform of the pair potential

$$\hat{V}(k) = 2\pi \int_0^\infty rV(r)J_0(kr)\,\mathrm{d}r, \qquad (22)$$

where $J_0(x)$ is the Bessel function of order 0. In Fig. 14 we display the dispersion relation for the uniform fluid with density $\rho\sigma^2 = 0.5$, for various values of ε.
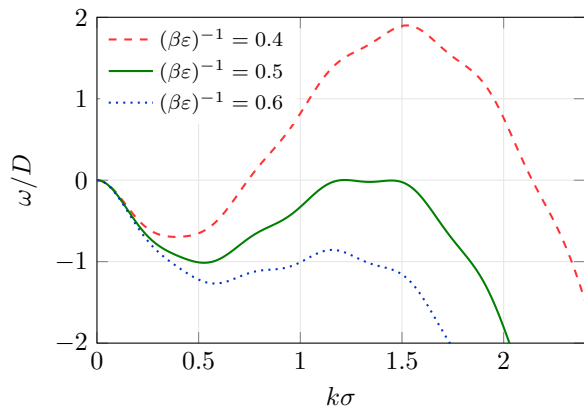
FIG. 14: The dispersion relation (21) for varying attraction strength ε, for the uniform fluid with density $\rho\sigma^2 = 0.5$, for fixed $\beta A = 1.5$, $z_1 = 2$ and $z_2 = 0.2$.

From the dispersion relation, we can find the linear instability threshold line. Since we know that the system becomes unstable when $\omega > 0$, the instability line is calculated for values of ε and ρ_0, where $\omega(k_c) = 0$, where k_c is the value at which $\omega(k)$ is a maximum, i.e.

$$\frac{\mathrm{d}\omega(k)}{\mathrm{d}k}\bigg|_{k=k_c} = 0. \tag{23}$$

The linear instability line is thus easily obtained from the dispersion relation and is displayed in Fig. 15. In this figure, we also display the linear instability line for the original lattice DFT model.
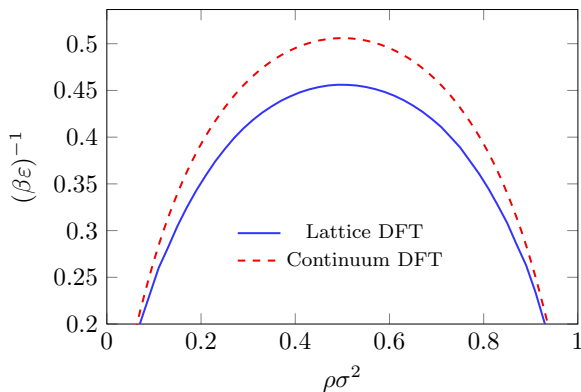

FIG. 15: Phase diagram showing the linear instability threshold line for the lattice DFT (blue solid line) and also the instability line for the continuum DFT (red dashed line), calculated from dispersion relation in Eq. (21).

Comparing the two instability lines in Fig. 15 shows that the maximum value of $(\beta\varepsilon)^{-1}$ where the system is linearly unstable is predicted to be a little higher in the continuum theory, compared to the lattice model. Comparing with Fig. 2 and Fig. 10, we see that this

simple calculation does indeed identify the region of the phase diagram where microphase separation is observed. Of course, it does not specify which structures (cluster, stripe or bubble) are formed, but it does allow one to narrow down to the relevant region of the phase diagram.

We find the above analysis rather instructive: mapping from a lattice to continuum theory or vice-versa is a "trick" that is often performed to aid the analysis of a system. This procedure is clearly an approximation, but the fact that the two curves in Fig. 15 are reasonably close to one another gives confidence that in the present situation the mapping is justified.

VI. CONCLUSION

In this paper we have studied a lattice model for 2D colloidal fluids where the colloids have attractive interactions at short separations, but repel at longer range. We model this by using a double-Yukawa pair potential between the particles. This SALR system self assembles to form different microphase separated structures. Using MC computer simulations and by calculating the heat capacity of the system as the chemical potential μ and the attraction strength coefficient ε are varied, we determine where in the phase diagram the different morphology changes occur. At lower values of $(\beta\varepsilon)^{-1}$, the heat capacity exhibits peaks at the transitions between the different structures. The height of the peaks decrease as we increased $(\beta\varepsilon)^{-1}$, eventually disappearing. The peak at the transition from the gas to the cluster state and also for the bubble to liquid shows no system size dependence for systems greater than or equal to $40\sigma \times 40\sigma$ in size. However, the peaks for the transitions to the stripe phase do change with system size, for the system sizes we were able to consider. By calculating how the number of lone particles and the static structure factor varies through the transition between the gas and the cluster phase, we conclude that this transition is a structural transition entirely akin to micellisation. The transition from the cluster to the stripe phase is very similar, except here occurring on a larger scale, by the gathering together of clusters to form stripes. This behaviour is also observed in living polymerisation, where a peak in the heat capacity is also observed.[37–39]

Due to the fact that the pair potential (2) between the particles is fairly long ranged, the MC simulations can be computationally expensive. Recall that we cut-off our slowly decaying potential at a range of $r_c = 16\sigma$, which is much longer ranged than the potentials considered e.g. in Refs. 10–14. We only implemented the simple Metropolis MC algorithm, so correctly sampling for system sizes greater than $60\sigma \times 60\sigma$ and for many state points was not feasible. To simulate efficiently for larger systems, a more sophisticated MC incorporating e.g. cluster moves is required. This simple MC also limited what temperatures (i.e. values of $(\beta\varepsilon)^{-1}$) we could go down to. For $(\beta\varepsilon)^{-1} = 0.18$ we are confident that our MC simulations

are correctly sampling the system. However, for lower temperatures, the algorithm struggles to sample a representative set of states in the time available. The low temperature properties of the model are interesting as it may be the case that at very low temperatures the structural transitions we observe become genuine phase transitions. It is certainly the case that other lattice models with competing interactions[11–14] do exhibit phase transitions at low temperatures. We leave investigating this aspect to future work.

We also used a simple lattice DFT to calculate density profiles for the system. Comparing Figs. 2 and 10, the agreement between simulation and the mean-field DFT is rather good. The pair potential (2), with the parameter values that we use, is fairly long ranged and slowly varying – see Fig. 1. In the case of purely attractive systems, when the pair potentials are long ranged and slowly varying (the classic mean-field situation) then one would not be surprised to find that mean-field DFT is accurate. However, given that the present system exhibits microphase ordering and is strongly fluctuating, it was not a-priori clear that the agreement between the DFT and the MC is as good as it is.

We also used the DFT to calculate the phase diagram and found that the heat capacity peaks in the MC simulations are close to the transition lines predicted by the DFT for the gas to cluster transition and the bubble to liquid transition. For the cluster to stripe and stripe to bubble transitions, they are somewhat further away.

One aspect of the DFT is that at lower values of $(\beta\varepsilon)^{-1}$, the model exhibits many local free energy minima. This means that to use the DFT to calculate the phase diagram one needs to ensure one has a good choice of initial density profile. Starting from a density profile that is not good approximation, the iteration can go to a local minimum with a free energy value above that of the global minimum. Such behaviour is often observed in pattern forming systems. Thus, great care is required to determine the system sizes in which the system arranges in a state that is close in free energy value to the global minimum value.

Mapping the lattice model onto a continuum DFT yields a theory from which determining the linear instability threshold line using the dispersion relation is straightforward, enabling us to easily and rapidly determine the range of parameter values where the microphase ordering occurs. This provides a useful starting point if future analysis of the behaviour of systems with different pair potential parameter values is required.

[1] J.-P. Hansen and I. R. McDonald, *Theory of Simple Liquids with Applications to Soft Matter*, 4th ed. (Academic Press, 2013).

[2] A. I. Campbell, V. J. Anderson, J. S. van Duijneveldt, and P. Bartlett, Phys. Rev. Lett. **94**, 208301 (2005).

[3] A. Stradner, H. Sedgwick, F. Cardinaux, W. C. K. Poon, S. U. Egelhaaf, and P. Schurtenberger, Letters to Nature **432**, 492 (2004).

[4] D. Pini, G. Jialin, A. Parola, and L. Reatto, Chem. Phys. Lett. **327**, 209 (2000).

[5] D. Pini, A. Parola, and L. Reatto, J. Phys.: Condens. Matter **18**, S2305 (2006).

[6] A. J. Archer, D. Pini, R. Evans, and L. Reatto, J. Chem. Phys. **126**, 1 (2007).

[7] A. J. Archer and N. B. Wilding, Phys. Rev. E **76**, 031501 (2007).

[8] M. B. Sweatman, R. Fartaria, and L. Lue, J. Chem. Phys. **140**, 124508 (2014).

[9] J.-M. Bomont, J.-L. Bretonnet, D. Costa, and J.-P. Hansen, J. Chem. Phys. **137**, 011101 (2012).

[10] J. Pekalski, A. Ciach, and N. G. Almarza, J. Chem. Phys. **138**, 144903 (2013).

[11] J. Pekalski, A. Ciach, and N. G. Almarza, J. Chem. Phys. **140**, 114701 (2014).

[12] N. G. Almarza, J. Pekalski, and A. Ciach, J. Chem. Phys. **140**, 164708 (2014).

[13] W. Selke and M. Fisher, Z. Physik B **40**, 71 (1980).

[14] D. Landau and K. Binder, Phys. Rev. B **31**, 5946 (1985).

[15] D. Andelman, F. Brochard-Wyart, and J.-F. Joanny, J. Chem. Phys **86**, 3673 (1986).

[16] Z. Nussinov, J. Rudnick, S. A. Kivelson, and L. N. Chayes, Phys. Rev. Lett. **83**, 472 (1999).

[17] C. B. Muratov, Phys. Rev. E **66**, 066108 (2002).

[18] M. Tarzia and A. Coniglio, Phys. Rev. E **75**, 011410 (2007).

[19] R. P. Sear and W. M. Gelbart, J. Chem. Phys. **110**, 9 (1999).

[20] R. P. Sear, S.-W. Chung, G. Markovich, W. M. Gelbart, and J. R. Heath, Phys. Rev. E **59**, R6255 (1999).

[21] A. Imperio and L. Reatto, J. Phys.: Condens. Matter **16**, S3769 (2004).

[22] A. Imperio and L. Reatto, J. Chem. Phys. **124**, 164712 (2006).

[23] A. Imperio and L. Reatto, Phys. Rev. E **76**, 040402(R) (2007).

[24] A. J. Archer, Phys. Rev. E **78**, 031402 (2008).

[25] A. P. Hughes, A. J. Archer, and U. Thiele, Am. J. Phys. **82**, 1119 (2014).

[26] D. P. Landau and K. Binder, *A guide to Monte Carlo simulations in statistical physics* (Cambridge university press, 2009).

[27] R. Bowley and M. Sanchez, *Introductory Statistical Mechanics*, 2nd ed. (Oxford Univeristy Press, 1999).

[28] D. Chandler, *Introduction to Modern Statistical Mechanics* (Oxford Univeristy Press, 1987).

[29] J. N. Israelachvili, *Intermolecular and Surface Forces*, 3rd ed. (Academic Press, 2011).

[30] A. I. Campbell, V. J. Anderson, J. S. van Duijneveldt, and P. Bartlett, Phys. Rev. Lett. **16**, 208301 (2005).

[31] D. E. Masri, T. Vissers, S. Badaire, J. C. P. Stiefelhagen, H. R. Vutukuri, P. Helfferich, T. H. Zhang, W. K. Kegel, A. Imhof, and A. van Blaaderen, Soft Matter **8**, 2979 (2012).

[32] A. Ciach, J. Pekalski, and W. T. Gozdz, Soft Matter **9**, 6301 (2013).

[33] A. J. Archer and R. Evans, J. Chem. Phys. **121**, 4246 (2004).

[34] U. M. B. Marconi and P. Tarazona, J. Chem. Phys. **110**, 8032 (1999).

[35] R. Evans, Adv. in Phys. **28**, 2 (1979).

[36] R. Evans, in *Fundamentals of Inhomogeneous Fluids*, edited by D. Henderson (Marcel Dekker, New York, 1992) Chap. 3, pp. 85–176.

[37] S. C. Greer, J. Phys. Chem. B **102**, 5413 (1998).

[38] J. Dudowicz, K. F. Freed, and J. F. Douglas, J. Chem. Phys. **111**, 7116 (1999).

[39] K. Van Workum and J. F. Douglas, Phys. Rev. E **71**, 031502 (2005).

Chapter 9

Final Remarks

Two different statistical mechanics based models for simulating the evaporation of nanoparticle suspensions have been developed and the simulation results have been compared. Both models are relatively simple in that they are lattice based and the code to simulate only uses basic mathematics. The two models take different approaches: MC works with the coarse grained particle configurations on the lattice, DDFT works with ensemble average density profiles. The power of DDFT is that thermodynamic quantities like surface tensions and the phase diagram can be obtained easily. When we compare quantities like the contact angle between the two approaches, we see good agreement at the temperatures of interest.

Treating the fluid via a simple Ising model with nearest neighbour interactions usually leads to blocky droplets but our choice of coefficients in the interaction matrix for neighbouring sites in the Hamiltonian minimises the effect of the grid and leads to hemispherical droplets for both the MC and DDFT models. This is an important aspect of our model and we believe future researchers may want to adopt this approach.

Both models used a similar methodology to model surface roughness. Roughening the surface by making the surface height a random variable on the scale of the grid does not work well because the scale is too coarse. However, we found that changing the mobility matrix in the layer of lattice sites at the surface to prevent fluid motion parallel to the surface in the

lattice sites touching the surface gives a good approximation for the effect of rough surfaces on droplet motion. The choice of the parameter v in Eq. (7.5.3) determines the receding contact angle. This parameter can be chosen to match experimental results.

The MC simulations were able to run for systems sizes up to $256 \times 256 \times 128$, taking normally only several hours to a few days. Our MC model is versatile enough to allow multiple kinds of surface and dynamical rules to be added to change the behaviour of the system so many more effects related to the size/shape of the nanoparticles and surface structure/chemistry could be added if desired. Currently there are no hydrodynamic effects in the MC model so it is desirable for this aspect to be addressed.

As noted, the advantage of the DDFT is that within this theory thermodynamic quantities like the free energy can be calculated. However, the DDFT used also neglects the Hydrodynamics. This could be remedied by using the DDFT of Refs. [79, 80] that incorporates the hydrodynamic interactions between the colloids, for describing the nanoparticles and the DDFT of Refs. [36, 6] for the solvent. However, one striking result of our work is that we observe what appears to be a coffee stain effect, a phenomena previously thought to be dependent on the advective hydrodynamics within the droplet, even though this in not in our theory.

Another possible future development is to extent the DDFT simulations into 3D space. For the 3D version of Fig. 7.14 we would expect concentric circles of deposit on the surface; it would be nice to confirm this with simulation results.

Bibliography

[1] M. Plischke and B. Bergersen, *Equilibrium Statistical Physics.* World Scientific, 2006.

[2] R. Evans, "Density functionals in the theory of nonuniform fluids," in *Fundamentals of Inhomogeneous Fluids* (D. Henderson, ed.), ch. 3, pp. 85–176, New York: Marcel Dekker, 1992.

[3] J.-P. Hansen and I. R. McDonald, *Theory of Simple Liquids: With Applications to Soft Matter.* Academic Press, 2013.

[4] M. Newman and G. Barkema, *Monte Carlo Methods in Statistical Physics chapter 1-4.* Oxford University Press: New York, USA, 1999.

[5] N. Metropolis, A. W. Rosenbluth, M. N. Rosenbluth, A. H. Teller, and E. Teller, "Equation of state calculations by fast computing machines," *The journal of chemical physics*, vol. 21, no. 6, pp. 1087–1092, 1953.

[6] A. J. Archer, "Dynamical density functional theory for molecular and colloidal fluids: A microscopic approach to fluid mechanics," *J. Chem. Phys.*, vol. 130, no. 1, 2009.

[7] U. M. B. Marconi and P. Tarazona, "Dynamic density functional theory of fluids," *J. Chem. Phys.*, vol. 110, no. 16, pp. 8032–8044, 1999.

[8] A. J. Archer and R. Evans, "Dynamical density functional theory and its application to spinodal decomposition," *J. Chem. Phys.*, vol. 121, no. 9, pp. 4246–4254, 2004.

[9] A. J. Archer and M. Rauscher, "Dynamical density functional theory for interacting brownian particles: stochastic or deterministic?," *J. Phys. A: Math. Gen.*, vol. 37, no. 40, pp. 9325–9333, 2004.

[10] A. J. Archer, "Dynamical density functional theory for dense atomic liquids," *J. Phys.: Condens. Matter*, vol. 18, no. 24, p. 5617, 2006.

[11] A. J. Archer, "Dynamical density functional theory for molecular and colloidal fluids: A microscopic approach to fluid mechanics," *J. Chem. Phys.*, vol. 130, no. 1, 2009.

[12] J.-L. Barrat and J.-P. Hansen, *Basic Concepts for Simple and Complex Liquids*. Academic Press, 2003.

[13] J. Rowlinson and B. Widom, *Molecular Theory of Capillarity*. Dover Publications, 2003.

[14] P.-G. De Gennes, F. Brochard-Wyart, and D. Quéré, *Capillarity and wetting phenomena: drops, bubbles, pearls, waves*. Springer Science & Business Media, 2013.

[15] H. Davis, *Statistical Mechanics of Phases, Interfaces and Thin Films*. Wiley-VCH, 1996.

[16] J. T. Simpson, S. R. Hunter, and T. Aytug, "Superhydrophobic materials and coatings: a review," *Reports on Progress in Physics*, vol. 78, no. 8, p. 086501, 2015.

[17] A. Cassie, "Contact angles," *Discussions of the Faraday Society*, vol. 3, pp. 11–16, 1948.

[18] A. E. Reed, L. A. Curtiss, and F. Weinhold, "Intermolecular interactions from a natural bond orbital, donor-acceptor viewpoint," *Chemical Reviews*, vol. 88, no. 6, pp. 899–926, 1988.

[19] M. Doi, *Soft Matter Physics*. Oxford: Oxford Univeristy Press, 2013.

[20] R. Evans, "The nature of the liquid-vapour interface and other topics in the statistical mechanics of non-uniform, classical fluids," *Adv. Phys.*, vol. 28, no. 2, pp. 143–200, 1979.

[21] A. P. Hughes, U. Thiele, and A. J. Archer, "An introduction to inhomogeneous liquids, density functional theory, and the wetting transition," *Am. J. Phys.*, vol. 82, no. 12, pp. 1119–1129, 2014.

[22] J. E. Gubernatis, "Marshall rosenbluth and the metropolis algorithm," *Physics of Plasmas*, vol. 12, no. 5, p. 057303, 2005.

[23] W. K. Hastings, "Monte carlo sampling methods using markov chains and their applications," *Biometrika*, pp. 97–109, 1970.

[24] E. Sanz and D. Marenduzzo, "Dynamic monte carlo versus brownian dynamics: A comparison for self-diffusion and crystallization in colloidal fluids," *The Journal of chemical physics*, vol. 132, no. 19, p. 194102, 2010.

[25] M. L. Crozier, A. Brunton, S. J. Henley, J. D. Shephard, A. Abbas, J. W. Bowers, P. M. Kaminski, and J. M. Walls, "Inkjet and laser hybrid processing for series interconnection of thin film photovoltaics," *Materials Research Innovations*, vol. 18, pp. 509–514, December 2014.

[26] A. Oron, S. H. Davis, and S. G. Bankoff, "Long-scale evolution of thin liquid films," *Rev. Mod. Phys.*, vol. 69, no. 3, p. 931, 1997.

[27] S. Kalliadasis and U. Thiele, *Thin Films of Soft Matter*. Springer, 2007.

[28] U. Thiele, I. Vancea, A. J. Archer, M. J. Robbins, L. Frastia, A. Stannard, E. Pauliac-Vaujour, C. Martin, M. Blunt, and P. Moriarty, "Modelling approaches to the dewetting of evaporating thin films of nanoparticle suspensions," *J. Phys.: Condens. Matter*, vol. 21, no. 26, p. 264016, 2009.

[29] A. Moosavi, M. Rauscher, and S. Dietrich, "Dynamics of nanodroplets on topographically structured substrates," *J. Phys.: Condens. Matter*, vol. 21, no. 46, p. 464120, 2009.

[30] L. Frastia, A. J. Archer, and U. Thiele, "Dynamical model for the formation of patterned deposits at receding contact lines," *Phys. Rev. Lett.*, vol. 106, p. 077801, 2011.

[31] L. Fraštia, A. J. Archer, and U. Thiele, "Modelling the formation of structured deposits at receding contact lines of evaporating solutions and suspensions," *Soft Matter*, vol. 8, no. 44, pp. 11363–11386, 2012.

[32] T. Ingebrigtsen and S. Toxvaerd, "Contact angles of lennard-jones liquids and droplets on planar surfaces," *J. Phys. Chem. C*, vol. 111, no. 24, pp. 8518–8523, 2007.

[33] G. Lu, H. Hu, Y. Duan, and Y. Sun, "Wetting kinetics of water nano-droplet containing non-surfactant nanoparticles: A molecular dynamics study," *App. Phys. Lett.*, vol. 103, no. 25, p. 253104, 2013.

[34] N. Tretyakov, M. Müller, D. Todorova, and U. Thiele, "Parameter passing between molecular dynamics and continuum models for droplets on solid substrates: The static case," *J. Chem. Phys.*, vol. 138, no. 6, p. 064905, 2013.

[35] S. Becker, H. M. Urbassek, M. Horsch, and H. Hasse, "Contact angle of sessile drops in lennard-jones systems," *Langmuir*, vol. 30, no. 45, pp. 13606–13614, 2014.

[36] A. J. Archer, "Dynamical density functional theory for dense atomic liquids," *J. Phys.: Condens. Matter*, vol. 18, no. 24, p. 5617, 2006.

[37] A. Nold, D. N. Sibley, B. D. Goddard, and S. Kalliadasis, "Fluid structure in the immediate vicinity of an equilibrium three-phase contact line and assessment of disjoining pressure models using density functional theory," *Phys. Fluids*, vol. 26, no. 7, p. 072001, 2014.

[38] A. P. Hughes, U. Thiele, and A. J. Archer, "Liquid drops on a surface: Using density functional theory to calculate the binding potential and drop profiles and comparing with results from mesoscopic modelling," *J. Chem. Phys.*, vol. 142, no. 7, p. 074702, 2015.

[39] A. P. Hughes, U. Thiele, and A. J. Archer, "Influence of the fluid structure on the binding potential: comparing liquid drop profiles from density functional theory with results from mesoscopic theory," *J. Chem. Phys.*, vol. 146, p. 064705, 2017.

[40] E. Rabani, D. R. Reichman, P. L. Geissler, and L. E. Brus, "Drying-mediated self-assembly of nanoparticles," *Nature*, vol. 426, no. 6964, pp. 271–274, 2003.

[41] E. Pauliac-Vaujour, A. Stannard, C. Martin, M. O. Blunt, I. Notingher, P. Moriarty, I. Vancea, and U. Thiele, "Fingering instabilities in dewetting nanofluids," *Phys. Rev. Lett.*, vol. 100, no. 17, p. 176102, 2008.

[42] I. Vancea, U. Thiele, E. Pauliac-Vaujour, A. Stannard, C. P. Martin, M. O. Blunt, and P. J. Moriarty, "Front instabilities in evaporatively dewetting nanofluids," *Phys. Rev. E*, vol. 78, p. 041601, 2008.

[43] A. Stannard, "Dewetting-mediated pattern formation in nanoparticle assemblies," *J. Phys.: Condens. Matter*, vol. 23, no. 8, p. 083001, 2011.

[44] C. G. Sztrum, O. Hod, and E. Rabani, "Self-assembly of nanoparticles in three-dimensions: Formation of stalagmites," *J. Phys. Chem. B*, vol. 109, no. 14, pp. 6741–6747, 2005.

[45] H.-S. Kim, S. S. Park, and F. Hagelberg, "Computational approach to drying a nanoparticle-suspended liquid droplet," *J. Nanoparticle Research*, vol. 13, no. 1, pp. 59–68, 2011.

[46] N. Jung, C. S. Yoo, and P. H. Leo, "Instability deposit patterns in an evaporating droplet," *J. Phys. Chem. B*, vol. 118, no. 9, pp. 2535–2543, 2014.

[47] A. Crivoi and F. Duan, "Three-dimensional monte carlo model of the coffee-ring effect in evaporating colloidal droplets," *Scientific reports*, vol. 4, 2014.

[48] W. Tewes, O. Buller, A. Heuer, U. Thiele, and S. V. Gurevich, "Comparing kinetic Monte Carlo and thin-film modeling of transversal instabilities of ridges on patterned substrates," *arXiv:1611.09685*, 2016.

[49] M. J. Robbins, A. J. Archer, and U. Thiele, "Modelling the evaporation of thin films of colloidal suspensions using dynamical density functional theory," *J. Phys.: Condens. Matter*, vol. 23, no. 41, p. 415102, 2011.

[50] A. Kumar, "Isotropic finite-differences," *J. Comp. Phys.*, vol. 201, no. 1, pp. 109 – 118, 2004.

[51] J. D. Weeks, "The roughening transition," in *Ordering in strongly fluctuating condensed matter systems*, pp. 293–317, Springer, 1980.

[52] D. B. Abraham, "Solvable model with a roughening transition for a planar ising ferro-magnet," *Phys. Rev. Lett.*, vol. 44, no. 18, p. 1165, 1980.

[53] D. P. Landau and K. Binder, *A guide to Monte Carlo simulations in statistical physics*. Cambridge university press, 2014.

[54] A. Einstein, "Über die von der molekularkinetischen Theorie der Wärme geforderte Bewegung von in ruhenden Flüssigkeiten suspendierten Teilchen," *Annalen der Physik*, vol. 322, pp. 549–560, 1905.

[55] G. Taubin, "Estimation of planar curves, surfaces, and nonplanar space curves defined by implicit equations with applications to edge and range image segmentation," *IEEE Trans. Pattern Anal. Mach. Intell.*, vol. 13, no. 11, pp. 1115–1138, 1991.

[56] R. N. Wenzel, "Resistance of solid surfaces to wetting by water," *Ind. Eng. Chem.*, vol. 28, no. 8, pp. 988–994, 1936.

[57] A. B. D. Cassie and S. Baxter, "Wettability of porous surfaces," *Trans. Faraday Soc.*, vol. 40, pp. 546–551, 1944.

[58] J. Bico, C. Marzolin, and D. Quéré, "Pearl drops," *EPL (Europhys. Lett.)*, vol. 47, no. 2, p. 220, 1999.

[59] A. P. Hughes, A. J. Archer, and U. Thiele, "An introduction to inhomogeneous liquids, density functional theory, and the wetting transition," *Am. J. Phys.*, vol. 82, no. 12, pp. 1119–1129, 2014.

[60] P. Concus and R. Finn, "On the behavior of a capillary surface in a wedge," *Proc. Natl Acad. Sci. USA*, vol. 63, no. 2, p. 292, 1969.

[61] Y. Pomeau, "Wetting in a corner and related questions," *J. Colloid Int. Sci.*, vol. 113, no. 1, pp. 5–11, 1986.

[62] E. H. Hauge, "Macroscopic theory of wetting in a wedge," *Phys. Rev. A*, vol. 46, no. 8, p. 4994, 1992.

[63] K. Rejmer, S. Dietrich, and M. Napiórkowski, "Filling transition for a wedge," *Phys. Rev. E*, vol. 60, no. 4, p. 4027, 1999.

[64] A. Malijevský and A. O. Parry, "Critical point wedge filling," *Phys. Rev. Lett.*, vol. 110, p. 166101, 2013.

[65] A. Malijevský and A. O. Parry, "Density functional study of complete, first-order and critical wedge filling transitions," *J. Phys.: Condens. Matter*, vol. 25, no. 30, p. 305005, 2013.

[66] M. O. Blunt, A. Stannard, E. Pauliac-Vaujour, C. P. Martin, I. Vancea, M. Suvakov, U. Thiele, B. Tadic, and P. Moriarty, "Patterns and pathways in nanoparticle self-organization," in *Oxford Handbook of Nanoscience and Technology*, 2010.

[67] W. Han and Z. Lin, "Learning from "coffee rings": Ordered structures enabled by controlled evaporative self-assembly," *Angew. Chem. Int. Ed.*, vol. 51, no. 7, pp. 1534–1546, 2012.

[68] A. F. Routh, "Drying of thin colloidal films," *Rep. Prog. Phys.*, vol. 76, no. 4, p. 046603, 2013.

[69] U. Thiele, "Patterned deposition at moving contact lines," *Adv. Col. Int. Sci.*, vol. 206, pp. 399–413, 2014.

[70] R. D. Deegan, O. Bakajin, T. F. Dupont, G. Huber, *et al.*, "Capillary flow as the cause of ring stains from dried liquid drops," *Nature*, vol. 389, no. 6653, p. 827, 1997.

[71] R. G. Larson, "Transport and deposition patterns in drying sessile droplets," *AIChE Journal*, vol. 60, no. 5, pp. 1538–1571, 2014.

[72] P. J. Yunker, T. Still, M. A. Lohr, and A. G. Yodh, "Suppression of the coffee-ring effect by shape-dependent capillary interactions," *Nature*, vol. 476, no. 7360, pp. 308–311, 2011.

[73] D. Bonn, J. Eggers, J. Indekeu, J. Meunier, and E. Rolley, "Wetting and spreading," *Rev. Mod. Phys.*, vol. 81, no. 2, p. 739, 2009.

[74] A. Nold, D. N. Sibley, B. D. Goddard, and S. Kalliadasis, "Nanoscale fluid structure of liquid-solid-vapour contact lines for a wide range of contact angles," *Math. Mod. Nat. Phenom.*, vol. 10, no. 4, pp. 111–125, 2015.

[75] B. D. Goddard, A. Nold, N. Savva, P. Yatsyshin, and S. Kalliadasis, "Unification of dynamic density functional theory for colloidal fluids to include inertia and hydrodynamic interactions: derivation and numerical experiments," *J. Phys.: Condens. Matter*, vol. 25, no. 3, p. 035101, 2012.

[76] I. Vancea, *Pattern formation in nanoparticle suspensions: a Kinetic Monte Carlo approach.* PhD thesis, Loughborough University, 2011.

[77] C. Chalmers, R. Smith, and A. J. Archer, "Modelling the evaporation of nanoparticle suspensions from heterogeneous surfaces," *Journal of Physics: Condensed Matter*, vol. 29, no. 29, p. 295102, 2017.

[78] A. J. Archer, M. J. Robbins, and U. Thiele, "Dynamical density functional theory for the dewetting of evaporating thin films of nanoparticle suspensions exhibiting pattern formation," *Phys. Rev. E*, vol. 81, no. 2, p. 021602, 2010.

[79] M. Rex and H. Löwen, "Dynamical density functional theory for colloidal dispersions including hydrodynamic interactions," *The European Physical Journal E: Soft Matter and Biological Physics*, vol. 28, no. 2, pp. 139–146, 2009.

[80] B. D. Goddard, A. Nold, N. Savva, G. A. Pavliotis, and S. Kalliadasis, "General dynamical density functional theory for classical fluids," *Phys. Rev. Lett.*, vol. 109, no. 12, p. 120603, 2012.

[81] D. Woywod and M. Schoen, "Phase behavior of confined symmetric binary mixtures," *Phys. Rev. E*, vol. 67, p. 026122, Feb 2003.

[82] J. R. Silbermann, D. Woywod, and M. Schoen, "Wetting of a selective solid surface by an asymmetric binary mixture," *Phys. Rev. E*, vol. 69, p. 031606, Mar 2004.

[83] D. Woywod and M. Schoen, "Topography of phase diagrams in binary fluid mixtures: A mean-field lattice density functional study," *Phys. Rev. E*, vol. 73, p. 011201, Jan 2006.

[84] A. Malijevský and A. J. Archer, "Sedimentation of a two-dimensional colloidal mixture exhibiting liquid-liquid and gas-liquid phase separation: A dynamical density functional theory study," *The Journal of Chemical Physics*, vol. 139, no. 14, p. 144901, 2013.

[85] R. Evans and M. C. Stewart, "The local compressibility of liquids near non-adsorbing substrates: a useful measure of solvophobicity and hydrophobicity?," *Journal of Physics: Condensed Matter*, vol. 27, no. 19, p. 194111, 2015.

[86] B. Chacko, R. Evans, and A. J. Archer, "Solvent fluctuations around solvophobic, solvophilic, and patchy nanostructures and the accompanying solvent mediated interactions," *The Journal of Chemical Physics*, vol. 146, no. 12, p. 124703, 2017.

[87] A. Archer, "Dynamical density functional theory: binary phase-separating colloidal fluid in a cavity," *Journal of Physics: Condensed Matter*, vol. 17, pp. 1405 – 1427, 2005.

[88] U. Thiele, D. V. Todorova, and H. Lopez, "Gradient dynamics description for films of mixtures and suspensions: Dewetting triggered by coupled film height and concentration fluctuations," *Phys. Rev. Lett.*, vol. 111, p. 117801, Sep 2013.

[89] K. R. Thomas, N. Clarke, R. Poetes, M. Morariu, and U. Steiner, "Wetting induced instabilities in miscible polymer blends," *Soft Matter*, vol. 6, no. 15, pp. 3517–3523, 2010.

[90] F. A. Bribesh, L. Fraštia, and U. Thiele, "Decomposition driven interface evolution for layers of binary mixtures. iii. two-dimensional steady films with flat and modulated surfaces," *Phys. Fluids*, vol. 24, no. 6, p. 062109, 2012.

[91] R. Yerushalmi-Rozen, T. Kerle, and J. Klein, "Alternative dewetting pathways of thin liquid films," *Science*, vol. 285, no. 5431, pp. 1254–1256, 1999.

[92] U. Thiele and E. Knobloch, "Front and back instability of a liquid film on a slightly inclined plate," *Phys. Fluids*, vol. 15, no. 4, pp. 892–907, 2003.